STRESS AND FAILURE ANALYSIS OF COMPOSITE MATERIALS USING FINITE ELEMENT METHOD

A thesis presented
in partial fulfilment of the requirements
for the degree of
Master of Technology
in Production Technology at
Massey University

Ali Abedian

1992

To my family who gave me great
support and assistant during preparation of this dissertation.

In the Name of Allah (God),
the most Merciful, the most Compassionate

CONTENTS

ACKNOWLEDGEMENTS

I can not find the proper words to appreciate the kind assistance of the following people during the preparation of this dissertation.

1. I would like to thank Dr. E. W. Smith for his excellent and close supervision during the course work and the research.

2. Mr. Harald Hendel, postgraduate student, for his great assistance during the computer work and his encouragement during the writing up stage.

3. Dr. Saied Nahavandi for his great encouragement during the writing up stage.

4. Mr Ian Noell, postgraduate student, for his great assistance in using the computer facilities.

5. Miss Heather North, postgraduate student, for her great assistance during the photography stage.

6. Mr. Len L. Chisholm and Mrs Vicki A. Spagnolo, technicians, for their great assistance during the computer work.

I specially appreciate the Scholarship Dept. of M.C.H.E. of the Islamic Republic of Iran and the Ministry of Jehad-e-Sazandegi for their award of a full fee scholarship and for their excellent assistance.

SUMMARY

STRESS AND FAILURE ANALYSIS OF GLASS/POLYESTER WOVEN ROVINGS COMPOSITE MATERIALS

A micro-mechanistic approach was performed with three-dimensional finite element analysis of stress and failure of glass/polyester woven roving mat composites. In this study the pre- and post-processor software MYSTRO and the finite element analysis software LUSAS were utilised.

The effects of a crimp (curvature), weft fibre, and the matrix volume fraction on the stress distribution and failure of a single short fibre, with 10 μm diameter and 50 mm length, subject to a tensile load, were studied. With the assumption of a perfect fibre-matrix interface the following were concluded:

A) Any curvature along the length of the fibre causes a big internal stress concentration which depends on the radius of the curvature.

B) With an increase of the matrix volume fraction, the stress concentration factor (S.C.F.) decreases.

C) Any direct contact between the interlaced fibres in the cross cover region can cause the fibre failure mode to occur before the other failure modes.

D) The composite failure initiates at the crimped area and propagates along the length of the fibre as a debonding phenomenon. This is followed by matrix failure mode and finally the composite will collapse by the fibre fracture mode.

CHAPTER 1:

LITERATURE SURVEY

1.1. Introduction

In early history, it was found that combinations of materials would produce properties in those materials that were superior to those of the separate components themselves. For instance, Damascus gun barrels combined layers of iron and steel and Mongols made bows from cattle tendons, wood, and silk bonded together. Most naturally occurring materials also derive their superb properties from combination of two or more components which can be distinguished readily when examined under optical or electron microscopes, like many tissues in the body, wood , bone, etc.

A more useful definition of a composite would be: The combination of a reinforcement material (such as a particle or fibre) in a matrix or binder material.

The principle materials used for composite matrices are polymers, ceramics, and metals, with polymers being the most common. Reinforcements are plastics, ceramics, or metals. The different kinds of reinforcements and matrices are shown in the following diagram.

The application of composite materials for designing structures has significantly increased in recent years. Due to continuous advances in manufacturing and analytical techniques, more and more composite structures are designed as primary load carrying elements. To design efficient structures the designer must have a good understanding of the behaviour of the materials used. As a consequence, two of the major concerns when designing these structures are their strength and failure behaviour under different kinds of loading. The design of composite structures is often a combination of traditional practices used for metal structures and empirical criteria.

Many researchers have carried out both the experimental and theoretical stress and failure analysis of composite materials. Some of the existing failure criteria are presented in Appendix A. In this investigation it is desired to find the stress and failure behaviour of woven rovings mat composites under the uniaxial tensile loading. The fabric composite's strength and failure behaviour have also been considered by Chou [1], Ishikawa and Chou [2 to 4]. They have suggested three macro-mechanical models for modelling the stiffness and strength properties of fabric composites (see [5]).

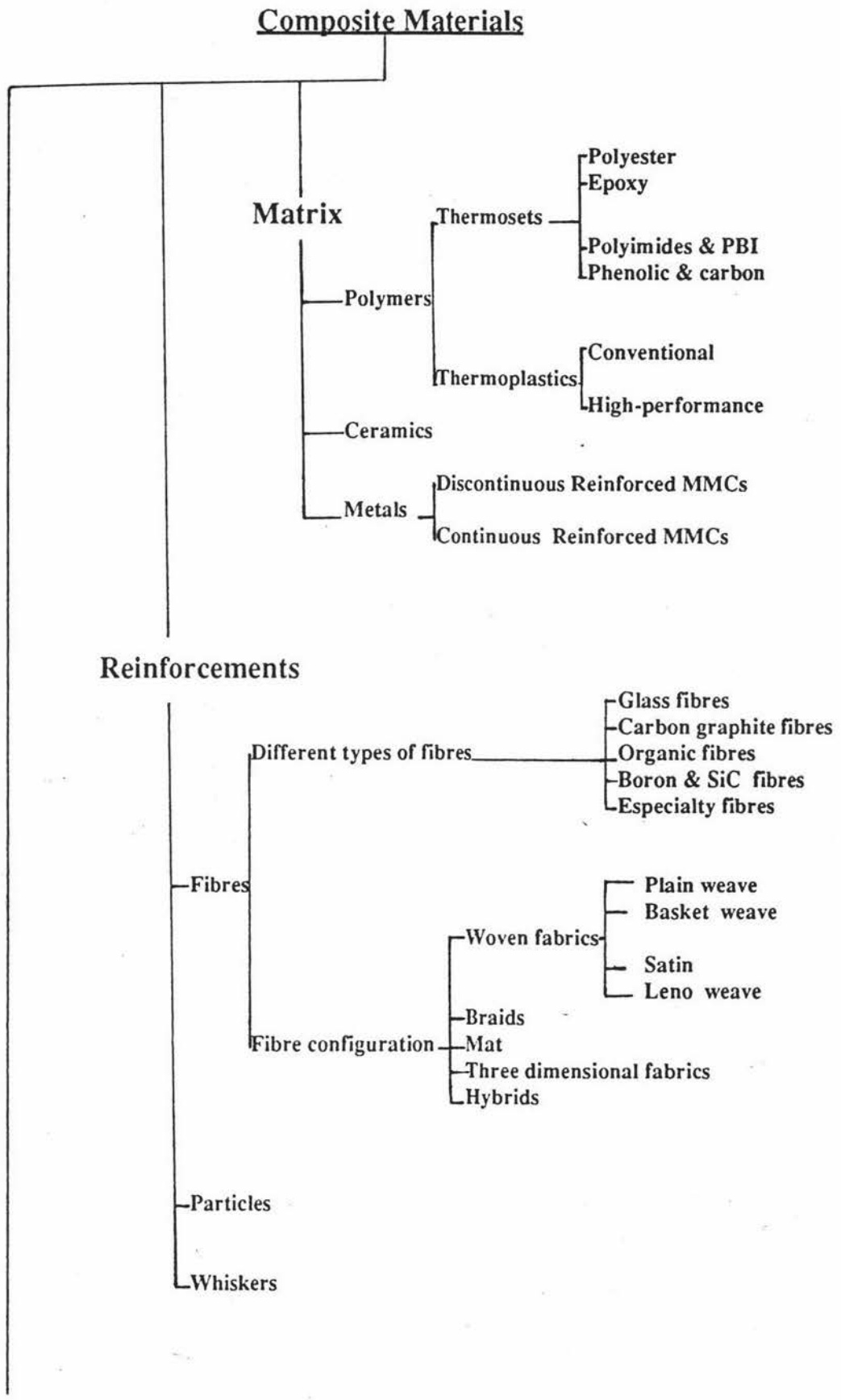

Fibre matrix interface

1.2. An Introduction to Finite Element Method

The finite element method is a numerical procedure for analyzing structures and continua. Usually the problem addressed is too complicated to be solved satisfactorily by classical analytical methods. The finite element method originated as a method of stress analysis. Today it is also used to analyze problems of heat transfer, fluid flow, lubrication, electric and magnetic fields, and many others. In general, this method models a structure as an assemblage of small parts (elements). Each element is of simple geometry and therefore is much easier to analyze than the actual structure. In essence, a complicated solution is approximated by a model that consists of simple solution. Elements are called " finite " to distinguish them from differential elements used in calculus. Each element has nodes (or points) which indicate where elements are connected to one another.

In stress analysis, depending upon the degree of consideration (i.e. 2 or 3 dimensional space) each node has 2 or 3 degrees of freedom (d. o. f.): that is, each node can displace in x and y or in x, y, and z-directions respectively. Thus, if there are n nodes in the structure, there are 2n, or 3n d.o.f. in the model. Algebraic equations that describe the finite element model are solved to determine the d.o.f.. The algebraic equations are generated by appropriate physical quantities which in the stress analysis field could be a chosen displacement function (i.e. ϕ). For a triangular element ϕ could be a polynomial of

$$\phi = a_1 + a_2 x + a_3 y \qquad (1.1(a))$$

Where the a_i are constants. These constants can be expressed in terms of ϕ_1, ϕ_2, and ϕ_3, which are the values of ϕ at the three nodes of the element. For the four-node quadrilateral element, the bilinear function

$$\phi = a_1 + a_2 x + a_3 y + a_4 xy \qquad (1.2(a))$$

is appropriate. Equations1.1(a) and 1.2(a) are interpolations of function ϕ in terms of the position (x, y) within an element [6].

A finite element analysis typically involves the following steps. Steps 1,4, and 5 require decision by the analyst and provide input data for the computer program. Steps 2,3,6, and 7 are carried out automatically by the computer program.

1) Divide the structure or continuum into finite elements.

2) Formulate the properties of each element. In stress analysis, this means determining nodal loads associated with all element deformation states that are allowed.

3) Assemble elements to obtain the finite element model of the structure.

4) Apply the known loads (i.e. nodal forces and/or moments in stress analysis).

5) In stress analysis, specify how the structure is supported. This step involves setting several nodal displacements to known values (which often are zero).

6) Solve simultaneous linear algebraic equations to determine nodal d.o.f. (nodal displacements in stress analysis).

7) In stress analysis, calculate element strains from the nodal d.o.f. and the displacement field interpolation, and finally calculate stresses from strains.

Recently this method is extensively used for stress and failure analysis of composite materials as well. For example Tan [7] has developed a progressive failure model for laminated composites containing openings subjected to in-plane loading using in-plane finite element method. The same study but under compressive loading has been also carried out using 2-D finite element method by Fu-kuo and Lessard [8]. Soutis and Fleck [9] have performed a 2-D finite element study of static compressive failure of carbon/epoxy composite laminates with a single hole. Failure analysis of a laminate due to free edge interlaminar stresses has been investigated by Sun and Chu [10] using 2-D finite element method. A three-dimensional finite element analysis of stresses and strains of thick laminated composites has been performed by Chang and Perez [11]. In all of the mentioned investigations, the FEA results were found in good agreement with the existing experimental data. This method is also used in the present investigation which will be discussed later.

1.3. Mechanics of Composite Mmaterials

1.3.1. Introduction

The strength of fibrous composites is controlled by local inhomogeneties or flaws, since they initiate failure. Flaws may be points of weakness in the fibres themselves or may take the form of unavoidable localized variations in the composite structure such as matrix voids or points of fibre-to-fibre contact. The strength of a composite is controlled by the stress levels at which these flaws propagate. Composite failure may occur as a consequence of fibre failure, matrix failure or failure of the fibre- matrix interface. The form of failure depends upon the relationship between the fibre orientation and the direction of the applied load. Shear forces applied parallel to the direction of the fibre alignment will tend to produce matrix failure or failure of the interface in longitudinal shear. Transverse tensile loads cause failure of the matrix or interface. On the other hand, tensile loads applied parallel to the fibre direction produce failure by fibre fracture. Compression loads, applied in the direction of fibre alignment, can cause failure through localized buckling of the fibres, usually due to inadequate local support by the matrix. Compression loads applied in other directions can cause shear failure of the matrix. Under complex loading conditions one or more failure processes may be occurring simultaneously and these may interact with each other and so modify the stress level at which failure occurs.

Because of the highly anisotropic nature of fibrous composites the stress levels at which the pre-existing flaws propagate within a lamina are dependent on the relative orientation of the fibres to the direction of loading. In the case of multiple laminates, crack extension may take place in plies oriented in particular directions and not in others, so that the laminate may retain a load-bearing capability but have a reduced elastic modulus.

The tensile strength of a lamina measured in the direction of the fibre alignment is much higher than its transverse tensile strength or its in-plane shear strength. Uniaxial compression strength may be higher or lower than the corresponding tensile strengths. When a combination of loads is applied, both the failure stress and the actual mechanism of failure depend upon the loading conditions. Furthermore, failure processes occurring in individual laminae can be inhabited by adjacent laminae when laminae are bonded together to form laminates. This effect depends upon the thicknesses of the laminae [12]. It also depends upon the orientation of the fibres in adjacent laminae.

In this subsection as both axial (tensile and compressive) and transverse strength properties influence design and performance of unidirectional composites, the modes of failure and the factors affecting these strength values will firstly be discussed. The mechanics of fabric reinforcement and especially the influence of crimp on the relative efficiencies of reinforcing fabrics are then reviewed.

1.3.2. Axial Tensile Strength

Axial tensile strength of unidirectional composites is very high, which is one of the major reasons for their high demand. A number of factors control the tensile strength of composites: Fibre modulus and strength properties, matrix mechanical properties including stress-strain behaviour, viscoelastic properties and strength characteristics, and fibre-matrix interfacial strength characteristics.The internal state of stress at the end of a long loaded unidirectional composite specimen is very complex. Although the axial strain in the central portion of the specimen is uniform, the axial stress in the fibres is much greater than that in the matrix because, for most composites, fibre modulus is greater than the matrix modulus (see Figure 1.1).

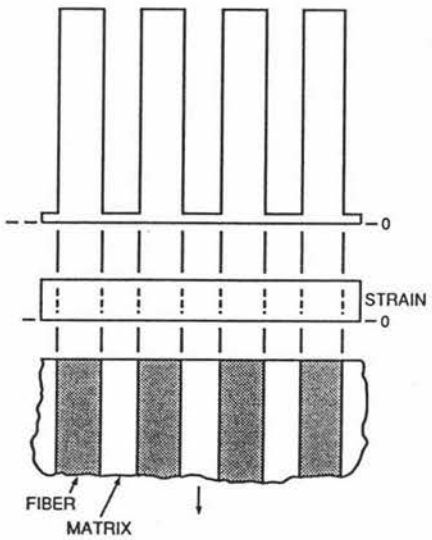

Figure 1.1: Theoretical stress distribution through the fibre and matrix.

One of the reasons for stress complication in composites is related to the different Poisson's ratios of the fibre and matrix. The two materials tend to contract by different amounts laterally to induce a complex transverse stress distribution. For most practical unidirectional composites, the fibre cross section is at least as large as that of the matrix. Therefore, the fibres carry most of the applied load because the total axial loads carried by the fibre and matrix phases are the product of their respective stresses and cross-sectional areas. However, although the direct contribution of the matrix in tensile strength is small, it does have an important indirect influence which is the subject of the next discussion.

The strength of individual fibres varies widely. Hence, one of the fibres in the composite may break down at a very low stress level. The broken fibre will release energy which may cause crack propagation or a stress wave that initiates an immediate and catastrophic mode of failure [13]. The load may be increased if the first fibre breakdown does not result in composite failure. Increasing the load causes additional fibres to break randomly. Figure 1.2 illustrates this process.

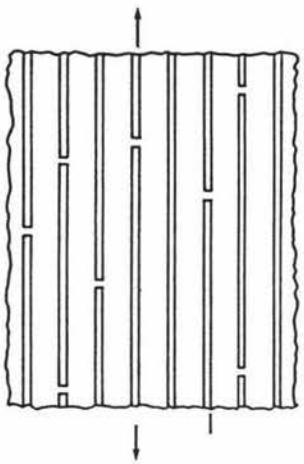

Figure 1.2: Presentation of the randomly broken fibres.

A local perturbation of stress happens in the position of the fibres' break which depends upon fibre modulus, stress-strain properties and strength of the matrix, and the strength of the interfacial bond. The matrix, assuming a perfect bond, resists the displacement of the end of the broken fibre. The resistance appears through shear stress on the lateral surface of the fibre (see Figure 1.3).

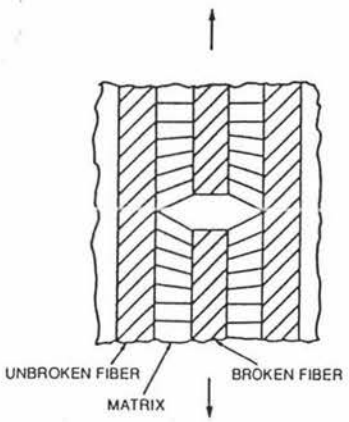

Figure 1.3: Presentation of the broken fibre in the matrix area.

While the tensile load of the fibre at the broken end is zero, the shear stress induces load into the fibre at this point at some distance along its length. Figure 1.4 presents a schematic representation of the interfacial shear stress and fibre tensile stress near a break. This distance, which is required to reload the broken fibre, is frequently referred to as the transfer length l_T. This quantity is referred to as the ineffective length, in the literature. The total distance over which the stress is perturbed is twice this length.

A detailed discussion of the ineffective length is presented in reference [13]. The tensile strength of the composites is not affected by a fibre break. The reason is that the matrix localizes the effect of fibre breaks; thus, ineffective length, rather than overall structure length, becomes the reference dimension for tensile strength. As

Figure 1.4 shows, the shear stress at the point of the break may cause localized failure of the matrix or interfacial bond.

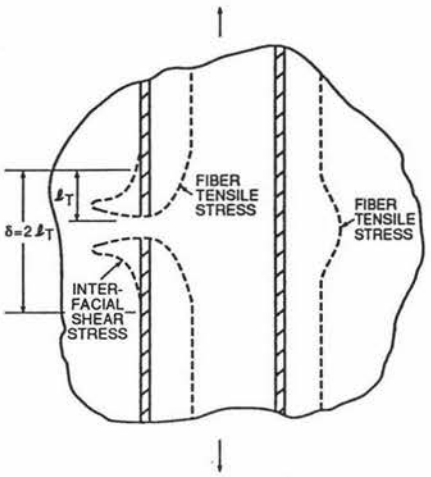

Figure 1.4: Schematic representation of the interfacial shear stress and fibre tensile stress near a break.

The tensile strength of composites is influenced by other aspects of the stress perturbation near the fibre breaks. The broken fibres' load is transferred to the unbroken fibres in the vicinity by the shear stress which causes local stress concentration in the surrounding fibres.The idealized representation of this stress concentration is illustrated in Figure 1.4. The magnitude of the stress concentration depends upon the number of fibres in the vicinity of the break. This value for two intact fibres next to a broken one is 1.33 and for a hexagonal array of the fibres this value is 1.1 for each one of the six fibres surrounding the broken one [13]. The effect of stress concentrations is to increase the failure of the overstressed fibres in the vicinity of the broken fibre. When one of the overstressed fibres breaks the stress concentration value for the unbroken fibres, in a two-dimensional array, is 1.6 compared with 1.33 for one broken fibre [13]. This process can continue, giving rise to a mode of failure associated with propagating fibre breaks.

From the above discussions, it is clear that the internal processes that give rise to tensile failure are complex, and several possible failure modes have been identified. There are more factors which could influence failure. "For example, local matrix or interface failure tends to reduce the intensity of fibre stress concentrations. In addition, when interfacial bond strength is high, fibre fracture can cause penny-shaped cracks in the matrix" [13]. There is one more topic related to composite tensile strength that deserves consideration - size effect. The composite strength decreases with the increasing composite volume. The details of the effect of composite volume and especially fibre length on the tensile strength of composites can be found in references [12] and [13].

1.3.3. Axial Compressive Stress

As in the case of axial tension, most of the applied load is carried by the fibres because of their much greater longitudinal stiffness. Therefore, Figure 1.1 for tensile stress also applies to compressive loading. Under compressive loading the isolated fibres buckle at a very low stress level unless they are extremely short fibres. In spite of the buckling, the compressive strength of the composite is quite high, like graphite/epoxy and boron/epoxy systems. The reason can be explained by the fact that the matrix stabilizes the fibres, preventing them from buckling at low stress levels. It is frequently difficult to determine whether the failure of a composite loaded in axial compressive was initiated by fibre compressive failure or instability. The type of instability referred to here is not overall buckling of the material component or specimen as a structure, rather it is about internal instabilities within the material itself. A number of authors have proposed models for fibre instability like two-dimensional models (shown in Figure 1.5(a)), and a kinking model which is shown schematically in Figure 1.5(b). Fibre instability is sensitive to imperfections such as local curvature and misalignment. When a compressive load is applied to curved fibres, shear stress develops between the fibre and matrix which can result in debonding or matrix cracking, causing overall material failure [13].

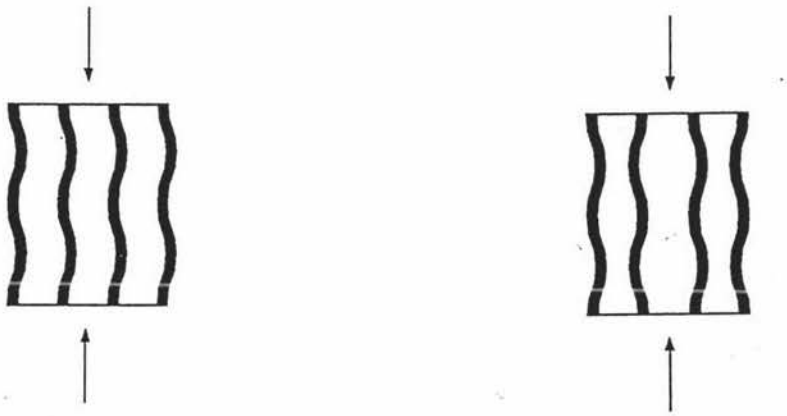

(a) Antisymmetric *(b) Symmetric*

Figure 1.5. Microinstability failure modes

The compressive strength is mostly dependent upon the uniformity of fibre distribution, the presence of matrix voids, the matrix yield strength, the fibre-matrix interface strength, the fibre volume fraction, and the stress level.Typical examples of the experimental relationship between compressive strength and fibre volume fraction are shown in Figure 1.6. "At the relatively low fibre volume fraction of 0.3 the fibre distribution is not particularly uniform and the composite compressive strengths are relatively low and are not sensitive to fibre straightness and fibre misalignment. Indeed, there is some evidence that for composites of this type the compressive strengths are improved as the fibre misalignment is increased up to about 10°" [12]. Composite longitudinal strengths also fall with increasing matrix yield strength values and temperature.

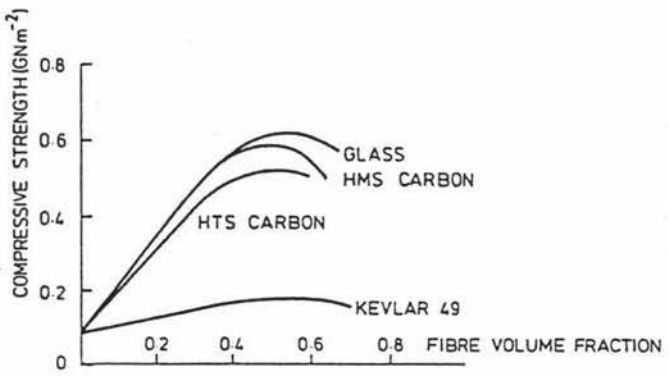

Figure 1.6. Uniaxial compressive strength for a polyester resin reinforced with various fibres. (Redrawn from [12])

1.3.4. Transverse Strength Properties

Transverse strength properties include transverse tensile and compressive strengths and axial interlaminar shear strengths. The major factors that affect these quantities are: matrix strength properties, interfacial properties, and imperfections such as voids and microcracks. In general, when these factors affect one of the transverse properties they affect them all, with the possible exception of transverse compressive strength which is less sensitive to imperfections.

Three modes of failure are recognized in conjunction with transverse strength properties which are shown in Figure 1.7. When the fibre and matrix bond is not high enough relative to the fibre and matrix transverse strengths, the debonding failure mode occurs (Fig. 1.7(a)). In the case of low matrix strength, high bond strength and fibre transverse strength, composite failure happens through the matrix (see Fig. 1.7(b)). The fibre failure mode takes place when the fibre transverse strength is low but matrix and bond strengths are high (Fig. 1.7(c)).

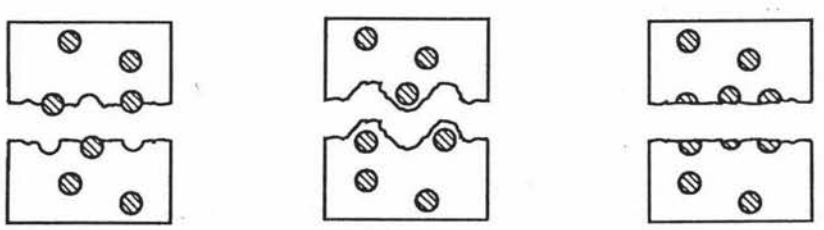

(a) Bond failure *(b): Matrix failure* *(c): Fibre failure*

Figure 1.7:

The effect of matrix strength on transverse strength properties is shown in Figure 1.8 which is the result of work which has been carried out on the glass fibre-epoxy composite. It is clear that the interlaminar shear strength increases as the resin tensile strength increases up to 83 MPa (12E3 psi). Above this value no further increase in interlaminar shear strength is observed because the bond strength becomes the factor which controls the interlaminar shear strength. The effect of internal defect factors, voids, on controlling the transverse strength properties is shown in Figure 1.9.

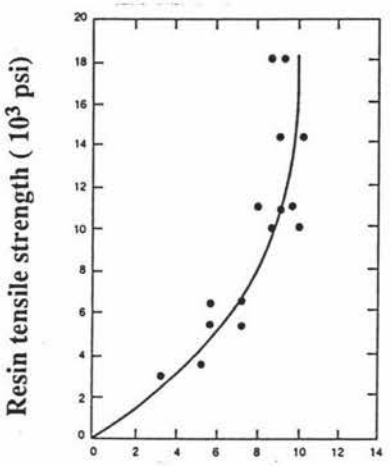

Figure 1.8: (Redrawn from [13])

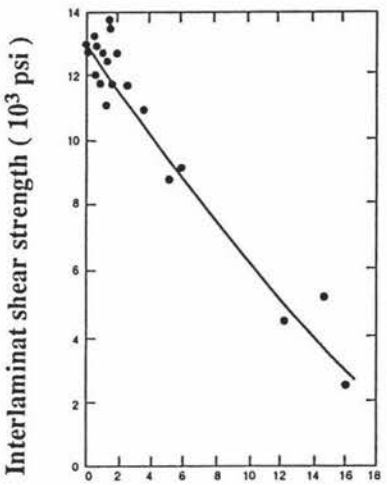

Figure1.9: (Redrawn from [14])

A severe drop in interlaminar shear strength is seen with increasing of the void content. The reason can be explained by the severe internal stress concentrations which voids cause. As discussed earlier, the large difference between the fibre and matrix transverse stiffness properties is the reason for the severe internal stress concentrations in materials with extremely low void contents. The magnitude of the stress concentration factor is dependent upon the volume fraction and also the ratio of axial fibre shear modulus-to-matrix shear modulus. This magnitude increases as each one of the above factors increases (see Figure 1.10).

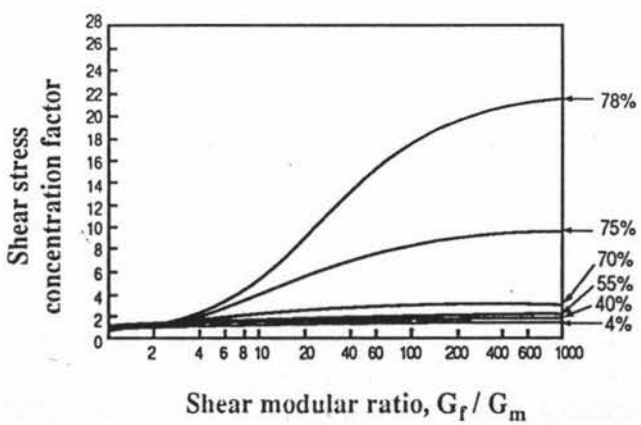

Figure 1.10: (Redrawn from [13]).

1.3.5. Mechanics of Fabric Reinforcement

Fabric composites have mechanical properties similar to those of laminates made from orthogonal unidirectional layers. Woven reinforcing fabrics are made by interlacing individual filaments. There are two main forms of fibre curvature in fabrics: twist and crimp. Twist curvature arises when two yarns twist around each other and crimp is the curvature which arises when fibres pass over and under one another. However, fibre curvature arising from yarn twist and weave crimp makes fabrics significantly less efficient reinforcements than aligned, straight fibres. Fibre crimp causes local stress perturbations which result in lower tensile and compressive strengths. The efficiency of fabric reinforcement depends strongly on the percentage of fibre length that is curved and the severity of the curvature. Figures 1.11(a) and (b) present the influence of fabric construction on flexural modulus and strength respectively. The figures show that both flexural modulus and strength decrease as the fill yarn spacing (picks or fill yarns/cm) increases. Because when the number of fill yarns increase the percentage of curvature on the length of warp yarns increases.

The figures also illustrate the effect of crimp severity at the same fill yarn spacing. As is clear from the graphs, both the flexural modulus and strength are less for crowfoot satins made from 3000 filament yarns than for 1000 filament yarns at the same fill yarn spacing. The graphs of satins with 3000 and 1000 filament yarns are shown

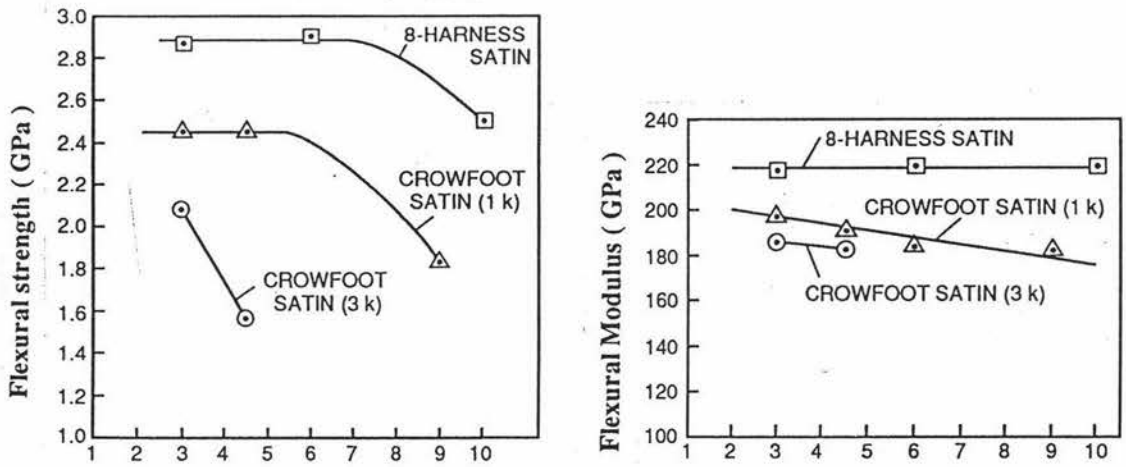

(a) Fill yarn spacing (picks/cm)

(b) Fill yarn spacing (picks/cm)

Figure 1.11: (Redrawn from [13])

with 3k and 1k symbols respectively. Hence, the strength and modulus of fabrics made from heavier yarns for equal fill yarn spacing decrease.

It is also seen that long-shaft satins tend to be relatively efficient because fibres are straight over much of their length. It is noted that flexural strength is much more sensitive to fill spacing than is modulus because material strength characteristics are generally sensitive to local defects whereas moduli are volume average bulk properties.

The properties of fabric composites differ in the warp and fill or weft yarns. Because during weaving tension in warp yarns is generally greater than that in the fill yarns, consequently , the amount of crimp in these yarns differs. There are other sources of warp and fill property differences, such as yarn spacing variability and skewing of yarns, which are not discussed here.

Failure mechanisms in fabric composites have not been studied as extensively as those in unidirectional composites. However, some prominent aspects can be identified. The most important feature is crimp which is reviewed here. Figure 1.12 shows schematically the stress acting on a yarn (warp yarn) subjected to tensile and to compressive axial stresses. The crimped yarn under tensile loading tends to straighten out. This results in compressive stresses on the fibre and in the matrix between the warp yarn and the adjacent fill yarn, which is shown in cross section. The compressive stress in the matrix acts on the fill yarn, tending to displace it laterally. This phenomenon was observed in flexural fatigue tests on woven roving laminates [13]. On the convex part of crimped fibre a tensile stress happens which causes fibre debonding from the matrix in this region. It is noted that the actual stress state in the vicinity of fibre curvature is extremely complex.

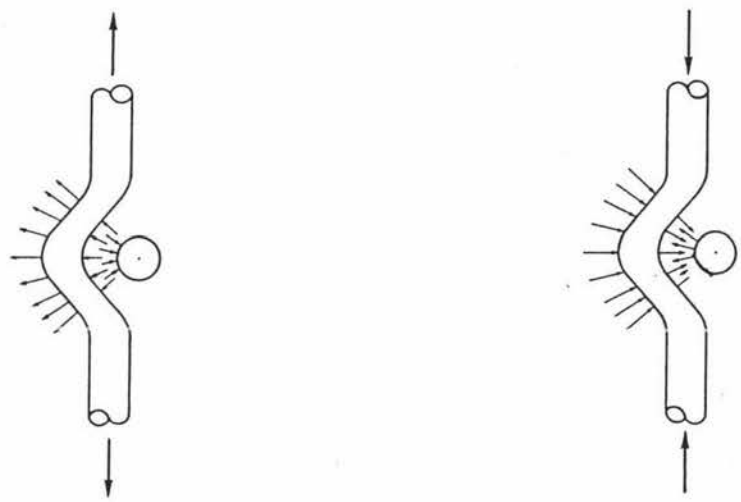

(a): Warp tension *(b): Warp compression*

Figure 1.12:

Under compression loading, because of the curvature, the fibre tends to buckle outward in the cross-over region. Buckling is resisted by compressive matrix stress on the outer, convex surface and tensile stress on the inner, concave surface. In the latter region, fibre debonding is promoted by the interfacial tensile stress. "This, in turn, reduces the lateral constraint on the fibre, intensifying its tendency to buckle" [13]. To summarize, the effect of crimp is to produce local stress perturbations which tend to promote fibre debonding, and other local failure mechanisms. In compression, crimp also promotes local fibre buckling, which results in lower laminate compressive strength compared to [0/90] composites made from unidirectional layers. Further aspects of strength of fabric composites, such as thermal behaviour and three techniques for modelling the stiffness and strength properties, are discussed in reference [13], chapter five.

1.4. Failure Criteria for Composite Materials

1.4.1. Introduction

Strength prediction of any material under combined loading is risky. In the literature as the strength criteria cannot be connected to any governing fundamental principles, they are known as purely empirical in nature. But they are divided into two separate groups which are applicable to homogenous orthotropic materials and laminated material systems [15].

The strength criteria of the orthotropic homogeneous materials are applicable to a wide variety of materials, including composites reinforced with aligned fibres or woven mats, and many discontinuous fibre systems. There are three major criteria in this field: maximum stress, maximum strain, and the quadratic interaction criterion.

In the laminated material systems a procedure for predicting progressive failure of laminates constructed from plies of unidirectional material is discussed. The procedure consists of predicting the first ply failure, followed by assumptions concerning ply unloading that shifts load to the remaining plies. The progressive ply failure procedure is continued until ultimate laminate failure is obtained. The ply failure and unloading procedures used separate fibre failure from matrix failure: therefore, they are most easily applied to unidirectional composites. Residual stresses and strains due to laminate cure are also considered in the strength analysis.

Another group of literature divides the strength prediction of composites into two broad approaches *empirical* and *mechanistic,* Smith and Pascoe [16].The empirical approach attempts to predict the strength at failure from a mathematical model. The basis for the model does not depend upon the constituent make-up of the composite and, indeed, can be the same for macroscopically different materials. This approach takes no account of the modes of failure.

The mechanistic approach attempts to predict strength from the properties and failure characteristics of constituent materials and their interrelationship with each other. This approach requires a careful study of the modes of failure of composites and how the constituent materials contribute to strength.

In this report the former idea is considered. Hence discussion in this section is divided into two major subsections: failure criteria for homogenous orthotropic materials and laminated material systems. Appendix (A) presents a summary of the latest empirical failure criteria.

1.4.2. Strength Criteria for Orthotropic Homogenous Materials

For the propose of strength determination, any composite material that is not in the form of a laminate may be treated as homogenous. The three mentioned strength models are discussed in this subsection. It is noted that the consideration here is

models are discussed in this subsection. It is noted that the consideration here is limited to orthotropic materials with respect to an x_1-x_2 axis system (see Figure 1.13) and is subjected to a state of plane stress.

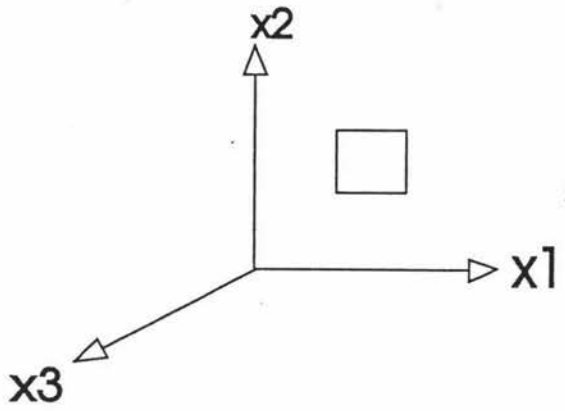

Figure 1.13: The coordinate system of consideration.

1.4.2.1. Maximum Stress Criterion

Failure results when any one of the stress components is equal to its corresponding intrinsic strength property. In mathematical form, the maximum stress criterion is given by

$$\sigma_1 \geq X_1^+,\ \sigma_1 > 0 \quad \text{or} \quad \sigma_1 \leq -X_1^-,\ \sigma_1 < 0 \qquad (1.1)$$

$$\sigma_2 \geq X_2^+,\ \sigma_2 > 0 \quad \text{or} \quad \sigma_2 \leq -X_2^-,\ \sigma_2 < 0 \qquad (1.2)$$

$$\sigma_6 \geq X_6,\ \sigma_6 > 0 \quad \text{or} \quad \sigma_6 \leq -X_6,\ \sigma_6 < 0 \qquad (1.3)$$

Where the intrinsic ultimate strengths are defined as follows:

X_1^+ = Ultimate tensile strength under a uniaxial tensile stress in the x_1 direction.

X_1^-= Ultimate compressive strength under a uniaxial compressive stress in the x_1-direction.

X_2^+ = Ultimate tensile strength under a uniaxial tensile stress in the x_2 direction.

X_2^-= Ultimate compressive strength under a uniaxial compressive stress in the x_2-direction.

X_6 = Ultimate in-plane shear strength under pure shear loading.

For most composite material systems, in-plane shear strengths are equal under positive or negative shear load; $X_6^+ = X_6^-$. This equality is reflected by equation (1.3).

1.4.2.2. Maximum Strain Criterion

The maximum strain criterion is totally analogous to the maximum stress criterion. That is, failure results when any one of the strain components is equal to its corresponding intrinsic ultimate strain. In mathematical form, the maximum strain criterion is given by

$$\varepsilon_1 \geq Y_1^+,\ \varepsilon_1 > 0 \quad \text{or} \quad \varepsilon_1 \leq -Y_1^-,\ \varepsilon_1 < 0 \qquad (1.4)$$

$$\varepsilon_2 \geq Y_2^+,\ \varepsilon_2 > 0 \quad \text{or} \quad \varepsilon_2 \leq -Y_2^-,\ \varepsilon_2 < 0 \qquad (1.5)$$

$$\varepsilon_6 \geq Y_6^+,\ \varepsilon_6 > 0 \quad \text{or} \quad \varepsilon_6 \leq -Y_6^-,\ \varepsilon_6 < 0 \qquad (1.6)$$

Where the intrinsic ultimate strains are defined as follows:

Y_1^+ = Ultimate tensile strain under a uniaxial tensile stress in the x_1 direction.

Y_1^- = Ultimate compressive strain under a uniaxial compressive stress in the x_1 direction.

Y_2^+ = Ultimate tensile strain under a uniaxial tensile stress in the x_2 direction.

Y_2^-= Ultimate compressive strain under a uniaxial compressive stress in the x_2 direction.

Y_6 = Ultimate in-plane shear strength under pure shear loading (assume $Y_6^+ = Y_6^-$).

1.4.2.3. Quadratic Interaction Criterion

Several forms of the quadratic interaction failure criterion may be found in the literature [17-18]. One of the most consistent of this class of failure models was developed by Tsai and Wu [19] as a modification of a theory proposed by Goldenblat and Kopnov [15]. The quadratic interaction criterion accounts for interaction of stress components in determining strength in a biaxial stress field. When the consideration is limited to orthotropic materials subjected to plane stress, the Tsai-Wu criterion is expressed in the form

$$F_{11}\sigma_1^2 + 2F_{12}\sigma_1\sigma_2 + F_{22}\sigma_2^2 + F_{66}\sigma_6^2 + 2F_{16}\sigma_1\sigma_6 + 2F_{26}\sigma_2\sigma_6$$

$$+ F_1\sigma_1 + F_2\sigma_2 + F_6\sigma_6 = 1 \qquad (1.7)$$

F_1, F_2, F_{11}, and F_{22} can be ascertained from measurements of uniaxial strength in the x_1 and x_2 directions and F_6 F_{66} from measurements of positive and negative shear stresses. F_{16} and F_{26} coefficients are both zero. The last two coefficients are ascertained from measurements of combined loading. Like a combination of tensile and shear loading $\frac{\sigma_1}{\sigma_6} = r$ = constant, when $\sigma_2 = 0$ [15]. The only undermined coefficient in Equation (1.7) is the interaction coefficient F_{12}. There are a number of combined stress states which may be used to establish a value of F_{12}. While failure prediction is very sensitive with F_{12}, a wide variation can result in the determination of F_{12}. Narayanaswami and Adelman [20] were able to correlate Equation (1.7) with experimental data by choosing $F_{12} = 0$. It is now necessary to examine three different methods of evaluating F_{12} : the Tsai-Hill, Hoffman, and von Mises plane strain analogy methods. See Smith-Pascoe [16] and Evans-Zhang [21] for further discussion on the determination of F_{12}.

1.4.2.3.1. Tsai-Hill Criterion

The orthotropic yield criterion which was proposed by Hill [15], for a three dimensional state of stress, takes the form

$$(G+H)\sigma_1^2 + (F+H)\sigma_2^2 + (F+G)\sigma_3^2 + 2H\sigma_1\sigma_2 + 2G\sigma_1\sigma_3 +$$

$$2\sigma_2\sigma_3 + 2L\sigma_4^2 + 2M\sigma_5^2 + 2N\sigma_6^2 = 1 \qquad (1.8)$$

This yield criterion was later used as a strength criterion by Tsai. The coefficients of the criterion was ascertained by applying different load conditions.

In summary, the Tsai-Hill criterion, for plane stress ($\sigma_3 = \sigma_4 = \sigma_5 = 0$) becomes

$$\left(\frac{\sigma_1}{X_1^+}\right)^2 + \frac{\sigma_1\sigma_2}{(X_1^+)^2} + \left(\frac{\sigma_2}{X_2^+}\right)^2 + \left(\frac{\sigma_6}{X_6}\right)^2 = 1 \qquad (1.9)$$

It is notable that, this equation is valid based on the assumption that the strengths in the x_2 and x_3 directions are equal [15]. For this case, the interaction term F_{12} is given by

$$F_{12} = 1/2(X_1^+)^2 \qquad (1.10)$$

If σ_1 and σ_2 are compressive stresses, then X_1^+ and X_2^+ in Equation (1.9) are replaced by X_1^- and X_2^- respectively.

If σ_1 and σ_2 are compressive stresses, then X_1^+ and X_2^+ in Equation (1.9) are replaced by X_1^- and X_2^- respectively.

1.4.2.3.2. Hoffman Criterion

Hoffman generalized Hill's criterion to allow for unequal tensile and compressive strengths [15]. For a three-dimensional state of stress, this criterion takes the form

$$C_1(\sigma_2 - \sigma_3)^2 + C_2(\sigma_3 - \sigma_1)^2 + C_3(\sigma_1 - \sigma_2)^2 + C_4\sigma_1 +$$

$$C_5\sigma_2 + C_6\sigma_3 + C_7\sigma_4 + C_8\sigma_5 + C_9\sigma_6 = 1 \qquad (1.11)$$

The same as the Tsai-Hill criterion, coefficients of the Equation were ascertained by applying normal tensile and compressive shear stresses in the three different directions and also assuming equal strengths in the x_2 and x_3 directions [15]. In summary, the Hoffman criterion, for a material subjected to a plane stress ($\sigma_3 = \sigma_4 = \sigma_5 = 0$), becomes

$$\frac{\sigma_1^2}{X_1^+X_1^-} - \frac{\sigma_1\sigma_2}{X_1^+X_1^-} + \frac{\sigma_2^2}{X_2^+X_2^-} + \left(\frac{1}{X_1^+} - \frac{1}{X_1^-}\right)\sigma_1 + \left(\frac{1}{X_2^+} - \frac{1}{X_2^-}\right)\sigma_2 + \left(\frac{\sigma_6}{X_6}\right)^2 = 1 \qquad (1.12)$$

This relationship is of the same form as Equation (1.7), with

$$F_{12} = -\frac{1}{2X_1^+X_1^-} \qquad (1.13)$$

For many materials, such as randomly oriented short fibre composites, the strengths in the x_2 and x_3 directions are not equal: therefore, Equation (1.13) is not valid.

1.4.2.3.2. Von Mises Plane Stress Analogy

The von Mises yield criterion for isotropic materials subjected to plane stress is of the form

$$\left(\frac{\sigma_1}{X_y}\right)^2 - \frac{\sigma_1\sigma_2}{X_y^2} + \left(\frac{\sigma_2}{X_y}\right)^2 = 1 \qquad (1.14)$$

where σ_1 and σ_2 are principal stresses and X_y is the yield strength. Making the substitution $x = \frac{\sigma_1}{X_y}$ and $y = \frac{\sigma_1}{X_y}$ Equation (1.14) becomes

$$x^2 - xy + y^2 = 1 \qquad (1.15)$$

which describes an ellipse with origin at $x = y = 0$ and major axis at 45° to the axis.

"If F_{12} is chosen such as the Equation (1.7), it can be put in the form of Equation (1.15), and the quadratic interaction criterion can be considered as an extension of the von Mises criterion for homogenous materials. This extension has been made by Tsai and Hahn [17]. A conic section or quadratic curves can go from an ellipse to parallel lines, and to hyperbola depending on the value of the interaction term. The criterion that dictates which branch of the quadratic curve it belongs to is based on the value of the following discriminate:

$$\text{Discriminate} = F_{11} F_{22} - F_{12}^2 \quad \begin{cases} > 0 \text{ for ellipse} \\ = 0 \text{ for parallel lines} \\ < 0 \text{ for hyperbola} \end{cases}$$

In order to ensure that the failure criterion represents a closed curve, to avoid infinite strength, this discriminate is constrained by the value shown for the ellipse in the equation above i.e.

$$F_{11} F_{22} - F_{12}^2 > 0 \qquad (1.16)$$

or

$$-\sqrt{F_{11} F_{22}} < F_{12} < \sqrt{F_{11} F_{22}} \qquad (1.17)$$

Now consider the interaction term in a normalized form

$$F_{12}^* = \frac{F_{12}}{\sqrt{F_{11} F_{22}}} = F_{12} \sqrt{X_1^+ X_1^- X_2^+ X_2^-} \qquad (1.18)$$

Expressing Equation (1.17) in terms of the normalized interaction coefficient gives the requirement

$$-1 < F_{12}^* < 1 \qquad (1.19)$$

Using a standard x, y, z coordinate system, The following normalized parameters are defined:

$$x = \sqrt{F_{11}}\ \sigma_x \qquad y = \sqrt{F_{22}}\ \sigma_y \qquad z = \sqrt{F_{66}}\ \sigma_z$$

$$F_1^* = \frac{F_1}{\sqrt{F_{11}}} \qquad F_2^* = \frac{F_2}{\sqrt{F_{22}}} \qquad (1.20)$$

and Equation (1.7) becomes

$$x^2 + 2F_{12}^{*}xy + y^2 + z^2 + F_1^{*}x + F_2^{*}y = 1 \qquad (1.21)$$

This equation can be considered as a generalization of the von Mises criterion if

$$F_{12}^{*} = -\frac{1}{2} \qquad (1.22)$$

In particular, for combined σ_x and σ_y loading (τ_{xy} = 0) with equal tensile and compressive strengths, Equation (1.21) reduces to Equation (1.15).

Solving Equation (1.22) in conjunction with Equation (1.18) for the interaction term yields

$$F_{12} = \frac{-1}{2\sqrt{X_1^{+}X_1^{-}X_2^{+}X_2^{-}}} \qquad (1.23)$$

and Equation (1.7) takes the form

$$\frac{\sigma_1^2}{X_1^{+}X_1^{-}} - \frac{\sigma_1\sigma_2}{\sqrt{X_1^{+}X_1^{-}X_2^{+}X_2^{-}}} + \frac{\sigma_2^2}{X_2^{+}X_2^{-}} + \left(\frac{1}{X_1^{+}} - \frac{1}{X_1^{-}}\right)\sigma_1 + \left(\frac{1}{X_2^{+}} - \frac{1}{X_2^{-}}\right)\sigma_2 + \left(\frac{\sigma_6}{X_6}\right)^2 = 1 \qquad (1.24)$$

1.4.2.4 Strain Space Expression of Quadratic Interaction Criterion

It is often useful to express the interaction criterion in strain space. This expression can be accomplished by substituting the plane stress constitutive relation

$$\sigma_i = Q_{ij}\,\varepsilon_j \qquad (i=j= 1, 2, \text{and } 6) \qquad (1.25)$$

for the orthotropic case ($Q_{16} = Q_{26} = 0$) into Equation (1.7), with the result

$$G_{11}\varepsilon_1^2 - G_{12}\,\varepsilon_1\varepsilon_2 + G_{22}\varepsilon_2^2 + G_{66}\varepsilon_6^2 + G_1\varepsilon_1 + G_2\varepsilon_2 = 1 \qquad (1.26)$$

where

$$G_{11} = F_{11}Q_{11}^2 + 2F_{12}Q_{11}Q_{12} + F_{22}\,Q_{12}^2$$

$$G_{22} = F_{11}Q_{12}^2 + 2F_{12}Q_{12}Q_{22} + F_{22}\,Q_{22}^2$$

$$G_{12} = F_{11}Q_{11}Q_{12} + F_{12}\,[Q_{11}Q_{22} + Q_{12}^2\,] + F_{22}Q_{12}Q_{22}$$

$$G_{66} = F_{66}\,Q_{66}^2 = [\,Q_{66}/S\,]^2$$

$$G_1 = F_1Q_{11} + F_2\,Q_{12}$$

$$G_2 = F_1Q_{12} + F_2Q_{22}$$

This Equation is already dimensionless. Such representation has many advantages, which include the generality of the equation in all physical dimensions. These material constants have the same values in SI and English units.

1.2.3. Strength Criteria for Laminated Orthotropic Materials

Laminate strength is predicted by determining the stress or strain distribution within each ply of the laminate and then systematically applying a given strength criterion. Since the lamina stress state is a function of the laminate configuration, loading, and ply material properties, the elastic stress distribution can be determined only when all of these factors are known. Further more, any inelastic behaviour of the lamina renders the stress field predicted by the elastic analysis invalid. Therefore, it should not be surprising to find that the maximum strain criterion has received widespread adoption, since the distribution of the strain through the laminate thickness is known when the surface strain components are known, regardless of material nonlinearity. The procedure discussed by Petit and Waddoups [15] is typical of this approach and is important because it provides for further loading beyond first ply failure. Many laminate strength criteria are based on first ply fissure, which appears to provide a conservative estimate of laminate failure. Any laminate failure criterion should also consider residual stresses and strains.

Obviously, any of the failure criteria discussed can be used to predict first ply failure. Prediction of laminate response beyond first ply failure is much more difficult [15]. One approach is simply to assume that the failed ply no longer carries any load and shift the load to the remaining plies.This procedure is continued until all of the plies have failed. However, to assume that a failed ply is damaged such that no load is carried is too conservative.

1.2.3.1. Failure of Laminates

For laminates consisting of only unidirectional plies, either continuous or discontinuous, another approach can be used. Distinct failure modes are predicted by the maximum stress criterion [15]. Analogous modes are predicted by the maximum strain criterion. When a ply fails, load carrying capability is reduced relative to distinct modes associated with the failure, whereas load carrying capability is maintained relative to the remaining modes. Such an approach cannot be used in conjunction with the quadratic interaction criterion, since distinct failure modes are not identified. Hashin and Rotem [22] proposed a strength theory for unidirectional composites that separates matrix dominated failure from fibre dominated failure. In particular, the maximum stress criterion is applied to axial strength (X_1^+, X_1^-), and the following combined stress criterion is applied to the matrix dominated failures:

$$\left(\frac{\sigma_1}{X_2^+}\right)^2 + \left(\frac{\sigma_6}{X_6}\right)^2 = 1 \qquad \text{(tensile loading)}$$

$$\left(\frac{\sigma_1}{X_2^-}\right)^2 + \left(\frac{\sigma_6}{X_6}\right)^2 = 1 \qquad \text{(compressive loading)} \qquad (1.27)$$

where the x_1 direction is parallel to the fibres.The quadratic interaction [Eq. (1.24)] can also be modified to consider interaction only between σ_2 and σ_6 for application to matrix dominated failures, with the result

$$\frac{\sigma_2^2}{X_2^+ X_2^-} + \left(\frac{1}{X_2^+} - \frac{1}{X_2^-}\right)\sigma_2 + \left(\frac{\sigma_6}{X_6}\right)^2 = 1 \qquad (1.28)$$

Further discussion of failure and post-failure theories of fibre composite laminates is found in reference [23].

CHAPTER 2:

Recognized Limitations of MYSTRO and LUSAS Finite Element Computer Softwares

2.1.Introduction

During the investigation some limitations of MYSTRO and LUSAS computer software were found which had major effects on the results. The limitations are divided into two groups. The first group consists of the limitations which did not cause big deviations in the results, the second group unfortunatly caused serious problems for the investigation and in some cases stopped the experiments. In this chapter, first the former and then the latter group will be presented and also the methods of solving the problems will be discussed.

2.2. Limitations

2.2.1. Common Limitations

The most important limitation of the first group is related to the load assignment aspect of MYSTRO. The assigned load on the features (i.e. volumes, surfaces, lines, and points) does not appear on some kinds of elements used for discretisation. For example, in one of the meshed models with a mixture of HX20 and PN15 elements, the assigned face load on the model did not appear on the HX20 elements. Therefore, using a mixture of elements, which was important to get more accurate results from the crimped area of the fibre-matrix model, was not possible. Another problem with the load aspect of MYSTRO is specifically related to the face loading type. Sometimes the assigned face load causes an unknown load to appear in the opposite direction to the face load on some of the element's nodes. In the post-processing stage, which will be discussed in the next chapter, occasionally obtaining data automatically from the output file of LUSAS was not possible. This caused some approximated data to be generated.

There are many more such recognized problems which are not discussed here. For more details refer to the LUSAS and MYSTRO Limitations Guide.

2.2.2. Serious Limitations

In this section two of the very important limitations of MYSTRO which were recognized during the investigation will be discussed. It is notable that the limitations have been confirmed by the producer.

One of the capabilities of MYSTRO is mixing two curves together.This is done by the command of spline line. It was found that the most of the models which consist of spline lines cannot be meshed using either the automatic or regular meshing methods of MYSTRO. One of the reasons might be the discontinuity, which can be caused by the inability of the spline line command to mix the curves.

During the experimental stage it was attempted to mesh many models which were composed of spline lines as well as arcs and straight lines. Many variables like spline lines, arcs, the methods of the model creation (i.e. using transformation mirror, transformation translation and so on) were considered to find the cause of the meshing problem. Each of the variables were tested and no progress was made until the spline lines were changed to arc lines. By omitting the spline lines the mesh problem for all of the existing models was solved. The experiments show that a few models with spline lines can be meshed using both of the existing meshing methods. However, it is not expected that the software will work for the sort of models with spline lines. This problem can be one of the most important limitations of MYSTRO because, without a spline line facility no complicated shapes can be generated. On the other hand the spline line facility can be called the master key of the software to the analysis of complicated models. It must be mentioned that, in some cases it is possible to approximate the complicated shapes to the regular shapes. However the imperfections, which are the result of dividing the spline lines to separate arc lines, cause some deviations in the stress distribution in the model.

The second important limitation from this series is related to the automatic meshing method. This facility has been provided for meshing the irregular shapes, like surfaces, with more than four lines and volumes with more than six sides. This method does not work for most of the irregular shapes which consist of spline lines and arc lines, non-planar surfaces, nor for volumes which consist of non planar surfaces.

For using the automatic meshing method it is necessary to create a background-grid around the model which surrounds it. The problem in this stage was appeared with this particular message "A node has been generated out of the background-grid" while the background-grid was consisted the model completely. For finding the error source(s) many such tests for the spline lines were repeated. It was found that the generation of the unknown point out of the background-grid is also related to the spline line problem which discussed above. Because, by ommiting the spline lines this problem solved too.

Rather than the spline line problem which affects automatic meshing, it was also found that, in some cases the irregular shapes which do not have spline lines cannot be meshed using the automatic meshing method either. One of the reasons was found to be related to the background-grid. In some cases, by changing the order of definition

of the points of the background-grid the problem was solved, but it was not a general solution.

The problem with the non-planar surfaces was also related to the spline lines because in order to mesh a non-planar surface it must be laid on a grid surface which must be created with spline lines.

Keeping these limitations in mind the experiments continued by approximating the models to regular shapes to overcome the mesh problem. In addition instead of using the spline lines, two arcs were used in the crimped area of the fibre model. The shape approximation caused it to have many regular shapes which in turn caused it to have a large number of elements. In processing the meshed models by LUSAS software it was found that the core of LUSAS is very limited as it is unable to process a model with more than three hundred elements. This LUSAS limitation halted the experiments for doing mesh refinement. To overcome this problem the straight parts of the models, which do not play an important role in stress distribution and stress concentration across the models, were meshed with a small number of elements to save the core of system for mesh refinment in the crimped area of the models.

CHAPTER 3:

Materials and Methods

3.1. Introduction

A list of the studied models is presented as follows:

I) Single straight fibre surrounded by a cylinder of matrix.

II) Single crimped fibre model.

III) Single crimped fibre-matrix model.

IV) Two crimped and straight crossed fibres.

V) Two crimped and straight crossed fibres surrounded by the matrix.

For all models a perfect interface was assumed. Modelling a real interface was possible using the "3-Dimensional Elasto-Plastic Interface Model" facility of MYSTRO. There was not any evidence to prove the ability of this facility to model a real interface so that results from the models with a perfect interface were considered firstly.

It is notable that each one of the models was made with an approximation due to the limitations. The results provide only some ideas about the stress distribution across the models and in some cases they are not comparable to the theoretical values.

3.2. Model Configuration

Figures 3.1 to 3.8 show the model configurations which were analyzed. The related dimensions are shown in large details in the figures.

Figure 3.1 shows a straight fibre embedded in a cylindrical matrix. The diameter of the fibre and matrix were considered to be 10 μm and 30 μm respectively with 50 mm length. The model was generated by transformation translation, which is a facility of MYSTRO, of two circles along the Y-direction. In this way the model is composed of 5 volumes.

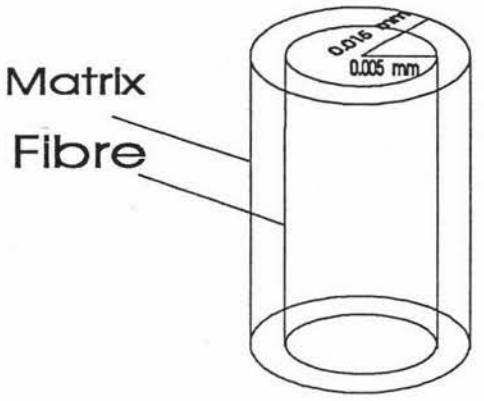

Figure 3.1: Single straight fibre surrounded by a cylindrical matrix.

Figure 3.2(a) shows a single crimped fibre. For this model the same dimensions as in Fig. 3.1 were considered. The detail of the crimped area is shown in Figure 3.2(b). It is notable that the crimped area due to the spline line limitation of MYSTRO was made using two separate arcs. The arcs were considered to have an equal tangent with different signs at their connection point. The model was produced by transforming a circle with three different transformation translations and one transformation mirror. This model consists of six volumes which are shown in Fig. 3.2(a).

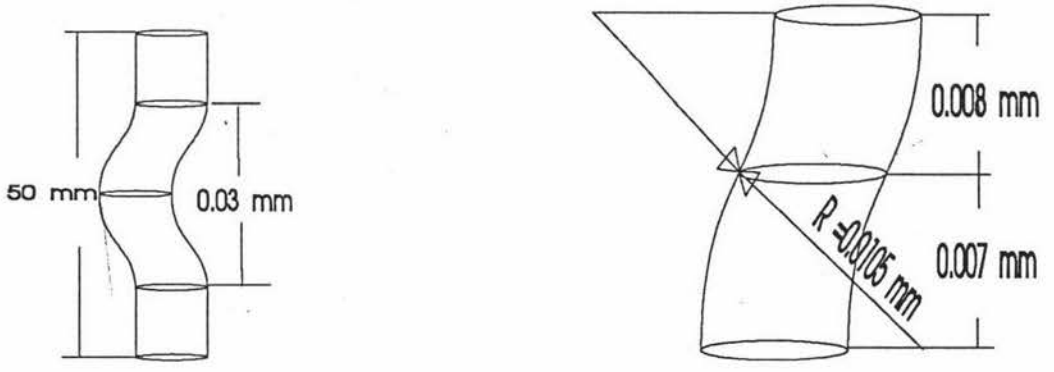

a) Single crimped fibre model. *b) Details of the crimped area.*

Figure 3.2:

Figure 3.3 shows the details of the single crimped fibre-matrix model. The dimensions of the model are the same as Fig. 3.1 and the dimensions of the crimped area are similar to the Fig. 3.2(b). The only difference between Fig. 3.2 and Fig. 3.3 is that in model three, two circles were transformed using similar transformation translations as in Fig. 3.2. The most important problem in this model was related to the number of generated volumes. This model consisted of 30 volumes. This caused it to have many elements so that LUSAS, due to the lack of core, was unable to process. So it was decided to simulate just half of the fibre matrix model. Considering the model symmetry and in order to decrease the number of volumes or number of elements, simulation of a quarter of the fibre and matrix model was attempted. This new model could give the advantage of using the rest of the LUSAS

core in the mesh refining stage. This model simulation was abandoned because of a big difference between its course mesh results and the course mesh results of the last model. In other words the results of the model of Fig. 3.3 was more comparable to the theory than the model of Fig. 3.4. It might be related to the load assignment stage. Therefore the model of Fig. 3.3 was considered for further study with the alteration of decreased number of elements for the straight parts of the model to save the rest of the system core for mesh refinement in the crimped area.

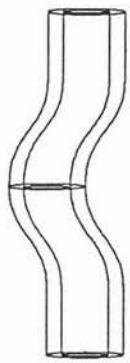

Figure 3.3: Single crimped fibre-matrix model.

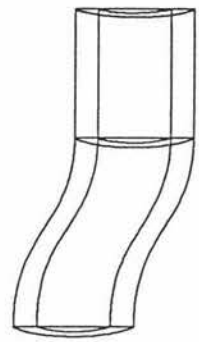

Figure 3.4: A quarter of the model.

Figure 3.5 (overleaf) shows the model which was generated for simulating the stress distribution of two interlaced fibres. In this model one fibre is passed over another. A similar crimped fibre like Figure 3.2(a) and a straight fibre like Figure 3.1 were considered.

In MYSTRO, for transferring a load between two separate features like interlaced fibres there must at least be a line connection between them. The connection between the features can be simulated as a perfect connection (no slipping) or a frictional connection. The properties of the connection can be defined using the "2-D or 3-Dimensional Elasto-Plastic Interface Model" facility of MYSTRO depending on the work space.

As it was discussed in the introduction of this chapter this facility can also be used for defining the properties of the fibre-matrix interface. But in this study a perfect connection (no slipping) between the two fibres was considered.

The only problem in this stage was how to create a line connection between the two fibres with the same dimensions as in Figure 3.2(a). If using the same dimensions as in Figures 3.1 to 3.5 there will be just a point connection between them. Changing the radius of the arcs in the crimped area was not possible because the radius of the arcs had a direct effect on the stress distribution in the crimped area. It was therefore decided to make a small arc right in the centre of the crimped area. The details of the redesigned arc are presented in Figure 3.6 (overleaf).

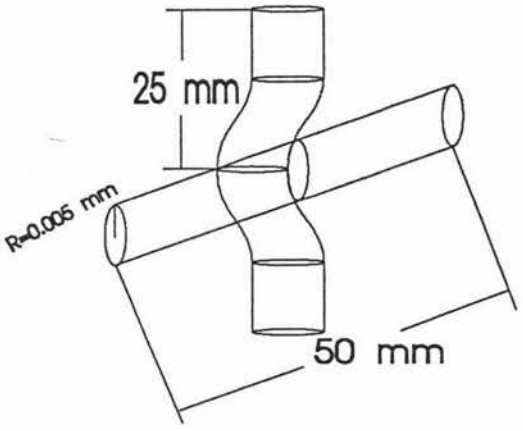

Figure 3.5: Interlaced fibres model.

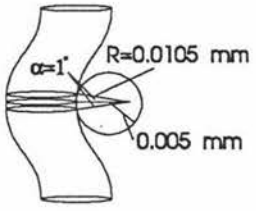

Figure 3.6. Details of the designed arc in the crimped area.

Firstly, with this small arc a line connection between the fibres was made and an ideal connection between them was prepared as well and secondly, the shape of the arcs in the crimped area remained unchanged. The only problem caused by this method was a distortion in the circle of the cross section of the straight fibre. Though it could cause some deviation from the real stress distribution in the straight fibre it would not be as important as changing the radius of the arcs in the crimped area. In the next stage, it was attempted to simulate the same model as in Figure 3.5 plus a matrix between the fibres. Fig. 3.7 shows the interlaced fibres surrounded by the matrix.

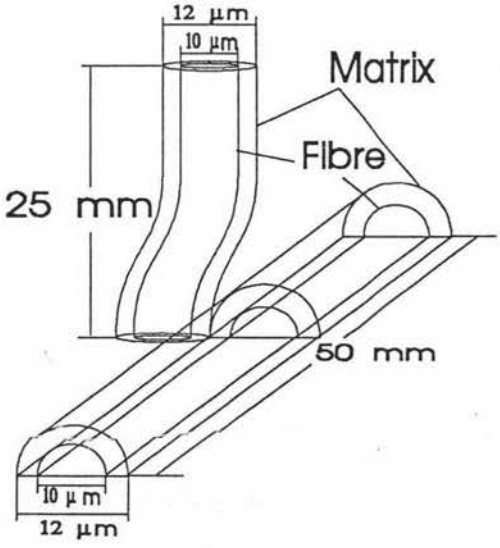

Figure 3.7: Interlaced fibres-matrix model.

It is notable that in this model the diameter of the cylinder of the matrix was changed to 12 μm. Hence the 2 micron gap between the fibres was filled with the matrix. Again a small arc as was designed in the modelling of the two interlaced fibres without a matrix was considered for this model as well. First an arc with the same dimensions was used. But in the discretization stage as the volumes generated by this arc were very small MYSTRO was unable to mesh the volumes. Therefore, it was decided to change the dimensions of the small arc. Finally a five degree arc, which was the smallest arc with which MYSTRO was able to work, was used in this model, see Figure 3.8.

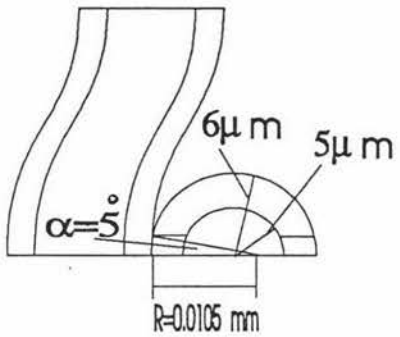

Figure 3.8. Details of the designed arc for the interlaced fibres-matrix model.

3.3. Material Properties

In this study a glass fibre was considered to be surrounded by polyester resin as a matrix. The properties of the fibre and the matrix are presented in Table 3.1 [24].

Table 3.1.

	Modulus of Elasticity (GN/m^2)	Poisson's Ratio	Mass Density (Kg/m^3)	Tensile strength (MN/m^2)
Glass Fibre	76	0.223	2560	3450
Polyester Resin	4	0.38	1400	40 to 90

It is notable that the interface between the fibre and the matrix was considered to be a perfect bond but in a real situation the properties of the interface are less than the fibre and the matrix [25].

3.4. Loading

A 0.01 Newton concentrated tension load was considered to be applied on each of the models. Loading was started with the straight fibre-matrix model. It was applied to the end of the fibre-matrix which consists of five surfaces. Figure 3.9 shows the surfaces which carry the load.

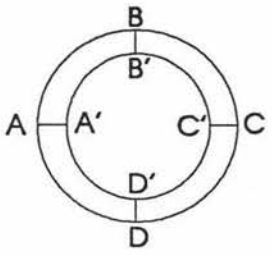

Figure 3.9: Configuration of the surface which the load assigned to.

The inside circle represents the fibre and the rest the matrix area. A problem was recognized at this stage by looking at the generated data file from the model file, it related to the amount of load on the common lines and points of the surfaces of Figure 3.9. As in MYSTRO the concentrated load must be applied to any of the shown surfaces separately, a double load appeared on the common lines (AA', BB', CC', DD') and a triple load on the points A', B', C', and D' which are shown in Figure 3.9. The problem was solved by using the face load facility of MYSTRO. Regarding the 0.01 Newton concentrated load the magnitude of the face load was calculated as follows:

$$F = 0.01 \quad N$$

$$A = A_f + A_m \qquad (3.1)$$

$$w = F / A = 14.1471 \quad MN/m^2 \qquad (3.2)$$

Where A_f and A_m are the fibre and matrix cross section areas respectively and w represents the magnitude of the face load.

A comparison of the results of the fibre-matrix model with those of the single crimped fibre and the interlaced fibres without matrix was desirable. In this case it was necessary to calculate the percentage of the 0.01 N load which was carried by the fibre of the fibre-matrix model. Because of the different moduli of elasticity the fibre and the matrix carry two unequal parts of the concentrated load.

$$F = F_f + F_m \qquad (3.3)$$

Where F_f and F_m are the resultant forces carried by fibre and matrix respectively. For solving the above indeterminate equation it was necessary to derive another equation. So it was assumed that the axial deformations of the two materials (fibre and matrix) were identical.

The deformation due to axial loading is given as $\Delta=FL/AE$ (3.4). Equating axial deformations of the fibre and the matrix give:

$$\frac{F_f L}{A_f E_f} = \frac{F_m L}{A_m E_m}$$

$$F_f = \frac{A_f E_f}{A_m E_m} F_m = \frac{\pi r_f^2 . E_f}{\pi(r_m^2 - r_f^2) . E_m} F_m = 2.375 F_m$$

$$F = F_f + F_m = 1$$

$$F_f = 0.00703703 \quad N$$

Where L is the length of the model and E_f and E_m are the moduli of elasticity of the fibre and the matrix respectively.

Regarding the calculated F_f the magnitude of the face load in the cases of the single crimped fibre and the interlaced fibres is calculated as follows:

$$w = F_f / A_f \quad \text{or} \quad w = 89.595 \quad MN/m^2$$

In the case of the interlaced fibres with the matrix model, as the size of the matrix was changed, to obtain comparable results to the previous models it is necessary to calculate the magnitude of the load which is carried by the matrix with the new size. In the case of the straight fibre matrix model, the contributions of the fibre and the matrix in carrying the 0.01 N concentrated load was calculated as follows:

$$F_f = 0.00703703$$

$$F_m = 0.00296297$$

As the fibre size was not changed the fibre load was considered to remain the same but for the matrix with the new size the load which is named F_m^* was calculated as follows:

$$\frac{F_m}{A_m} = \frac{F_m^*}{A_m^*} \qquad (3.5)$$

$$F_m^* = \frac{A_m^*}{A_m} F_m = \frac{\pi((r_m^*)^2 - r_f^2)}{\pi(r_m^2 - r_f^2)} 0.00296297 = 0.00016296 \quad N$$

Considering the fibre and the new matrix loads the magnitude of the face load was also calculated as follows:

$$F = F_f + F_m^* \qquad (3.6)$$

$$w = F / (A_f + A_m^*)$$

$$w = 63.6619 \quad MN/m^2$$

3.5. Boundary Conditions

The support conditions are one of the most important subjects in a finite element analysis because the supports state the deformation of the model and directly affect the stress distribution in the model. Due to different configurations for each one of the models appropriate support conditions were necessary to define.

Figures 3.10(a) to 3.10(e) (overleaf) show the support conditions of each one of the models.

Figure 3.10(a) represents the straight fibre-matrix model. The applied supports to the ends of the model prevent the movement of the ends in the x and z directions and allow them to move in the load direction y.

Figure 3.10(b) represents the single crimped fibre model. The same supports as Fig. 3.10(a) were used for the ends of this model.

In Figure 3.10(c) which shows the single crimped fibre-matrix model, due to the lack of the core of LUSAS, half of the model is simulated. The same support conditions as Fig. 3.10(a) were considered for the top end section. But at the other end, which is the surface of symmetry of the model, it is sufficient just to simulate the effect of the other half. It was carried out by restraining the movement of the model perpendicular to the cut section. Therefore, this end is free to move in both x and z-directions but it is restrained in the y-direction .

In Figure 3.10(d) the same support conditions as Fig. 3.10(b) were used for the crimped fibre ends. But the ends of the straight fibre of the model were considered to be restrained in all directions (i.e. x, y, and z-directions).

In the last model of the Fig. 3.10(e), again due to the lack of the LUSAS core, half of the model of Fig. 3.10(d) plus the matrix was simulated. The same support conditions as Fig. 3.10(c) were used for the crimped fibre-matrix of the model. However for the straight fibre-matrix in this model the cut section was considered to be restrained in the y-direction and its ends were restrained in all directions, the same as the straight fibre of Fig. 3.10(d).

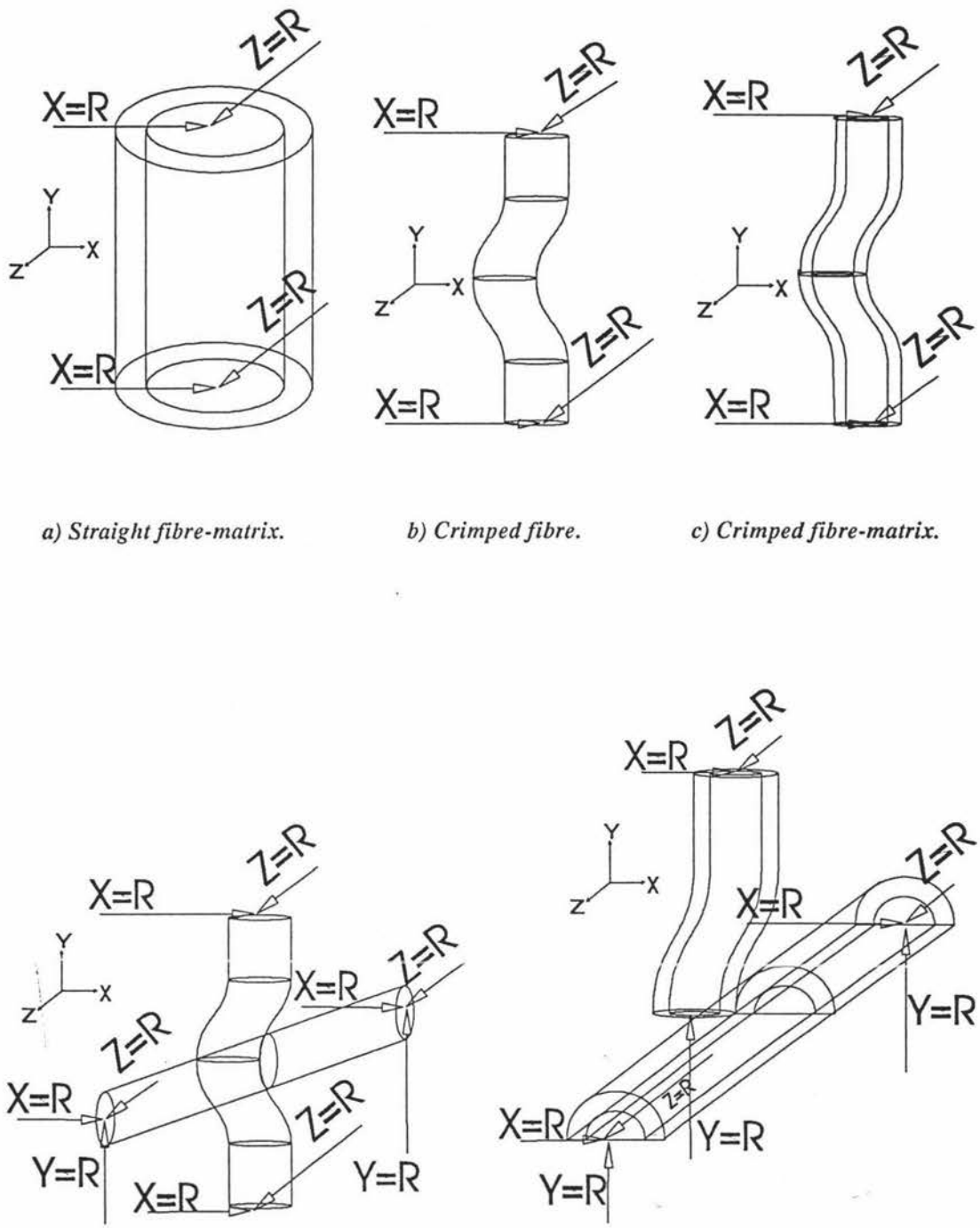

a) Straight fibre-matrix. *b) Crimped fibre.* *c) Crimped fibre-matrix.*

d) Interlaced fibres. *e) Interlaced fibres-matrix.*

Figure 3.10. Apropppriate support conditions for each one of the models.

3.6. Finite Element Modelling

A three dimensional finite element analysis was prepared using MYSTRO and LUSAS Finite element computer softwares . In this subsection, first it is desirable to give a brief explanation about the procedure of the experiments and then the finite element meshing will be discussed in detail.

3.6.1. The Experimental Procedure

The procedure for the experiments is divided into three separate sections.

3.6.1.1. Pre-Processing (by MYSTRO)

In this section the specimen configuration, mesh discretezation, material properties, geometry properties, loads and support conditions are simulated using MYSTRO as a pre-processor. In the end of this section a data file which is readable by LUSAS is created from the generated model file with the TABULATE command facility of MYSTRO.

3.6.1.2. Finite Element Analysis (by LUSAS)

In this stage the generated data file is processed by the LUSAS finite element analysis software. Depending on the degree of the analysis i.e. 2-D or 3-D analysis, different kinds of results have been prepared in LUSAS. In this study a 3-D analysis was carried out using two different solid elements (HX20 and PN15). The available results for the above elements are shown in Table 3.2 [26].

Table 3.2

ELEMENT GROUP		3D - CONTINUUM															
ELEMENT SUBGROUP		SOLID															
ELEMENTS	RESULTS RECORD	COLUMN															
		1	2	3	4	5	6	7	8	9	10	11	12	13	14	15	16
TH10 TH4	DISPLACEMENT	u	v	w	r	v_x	v_y	v_z	a_x	a_y	a_z		C				
PN15 PN6	STRAIN	ε_x	ε_y	ε_z	γ_{xy}	γ_{yz}	γ_{xz}	ε_1	ε_2	ε_3	β	ε_v	C				
PN12	STRAIN "label"																
HX20 HX8	STRESS	σ_x	σ_y	σ_z	σ_{xy}	σ_{yz}	σ_{xz}	σ_1	σ_2	σ_3	σ_s	σ_v	C				
HX16	STRESS "label"																

Where σ_x, σ_y, and σ_z are normal stress components in the x, y, and z directions and σ_{xy}, σ_{yz}, and σ_{xz} are shear stresses on the xy, yz, and xz planes respectively. Also σ_1, σ_2, and σ_3 are major, intermediate, and minor principal stresses and σ_s and σ_v are maximum shear stress and equivalent stress (von-Mises) respectively. Where σ_v in 3-D is as follows:

$$\sigma_v = (\sigma_x^2 + \sigma_y^2 + \sigma_z^2 - \sigma_x\sigma_y - \sigma_y\sigma_z - \sigma_x\sigma_z + 3\sigma_{xy}^2 + 3\sigma_{yz}^2 + 3\sigma_{xz}^2)^{1/2} \qquad (3.7)$$

3.6.1.3. Post-Processing Analysis (by MYSTRO)

The results of the finite element analysis are stored in a file which is readable by MYSTRO. This file consists of the data of Table 3.2 which is processed by MYSTRO to create fill contours of stress and strain, graphs of stress and strain distributions across the specimen, and mesh deformation configurations.

3.6.2. Model Discretization

The mesh configurations of each one of the models are shown in Figures 3.12(a) to 3.12(e).

Two kinds of solid continuum 3-D elements HX20 and PN15 were used for meshing the straight fibre-matrix model. This model was meshed in two ways, first the fibre and the matrix were meshed with HX20 and PN15 respectively. Figure 3.11 shows the configuration of the HX20 and the PN15 elements. However due to the loading problem when using the two kinds of elements, which was discussed in chapter 2, the model was meshed with just the HX20 elements. In this model the length of the fibre was divided into four sections and both the fibre and the matrix circumferences were divided into 16 sections. Therefore, the model consisted of 80 HX20 elements which were dispersed uniformly all over the model. See Figure 3.12(a) overleaf.

In the crimped fibre model more attention was paid to the crimped area of the fibre. The model, apart from the crimped section, consisted of two straight sections. The straight sections were divided into two sections and the length of the crimped area was totally divided into 8 sections. On the other hand, each one of the arcs of the crimped area, which consisted of four arcs, was divided into two sections.

It is notable that the length of the crimped area is 0.03 mm. The circumference of the fibre circle was divided into16 sections, the same as the last model.The result of the meshing was 85 and 125 HX20 elements for the straight parts and the crimped area of the model respectively (see Figure 3.12(b)).

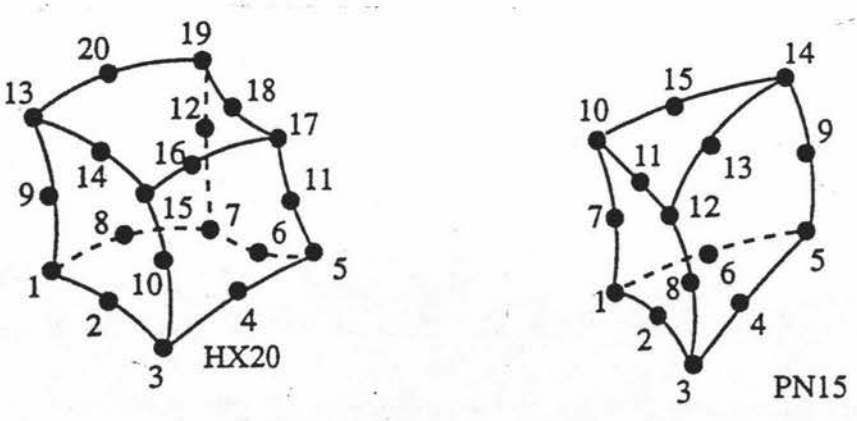

Figure 3.11: Configuration of the HX20 and PN15 elements.

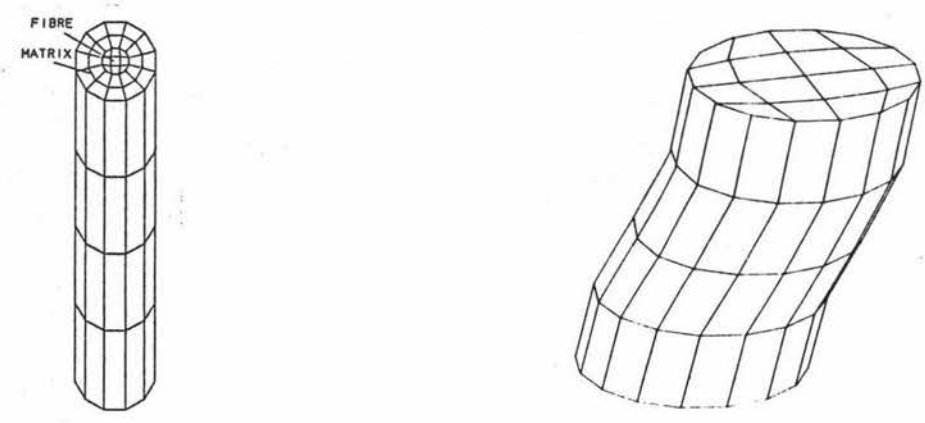

a) Straight fibre-matrix model. *b) Crimped fibre model.*

Figure 3.12: Mesh configuration.

Figure 3.12(c) shows the meshed crimped fibre matrix model with the HX20 elements. The lengths of the straight sections and the crimped area were divided the same as the single crimped fibre model. In this way the model consisted of 150 elements of HX20 of which 120 belonged to the crimped area. The matrix consisted of 100 elements in total.

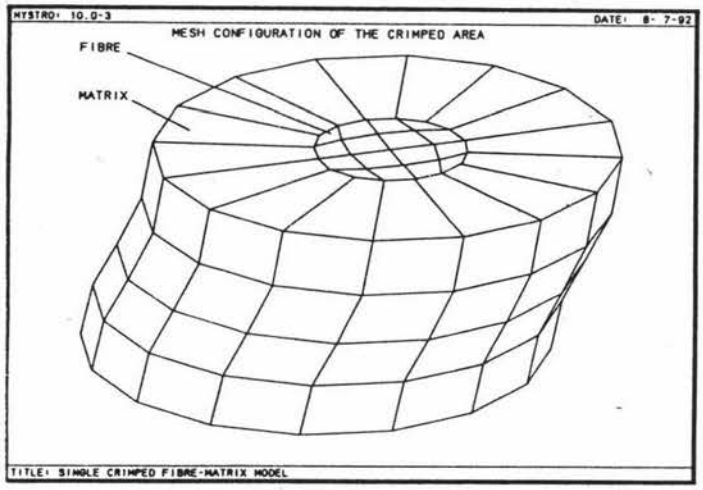

Figure 3.12(c): Mesh configuration of the crimped fibre-matrix model.

The model of the interlaced fibres was meshed with just the HX20 elements. The crimped area in this model, due to the presence of a small arc (2 degree arc) which was discussed in section 3.2, consisted of five volumes. The length of each one of the volumes was divided into two sections as well as the two straight parts of the crimped fibre. The straight fibre in this model was also divided onto two sections in length and its circumference was divided into 16 sections. The model after descretization consisted of 160 elements, 120 and 20 of which belonged to the crimped area and the straight fibre respectively. See Figure 3.12(d) overleaf

Finally, the interlaced fibres plus matrix model consisted of 220 elements. The crimped fibre was divided the same as the last model but the straight fibre of the

model involved some changes. In this model the length of the straight fibre was divided into two sections and the cross section of the fibre shows the number of sections considered for the circumference. See Fig. 3.12(e).

The crimped area and the straight fibre of the model consisted of 160 and 20 elements respectively.

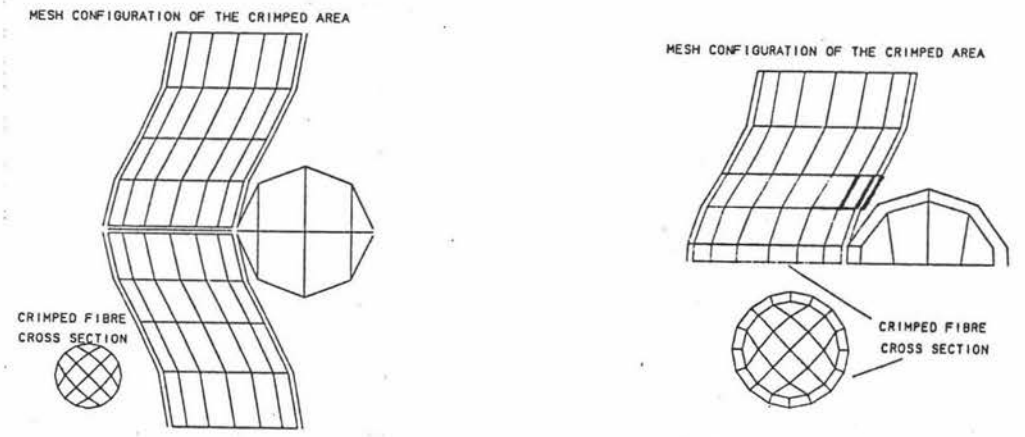

d) Interlaced fibres model. *e) Interlaced fibres-matrix model.*

Figure 3.12: Mesh configuration.

CHAPTER 4 :

Results and Model Discussion

4.1. Introduction

All of the models have been carefully studied from the stress distribution and stress concentration points of view. The provided data includes the normal stress components in 3-D, shear stress on xy, yz, and xz-planes, principal stresses (σ_1, σ_2, σ_3), Maximum shear stress, and von Mises stress for each one of the models.

The above stress components were studied on six cross sections for the straight fibre-matrix model (see Figure 4.1(a)) and for the others on eighteen cross sections, the first eleven of which are located in the crimped area and the rest have been taken from the straight part of the crimped fibre (see Figure 4.1(b)).

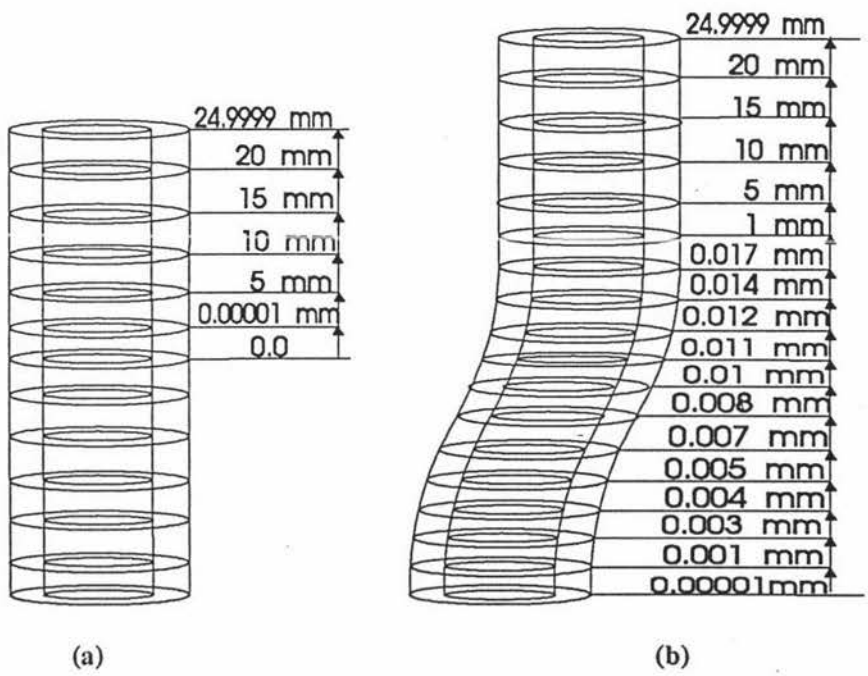

Figure 4.1. Representing the position of the studied cross sections of the models.

It must be noted that the investigation for the interlaced fibres and interlaced fibres plus matrix models has been carried out on the crimped fibre of the models.

The presented data in this study are divided into three different kinds:

A) Colour contours of the normal and shear stress components on the studied cross sections of each one of the models.

B) The positions and the maximum and minimum values of the mentioned stress components on the studied cross sections.

C) Regarding the B section the stress distribution graphs were prepared along the lines where the stress components are maximum.

In this chapter, first the results of the straight fibre-matrix model and then the single crimped fibre model, single crimped fibre-matrix model, interlaced fibres model, and interlaced fibres plus matrix model will be considered respectively.

A brief discussion will be presented on the nature of the stress components and then the results of the models will be compared together. In addition the composites' failure criteria will be examined.

4.2. Straight Fibre-Matrix Model

4.2.1. Stress Analysis

As discussed in chapter one, due to the greater modulus of elasticity most of the applied load ON the model is carried by the fibre and a small amount of it is carried by the matrix. Figure 4.2 (overleaf) shows the normal stress contours in the x, y, and z-directions. The contours of stress in the y-direction show a uniform stress along the length of fibre but a little difference in the values (see Figure 4.3(a)) could be the result of the end effects which deviates the stress values. Theoretically, the maximum stress values of the fibre and matrix in the y-direction, which are calculated in chapter 3, are 89.59 MN/m^2 and 4.71 MN/m^2 respectively.

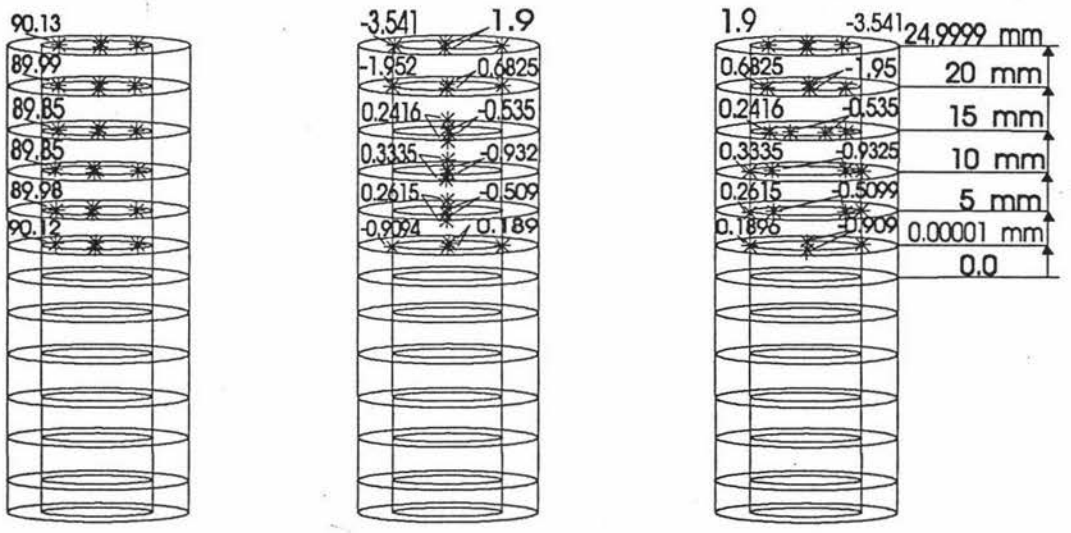

a) y-direction *b) x-direction* *c) z-direction*

Figure 4.3: Maximum values of the normal stress components on the studied sections.

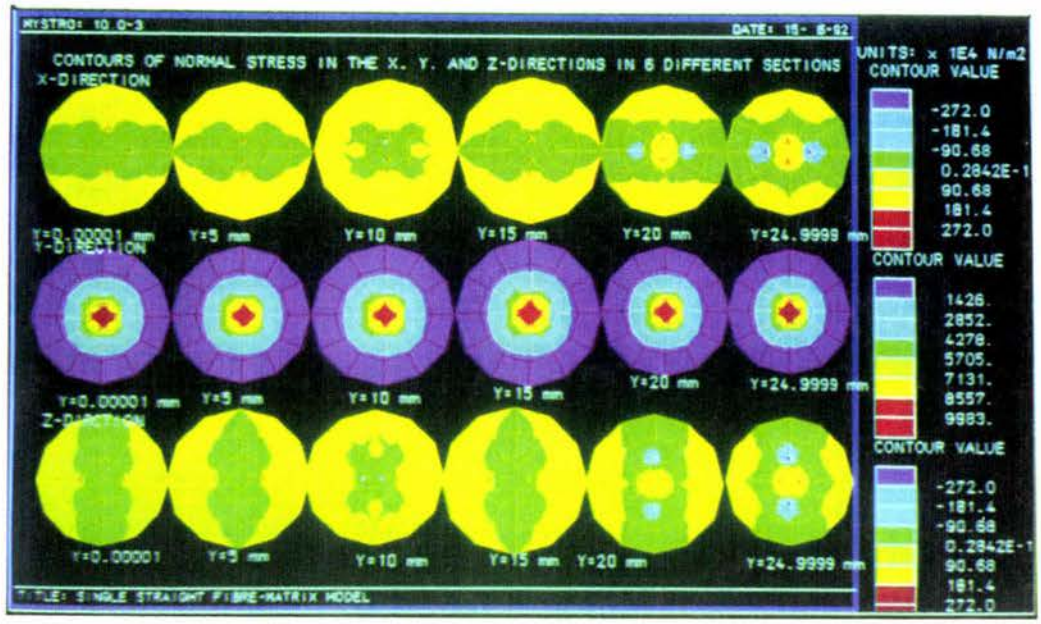

Figure 4.2: Colour contour of the normal stress components on the studied cross section.

The blue regions of the contours of stress in the y-direction show the complexity of the stress around the fibre-matrix interface.

This complex stress area starts almost from the middle of the matrix thickness and contains a small area of the fibre cross section near to the interface which are shown by the green and yellow sections in Figure 4.2. A relatively uniform stress region appears in the centre of the fibre (the red region) which contains most of the fibre cross sectional area. Figure 4.4 (overleaf) shows the stress distribution graphs in the y-direction on the sections y=0.00001, 5, 10, and 24.9999 mm along three different lines. The complexity of the stress at the interface causes the stress curves near the interface to have the form of a cubic spline instead of a step function as in Figure 1.1.

Due to the perfect interface assumption the whole of the structure is going to redistribute the stress. Hence, the structure builds up a complex internal stress which could affect the real stress distribution through the model and especially the stress regions around the interface.

The graphs of Figure 4.4 show that the stress in the y-direction at the interface along the line two is maximum. This phenomenon can be explained by the contours of stress in the x and z-directions (see Figure 4.2). The values of σ_x and σ_z are both compressive along the line two (45° to the horizontal line) near the interface.

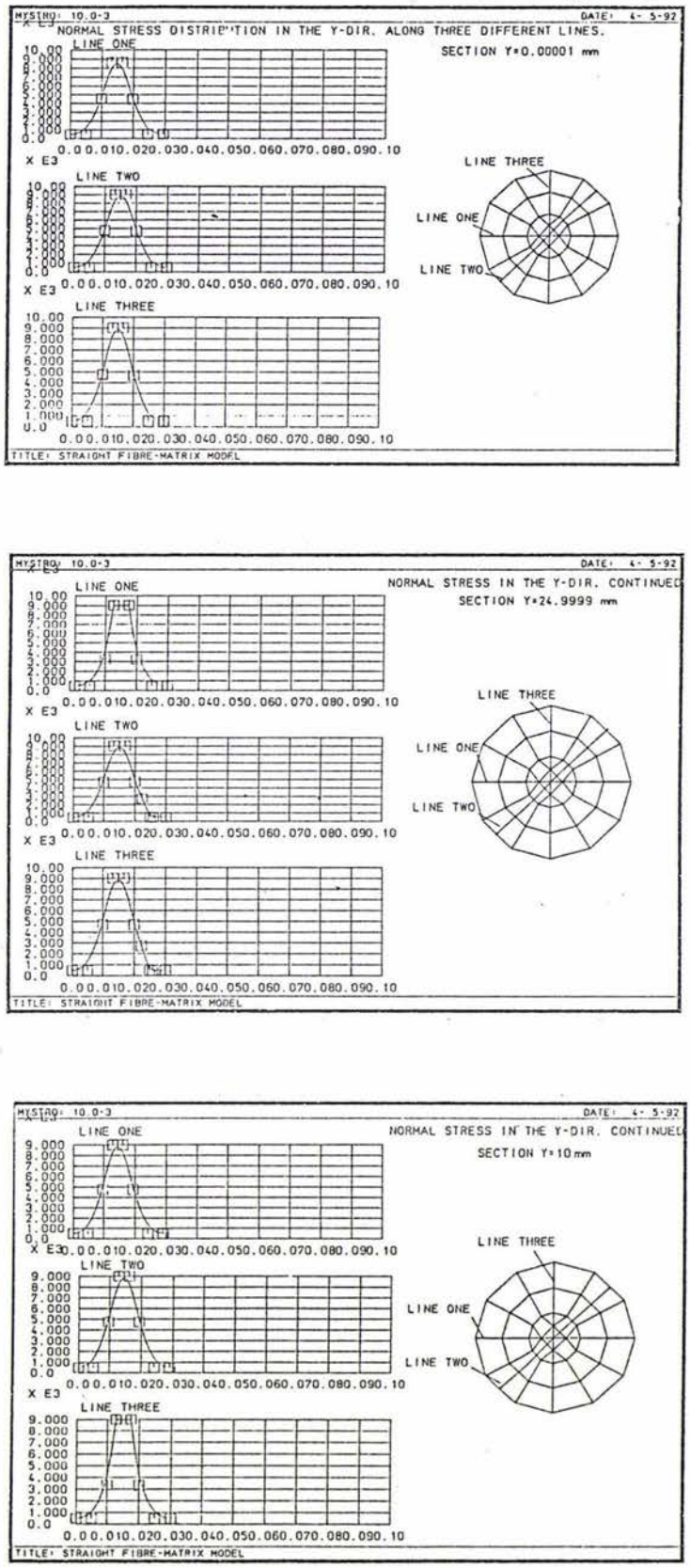

Figure 4.4: Distribution of the normal stress in the y-direction in different sections along the length of the fibre.

The compressive stresses, for any value of the composite's Poisson's ratio, could cause a tensile strain in the y-direction. This is not the case along the lines one and three because at least one of the stress values (σ_x and σ_z) is tensile along these lines which causes a compressive strain in the y-direction. Hence, σ_y is relatively higher at the interface along the line two than the other two lines.

By looking at the contours of stress in the x and z-directions it is clear that the stress situations in both directions are similar (taking into account the 90° rotation) for all of the studied sections. The 90° rotation can be explained by the fact of the different moduli of elasticity of the fibre and matrix. As the fibre's modulus is greater than that of the matrix, it transfers most of the load and creates a relatively high σ_y which in turn causes a high negative stress in both the x an z-directions (Poisson's ratio effect) on the fibre. σ_y is high enough so that the effect of σ_x and σ_z on σ_y and on each other, due to the Poisson's ratio effect, cannot change the sign of the stresses (σ_x and σ_z) on the fibre. Hence the stress in both the x and z-directions on the fibre on each one of the studied sections are compressive (see Figure 4.2). This is not true for the matrix because the low modulus of elasticity of the matrix cannot create a big σ_y on the matrix and as a result big compressive σ_x and σ_z components do not appear on the matrix. Therefore, unlike the fibre the effect of the generated σ_x and σ_z on each other, due to the Poisson's ratio effect, could easily change the sign of the resultant stress. This can be explained with the following mathematical expressions. It can be carried out by ignoring the structure as a composite and assuming the matrix as a homogenous material.

$$\varepsilon_x = \sigma_x - \nu\sigma_y - \nu\sigma_z \qquad (4.1)$$

$$\varepsilon_z = \sigma_z - \nu\sigma_y - \nu\sigma_x \qquad (4.2)$$

In Eq. (4.1) the first and the second terms of the right hand side are negative because, σ_y is tensile and σ_x is the result of the σ_y due to the presence of the Poisson's ratio effect and so will be definitely compressive. Hence if σ_z is tensile the left hand side of Eq. (4.1) will be negative. The same analysis could be considered for Eq. (4.2) which results a negative sign for the left hand side of the equation when the σ_x is tensile. So right on the positions which a compressive σ_x appears a tensile σ_z takes place and vice versa. This is why the 90° rotation is seen on Figure 4.2 at about the centre of the fibre cross section for the σ_x and σ_z.

The values of σ_x, σ_y, and σ_z on Figure 4.3(a), (b) and (c) could be used for calculating the composite's Poisson's ratio. Normally, for homogenous materials in 3-D stress states the following expression

$$(\sigma_x \text{ or } \sigma_z) = \frac{-\nu}{(1+\nu)}\sigma_y \qquad (4.3)$$

is used for calculating the stress values in the x and z directions of a body subjected to σ_y.

Applying the above expression to just the fibre with $\nu = 0.223$ and to the matrix with $\nu = 0.38$ and under the same load as they carry in the composite structure (see section 3.4 for the theoretical values of σ_y for both the fibre and matrix) yields, $\sigma_x = \sigma_z = -16.38$ MN/m^2 and $\sigma_x = \sigma_z = -1.298$ MN/m^2 respectively. But the finite element results (see Figures 4.5(a), (b), and (c)) show that the values of these quantities for the composite are $\sigma_x = \sigma_z = -3.541$ MN/m^2. Regarding the maximum value of σ_y (see Figure 4.3(a)) yields a Poisson's ratio of magnitude $\nu = 0.039$ for the whole of composite. It is notable that this value for a real composite is totally different because of a real interface condition.

Figure 4.5 shows the contours of shear stress on the xy, yz, and xz-planes. The presented cross sections lie on the xz-plane (see Figure 4.1(a)). Since the load in the y-direction is perpendicular to this plane. Hence no shearing stress on both the xy and yz planes appears on the studied cross sections.The small values of the shear stress on the xy and yz planes (see Figures 4.6(a) and (b) (overleaf)) could be the results of the end effects because these values go to zero when the middle of the model is approached.

The resultant stresses i.e. σ_x and σ_z lie on the studied cross section and generate a shear stress on the xz-plane (τ_{xz}). As Figure 4.5 shows the maximum and minimum values of τ_{xz} occur in 30° angle to the x or z axis. This is due to the angle that the result of σ_x and σ_z on each point of the cross section makes with the horizontal or vertical direction.

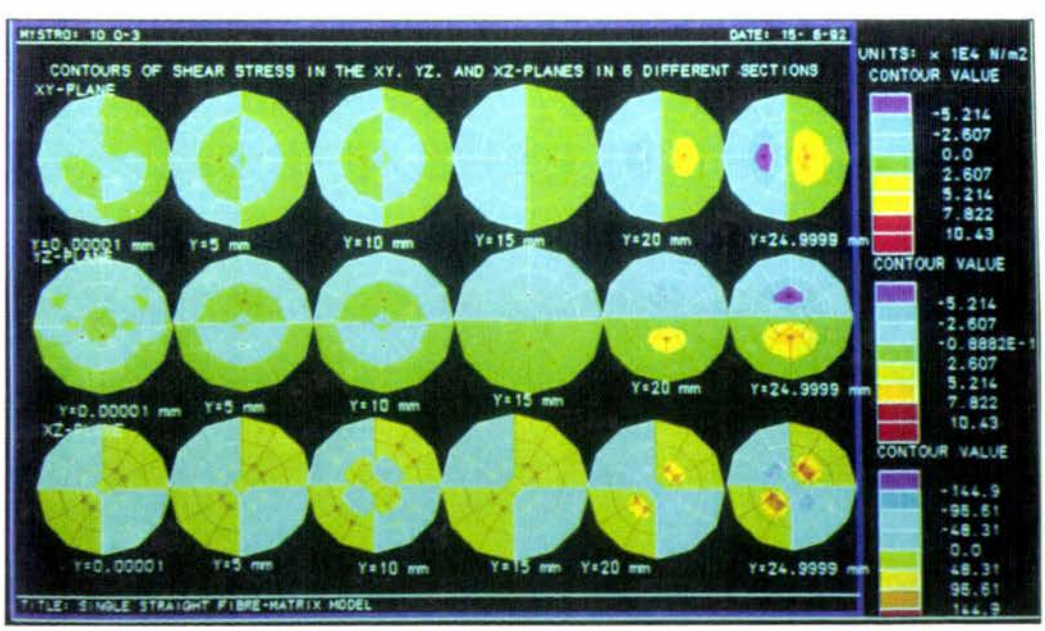

Figure 4.5: Colour contour of the shear stress components on the studied cross section.

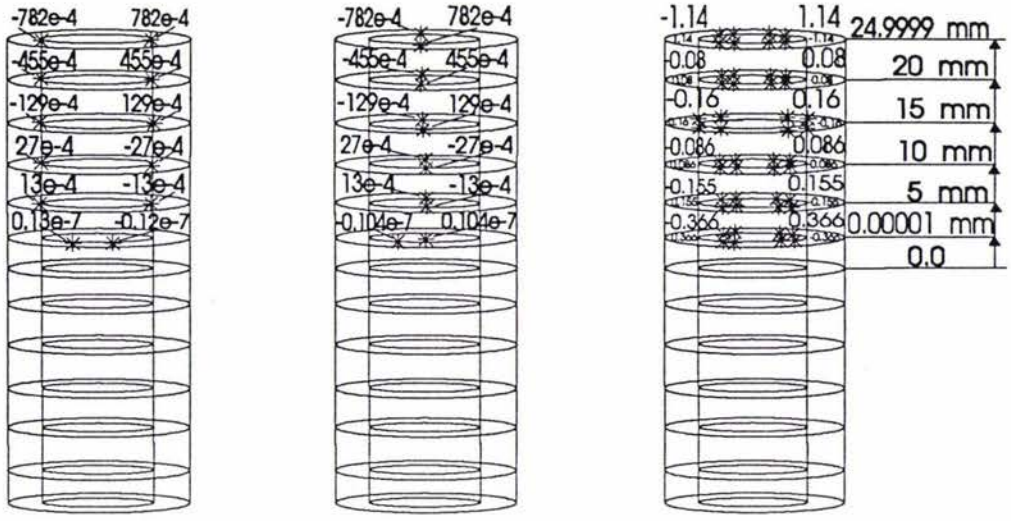

a) on xy-plane *b) on yz-plane* *c) on xz-plane*

Figure 4.7: Maximum values of the shear stress components on the studies sections (unit: MN/m^2)

For example on section y=24.9999 mm the above angle on the position of the maximum σ_x (σ_x = 1.90 MN/m^2) and minimum σ_z (σ_z = -3.541 MN/m^2) is shown in Figure 4.7.

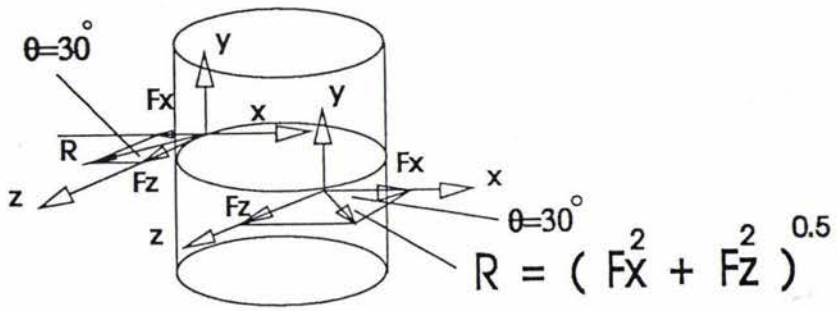

Figure 4.7: Schematic presentation of the reaction load.

4.2.2. Failure Analysis

The existence imprical failure criteria are applicable just to a composite body which consist of laminates. Therefore in this study regarding the micro-mechanistic consideration the existent mechanistic failure criteria are used.

The studied models consist of two different materials and so their behaviour are different in failure. The fibre tends to fail in a brittle manner but the matrix fails like ductile materials. Hence different mechanistic failure criteria are applied to the fibre and matrix. The maximum normal stress and strain failure criteria are considered for the fibre while for the matrix the maximum shear stress and maximum distortional energy (von Mises) criteria are used. It is notable that composite materials unlike metals do not show a plastic deformation before failure. Therefore the yield strength for the mentioned failure criteria is replaced by the ultimate tensile strength of the fibre and matrix.

4.2.2.1. Maximum Normal Stress Criterion

Figure 4.8(a) illustrates stress states associated with safety and with failure for the fibre. The ultimate tensile stress for the E-glass fibre ($\sigma_{uts} = 3450$ MN/m^2), which is presented in Table 3.1, indicates the limitation of the safe region of the criterion.

According to this criterion failure occurs whenever one of the three principal stresses equals the strength. Assuming $\sigma_1 > \sigma_2 > \sigma_3$, Failure occurs if:

$$\sigma_1 = \sigma_{uts} \qquad \text{or} \qquad \sigma_3 = \sigma_{ucs}$$

Here the compressive stresses are not taken into account because no cracks propagate in the compressive regions. In the other word, compressive stresses will no be damaging in terms of failure when considered on their own, but for τ_{max} and von Mises equivalent stress they will have an important contribution.

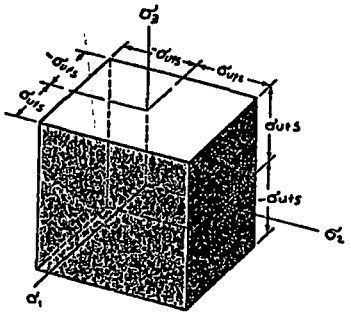

$|\sigma_{uts}| = |\sigma_{ucs}|$

$\sigma_{uts} = 3450$ MN/m^2

a) For the fibre.

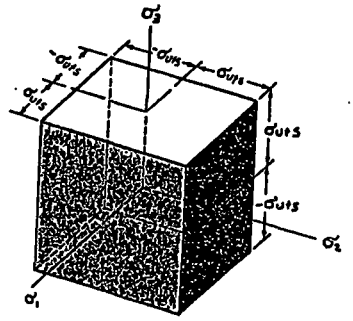

$|\sigma_{uts}| = |\sigma_{ucs}|$

$\sigma_{uts} = 40$ to 90 MN/m^2

b) For the matrix.

Figure 4.8. Schematic representation of the maximum normal stress criterion.

The maximum value of the maximum principal stress of the model happens in the middle and at the end of the model (see Figure 4.9). Except the end values which are not considered here due to the presence of the end effects, the value in the middle section ($\sigma_1 = 90.12$ MN/m^2) is located in the safe region of the criterion (see Figure 4.8(a)).

According to this theory, regardless of the matrix and the interface failure modes increasing the load, a crack will initiate in the fibre region of the cross section and then propagate through the diameter of the fibre. Hence the fibre fracture mode appears before the two modes of failure.

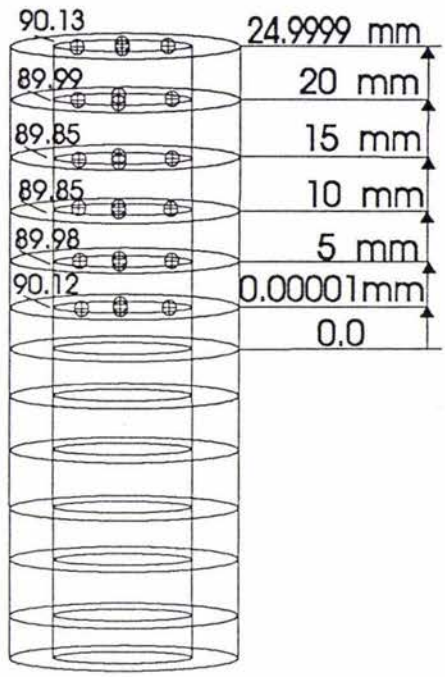

Figure 4.9: Maximum values of σ_1 on the studied cross sections.

According to the literature which was discussed in chapter one, at the broken ends of the fibre a shear stress appears which resists the movement of the fibre (see Figure1.3). This shear stress with increasing the load is predicted to cause the debonding mode of failure which happens because the interface strength in a real situation is less than the matrix [25]. Finally when the fibre fails and also debonding occurs most of the load must be transmitted by the matrix. This in turn causes the matrix failure mode to appear and as a result the composite will collapse.

As discussed above the progressive failure prediction occurs when the maximum principal stress of the matrix remains in the safe region of the criterion based on the σ_{uts} of the matrix (see Figure 4.8(b)).

Figure 4.10(a) shows the distribution of the maximum principal stress on the section y=0.00001 mm, on which the maximum value of σ_1 appears on it. The graphs show that the value of σ_1 along the line two is maximum (σ_1 = 50 MN/m^2) which happens at the interface. This value shows that the matrix under the applied load is in a critical situation because it lies on the boundary of the safe region of the criterion (see Figure 4.8(b)).

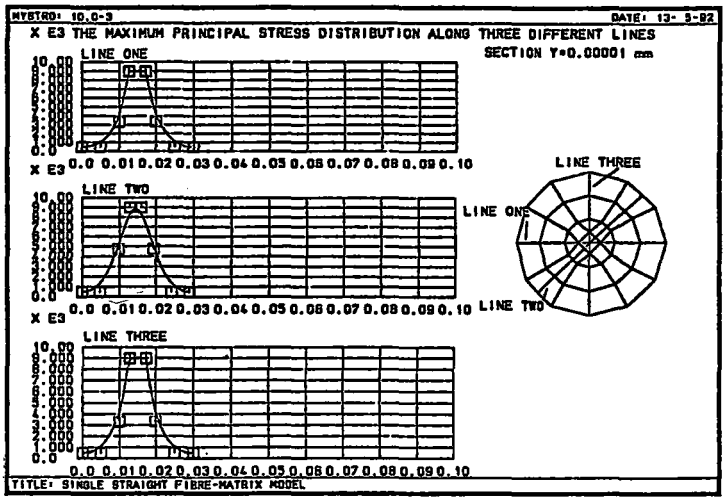

Figure 4.10(a): Distribution of σ_1 on section y=0.00001 mm.

Based on this result, assuming a perfect interface, the fibre-matrix debonding mode of failure may occur before the others because the maximum of σ_1 happens at the interface. The initiated failure will then run through the matrix and with further increasing of the load, fibre fracture will cause the composite collapse.

Assuming a real interface may change the failure phenomenon. The maximum principal stress distribution curve of Figure 4.10(a) may change under a real interface condition as in Figure 4.10(b)

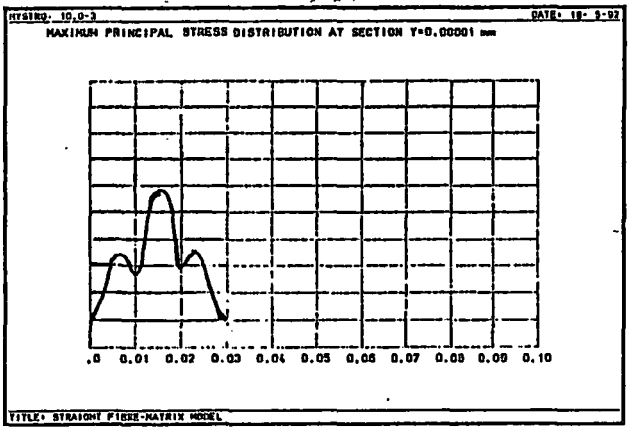

Figure 4.10(b): Prediction of the maximum principal stress distribution on section y=0.00001 under a real interface condition.

Under this possibility of stress distribution the maximum stress may occur in the matrix region. This may initiate a small crack which may propagate through the matrix first and then cause the debonding mode to appear and finally with further increasing of the load the fibre fracture happens.

Another possibility which could be considered here is that the maximum value of σ_1 in all sections happens at the interface. Therefore the initiated local debonding may instead of causing the matrix failure, run along the length of the interface and cause a fibre pull out phenomenon to appear.

All the described possible failure phenomenons may be affected by the fibre strength situation. As discussed in chapter one the stress concentration factor, the fibre contact, the fibre manufacturing methods, and many other factors, which are not taken into account, may affect the fibre's strength. A very weak fibre or the stress concentration on the fibre could cause the fibre fracture mode to appear before the other modes.

4.2.2.2. Maximum Normal Strain Criterion

According to this theory failure occurs when the largest of the three principal strains becomes equal to the strain corresponding to the tensile strength.

$$\sigma_1 - \nu (\sigma_2 - \sigma_3) = \sigma_{uts}$$
$$\sigma_2 - \nu (\sigma_3 - \sigma_1) = \sigma_{uts}$$
$$\sigma_3 - \nu (\sigma_1 - \sigma_2) = \sigma_{uts}$$

Figure 4.11(a) shows the safe and failure regions for the fibre according to the maximum normal strain theory.

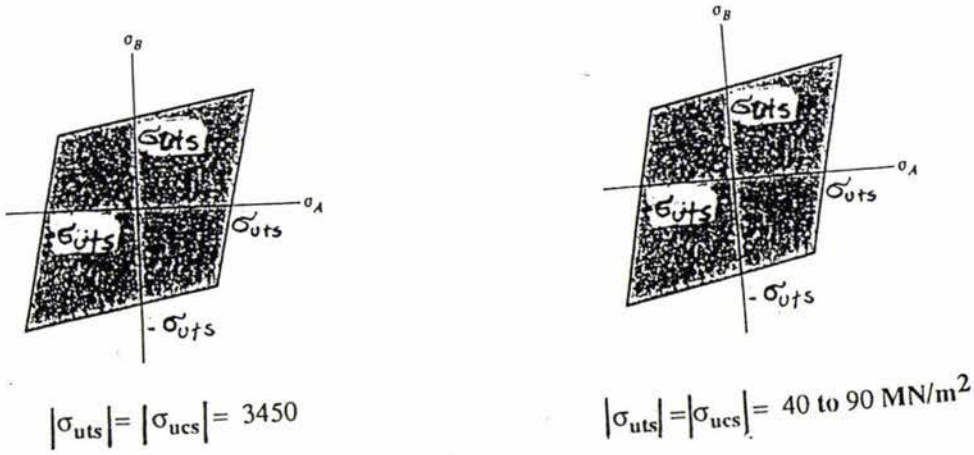

(a) For the fibre. *(b) For the matrix.*

Figure 4.11: Schematic representation of the normal strain criterion.

The maximum strain of the model happens at the section y=0.00001 mm (see Figure 4.12). The strain value in this section neglecting a little deviation is uniform on the whole area of the section. The mentioned deviation of the maximum principal strain is shown in Figure 4.13.

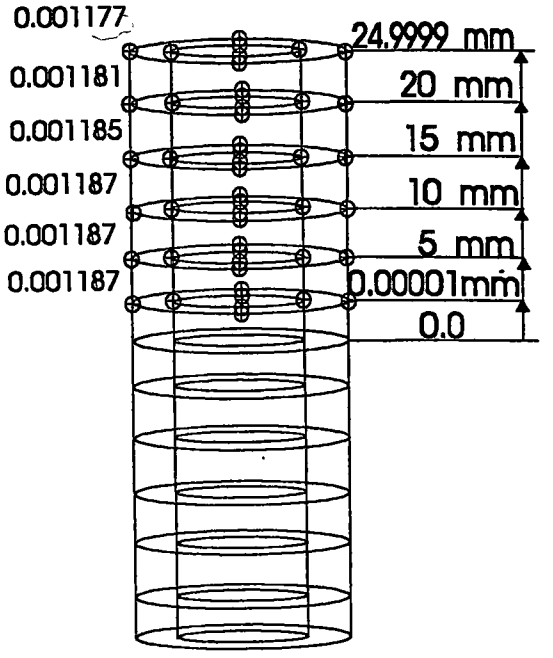

Figure 4.12: Maximum values of ε_1 on the studied cross sections.

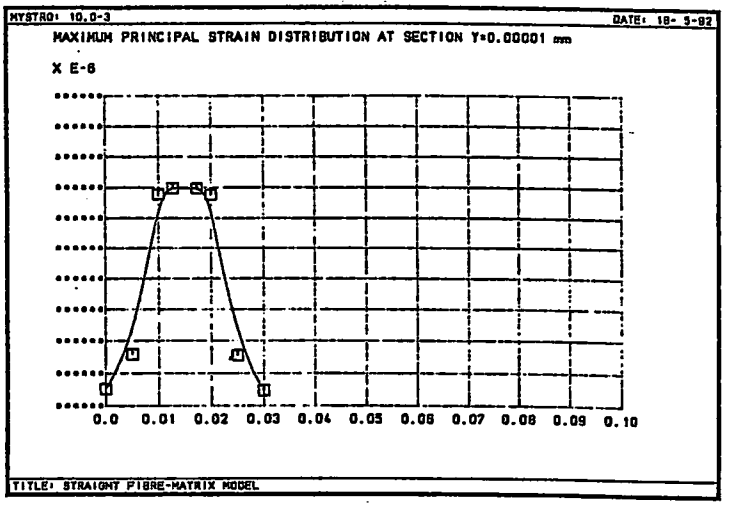

Figure 4.13: Distribution of ε_1 on section y=0.00001 mm.

According to the values of Figure 4.12 the maximum value of ε_1 is less than the normal strain corresponding to the ultimate tensile strength of the fibre.

$$0.001187 < 0.0454$$

It is graphically shown in Figure 4.11(a). Hence, the model regardless of the matrix and interface is safe under the applied load and comparing the values shows that the model will remain safe with further increasing of the load.

Applying the criterion to the matrix yields:

$$0.001187 < 0.01 \text{ to } 0.0225$$

(see Figure 4.11(b)). The above result shows that the matrix is safe under the applied load. Comparing this to the result of the maximum normal stress criterion shows that the latter criterion gives a more inside prediction than the former one.

Failure can be predicted by taking the deviation of the strain into account (see Figure 4.13). As the graph of the strain deviation shows the maximum deviation from the uniform value which happens on the fibre and in the matrix area it appears at the interface. Regarding the uniform value of ε_1 on the cross section and comparing the values of ε_{uts} the fibre and matrix boosts this idea that failure of the composite is governed by the matrix.

As the maximum strain deviation in the matrix area occurs at the interface, with increasing of the load the failure may initiate with debonding. From the ε_{uts} values of the fibre and matrix it can be predicted that the initiated crack will then run to the matrix area and finally the composite will collapse with further increasing of the load by fibre fracture.

4.2.2.3. Maximum Shear Stress Criterion

According to the maximum shear stress theory, the specimen fails whenever the maximum shear stress in any element becomes equal to the maximum shear stress in a tension test. Assuming $\sigma_1 > \sigma_2 > \sigma_3$, then

$$\tau_{max} > 0.5\, \tau_{uts}$$

where τ_{max} could be one of the following expressions

$$\frac{(\sigma_1 - \sigma_2)}{2} \qquad \frac{(\sigma_2 - \sigma_3)}{2} \qquad \frac{(\sigma_1 - \sigma_3)}{2}$$

Figure 4.14 illustrates the safe and failure regions of the criterion based on the σ_{uts} = 40 to 90 MN/m^2 of the matrix.

The Maximum shear stress of the model τ_{max} = 45.4 MN/m^2 lies on the cross section y= 10 mm (see Figure 4.15) and happens on the fibre. Figure 4.16 represents the maximum shear stress distribution through the matrix. The graph of maximum shear stress along the line two gives the value of τ_{max} = 25 MN/m^2 which happens at the interface. This value lies in the safe region of the criterion (see Figure 4.14).

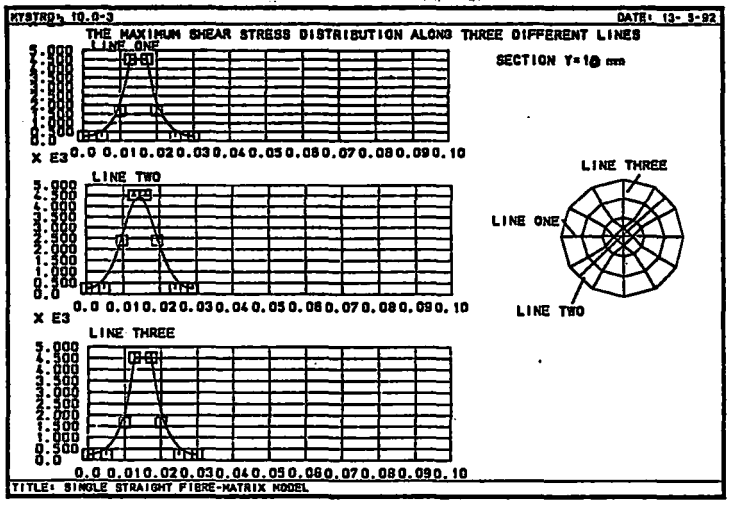

Figure 4.16:

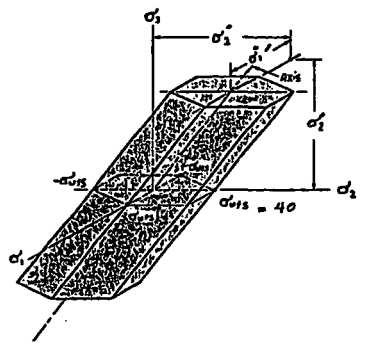

$|\sigma uts| = |\sigma ucs| =$ 40 to 90 MN/m^2

Figure 4.14: Schematic representation of the maximum shear stress criterion.

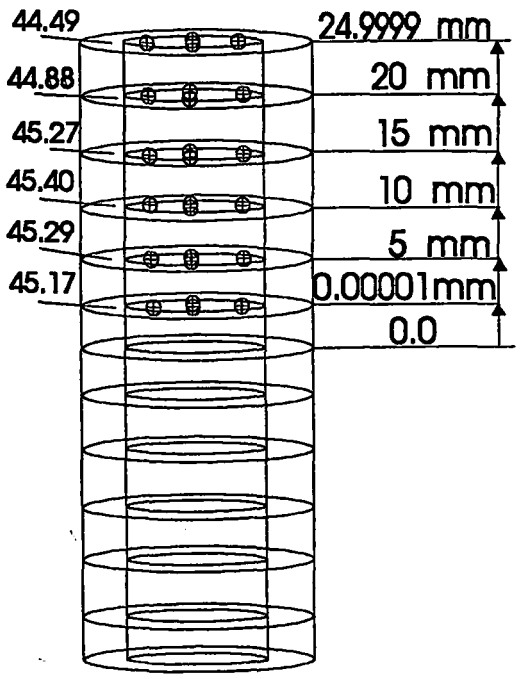

Figure 4.15: Maximum values of τ_{max} on the studied cross sections.

According to this theory and regarding the value of the shear stress for the matrix the chance of appearance of the matrix failure mode is relatively high, but the interface failure like that which was described for the maximum normal stress theory may happen first. Comparing the result of this criterion to the maximum normal stress theory indicates that the predictions under both the criteria are relatively the same.

4.2.2.4. Maximum Distortional Energy Criterion (von Mises)

This criterion is based on the modification of the maximum strain energy theory [27]. In 3-D state of stress it is expressed as

$$\sigma_v = [\frac{(\sigma_1 - \sigma_2)^2 + (\sigma_1 - \sigma_2)^2 + (\sigma_1 - \sigma_2)^2}{2}]^{0.5}$$

or in the form of normal stress components see Eq. (3.7). This theory predicts that failure occurs when

$$\sigma_v \geq \sigma_{uts}$$

See Figure 4.17 for graphically representation of the theory based on σ_{uts} =40 to 90 MN/m^2 for the matrix. The oblique elliptical cylinder encloses all safe values of the general stress state given by σ_1, σ_2, and σ_3.

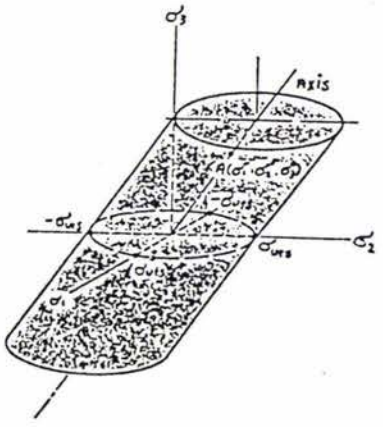

$|\sigma_{uts}| = |\sigma_{ucs}|$

σ_{uts} = 40 to 90 MN/m^2

Figure 4.17: Graphically representation of the maximum distortional energy theory. σ_1'', σ_2'', and σ_3'' represent the hydrostatic part of the principal stresses [27].

The maximum value of σ_v (σ_v = 90.71 MN/m2) for the model lies on section y=10 mm and happens on the fibre area (see Figure 4.18(a)). Figure 4.18(b) represents the distribution of the distortional energy through the matrix on section y=10 mm along three different lines.

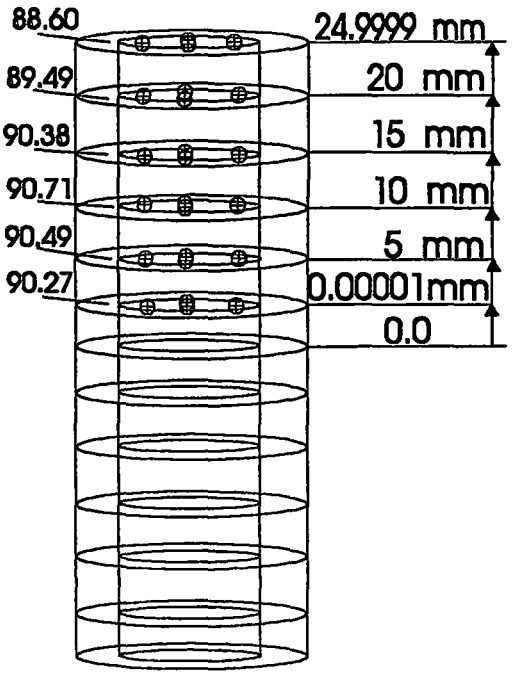

a) Maximum values of σ_v.

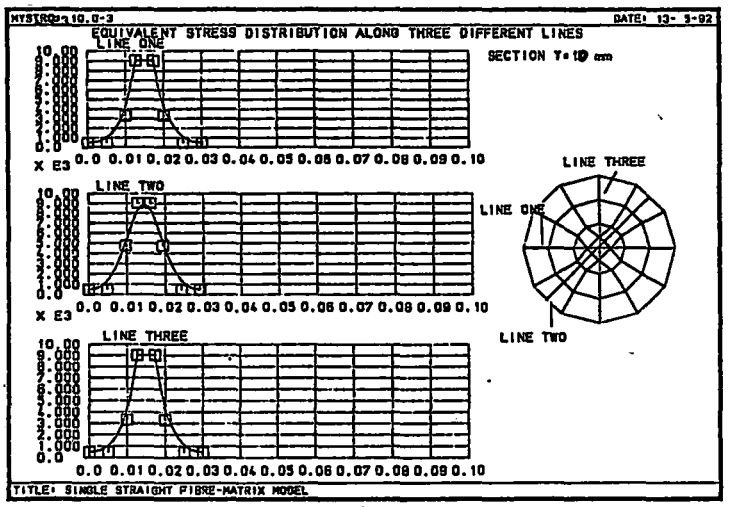

b) Distribution graph of σ_v on section y= 10 mm.

Figure 4.18:

It is clear that the maximum value of σ_v through the matrix happens right at the interface along the line two (σ_v = 50 MN/m2). This value lies on the boundary of the safe region of the criterion (see Figure 4.17). As with the maximum shear stress criterion the matrix and interface both are in critical situations. The same discussion can be considered for the failure of the composite under the maximum distortional energy theory.

4.2.2.5. Conclusion

It is concluded that for the single straight fibre-matrix model failure will initiate by debonding. The initiated crack may then either run through the matrix and finally the composite will be collapsed by appearing the fibre fracture mode or may run along the length of the interface and cause a fibre pull out phenomenon to happen. The possible path(s) of failure are shown in Figure 4.19.

It is also concluded that under the applied load (F=0.01 N) even the fibre is safe but the matrix is in a critical situation and further increasing of the load is not allowed.

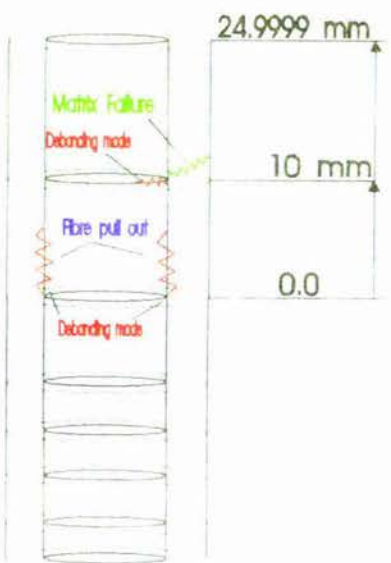

Figure 4.19: Predicted paths of failure for the straight fibre-matrix model.

4.3. Single Crimped Fibre Model

4.3.1. Stress Analysis

The stress distribution along the length and diameter of a single short fibre without matrix is uniform. Consider a straight fibre under the same load for the single crimped fibre model. The normal stress distribution graphs for any cross section of the fibre are shown in Figure 4.20.

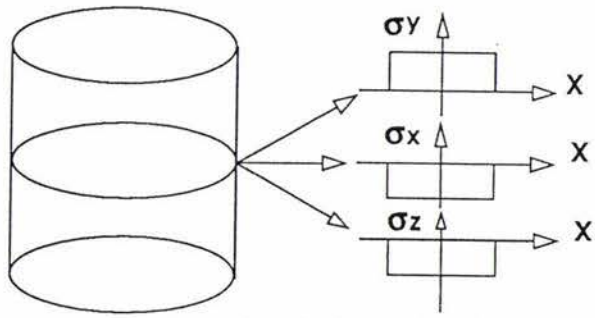

Figure 4.20. Normal stress distribution graphs for a short straight fibre.

In this subsection the effects of a crimp area on the distribution of normal and shear stress components, along the length and across the diameter of the fibre, will be studied.

4.3.1.1. Normal Stress in the y-Direction

A colour contour of the normal stress in the y-direction on the studied cross sections of the fibre is shown in Figure 4.21 (overleaf). Under the tension load the fibre tends to straighten out, therefore a tension stress region appears on the concave part of the crimped fibre, while on the convex part a compressive stress region is seen.

The reason for the appearance of the compressive stress at the middle section is shown in Figure 4.23. The reaction of the applied load at the middle section generates a momentum which causes a normal tensile stress in the concave part and a compressive normal stress in the convex part.

The magnitude of the compressive stress is related to the severity of the crimp because the generated momentum depends on the distance between the applied load and its reaction. This is why the compressive stress region disappears in the straight part of the fibre (see Figures 4.21 and 4.22). In this study the centre line of the fibre was bent equal to the radius of it's cross section (see Figure 4.23).

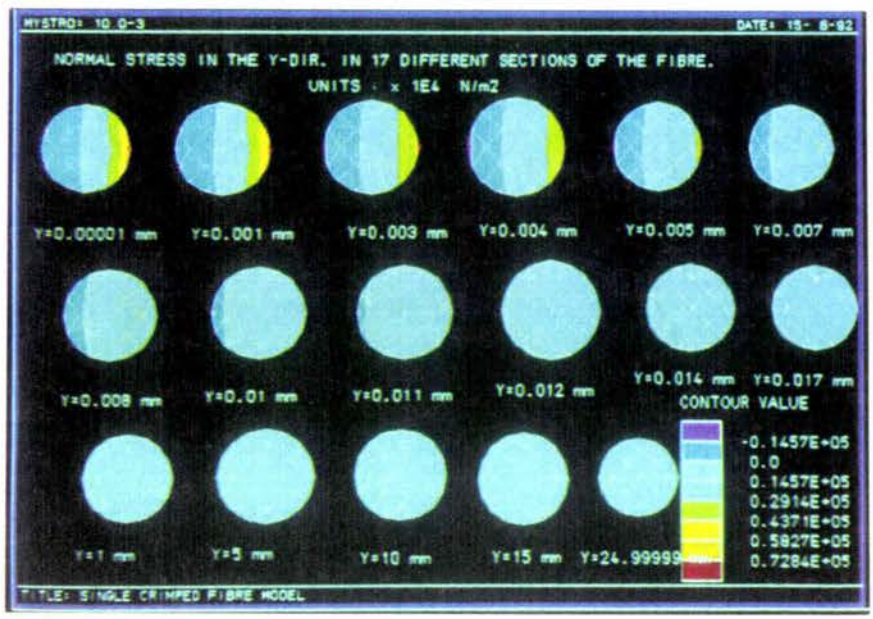

Figure 4.21: Colour contour of σ_y on the studied cross sections.

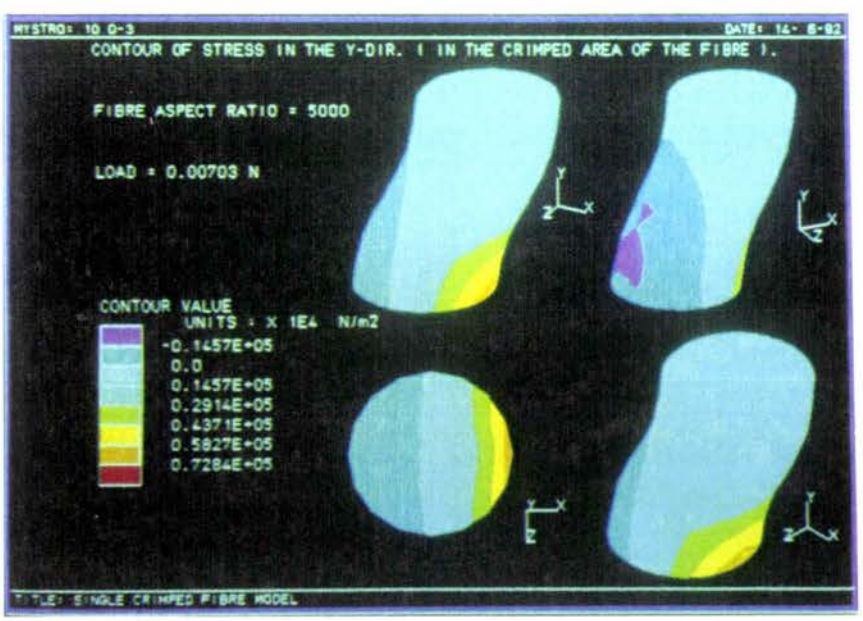

Figure 4.22: 3-D colour contour of σ_y in the crimped area.

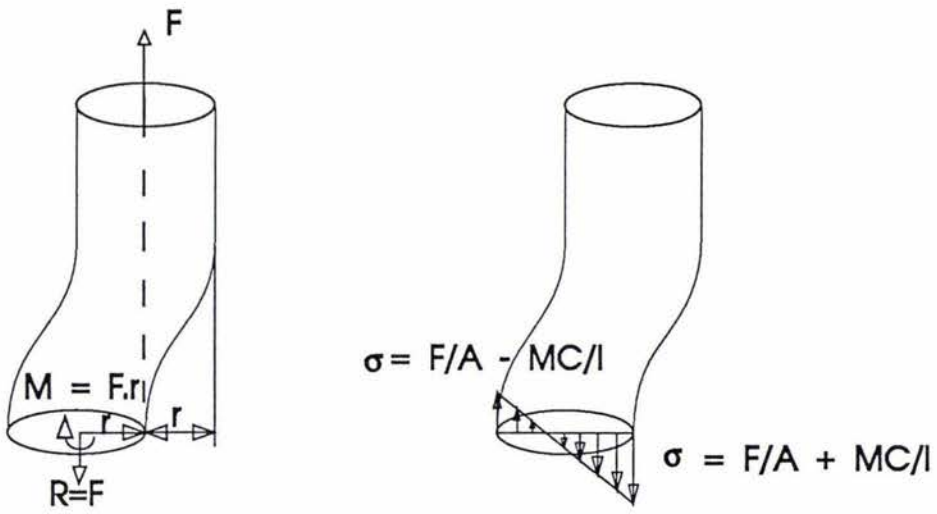

Figure 4.23. Normal stress situation in the y-direction at the middle of the crimp.

In the straight part of the fibre the effect of the crimp is gradually decreased until at about the end of the fibre a uniform distribution of σ_y appears. Figure 4.24 (overleaf) represents the distribution of σ_y in 12 sections of the model.

Comparing these graphs with the graph of Figure 4.20 for σ_y shows the severity of the deviation which a crimp could cause for the stress distribution. Comparing the value of σ_y for the straight fibre with the maximum value of σ_y which happens on the crimped fibre (see Figure 4.25 section y=0.00001 mm) gives a stress concentration factor of magnitude (SCF = 7.87). This value could play a major role in the failure of the model which will be discussed later.

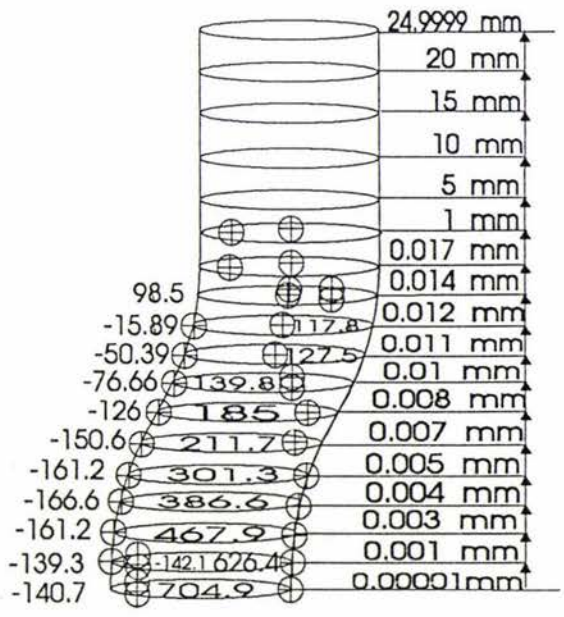

Figure 4.25. Maximum values of σ_y on the studied cross sections.

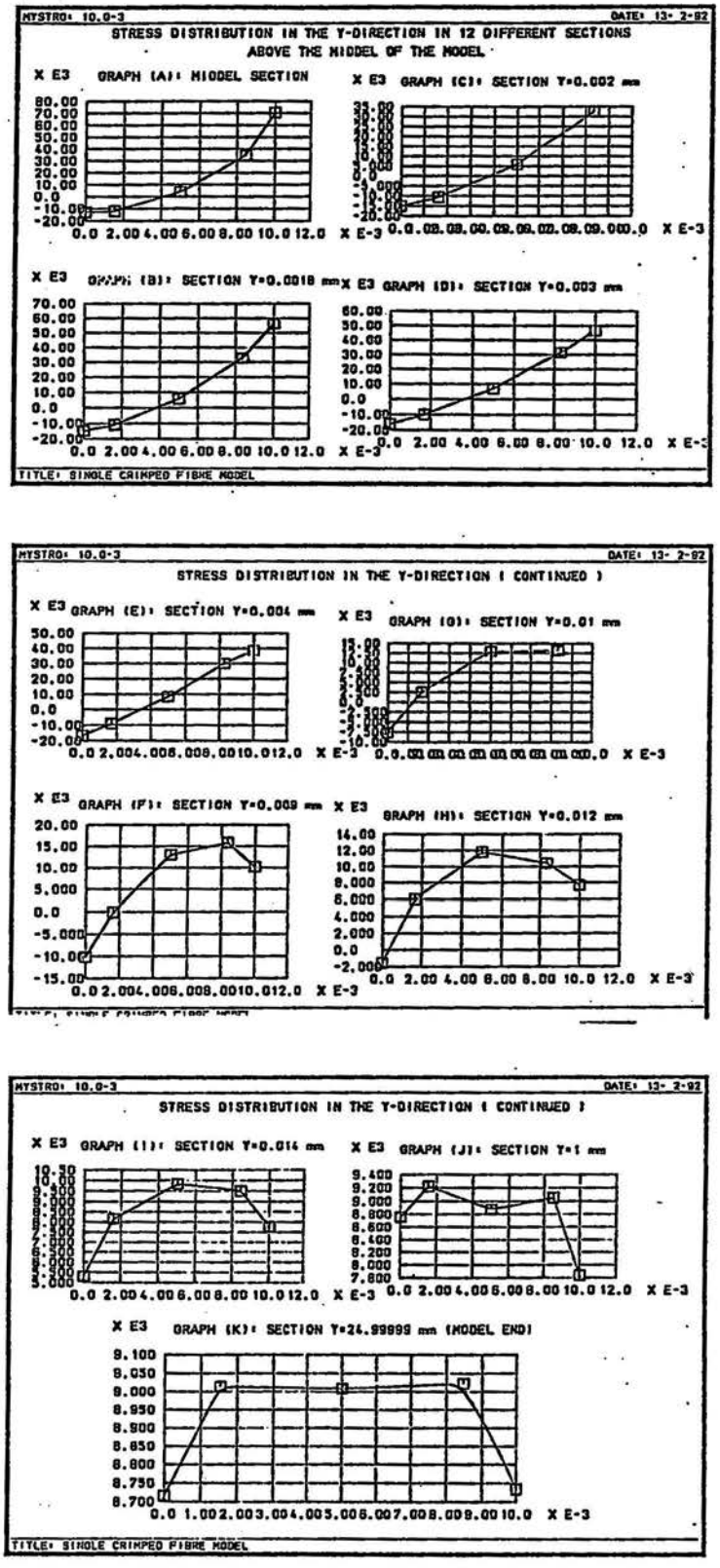

Figure 4.24. Distribution of σ_y on twelve sections of the crimped fibre.

4.3.1.2. Normal Stress in the x-Direction

Stress distribution in the x-direction of the crimped fibre is totally different to that of the straight fibre. Figures 4.26 and 4.27 (overleaf) show 3-D contours of σ_x in the crimped area and the stress contours on the studied sections respectively. As discussed the crimped fibre tends to straighten out. So the convex part of the crimp is under expansion while the concave part is under contraction. This causes a tensile region of σ_x to appear in the convex part and a compressive region in the concave part the same as σ_y (see Figure 4.26). Right in the middle of the crimp area, reaction of the applied load is perpendicular to the cross section. Therefore, it's component in the x-direction is zero (see Figure 4.28). As a result, on the middle cross section of the crimp area no compressive region of σ_x appears. Now for discussing the maximum tensile and compressive regions of σ_x in the crimped area a note must be made from section 3.2. As was explained the crimp area consists of two arcs (see Figure 3.2(b)). The load corresponding to the existing contraction and expansion regions in the crimped area are compressive and tensile respectively.

The reaction load of Figure 4.28 which could be tensile or compressive does not remain parallel to the y-direction when the straight part of the fibre is approached. The angle between the load and y-direction , θ , increases from the middle of the crimp until the end of the first curve and decreases to zero again from this section to the end of the second arc. Therefore the x-component of the tensile or compressive reaction load increases up to the end of the first curve and decreases again when the straight part of the fibre is approached. This is why the two maximum compressive and tensile regions of σ_x appear on section y=0.007 mm (see Figures 4.26 and 4.27).

According to the effect of Poisson's ratio and due to the tensile σ_y in the straight part of the fibre a compressive σ_x is expected in this part. This might be the effect of the crimped area which disturbs the reaction force and changes it's direction. The inclination is such that the load makes tensile components in the x and z-directions which generate tensile regions of σ_x and σ_z in the straight part of the fibre.

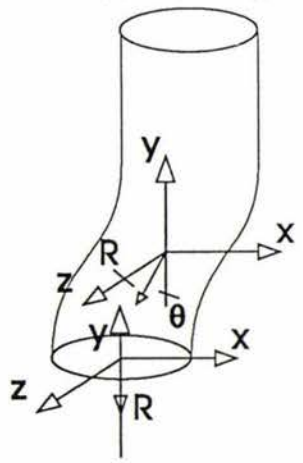

Figure 4.28: Representation of the reaction load direction in the crimped area.

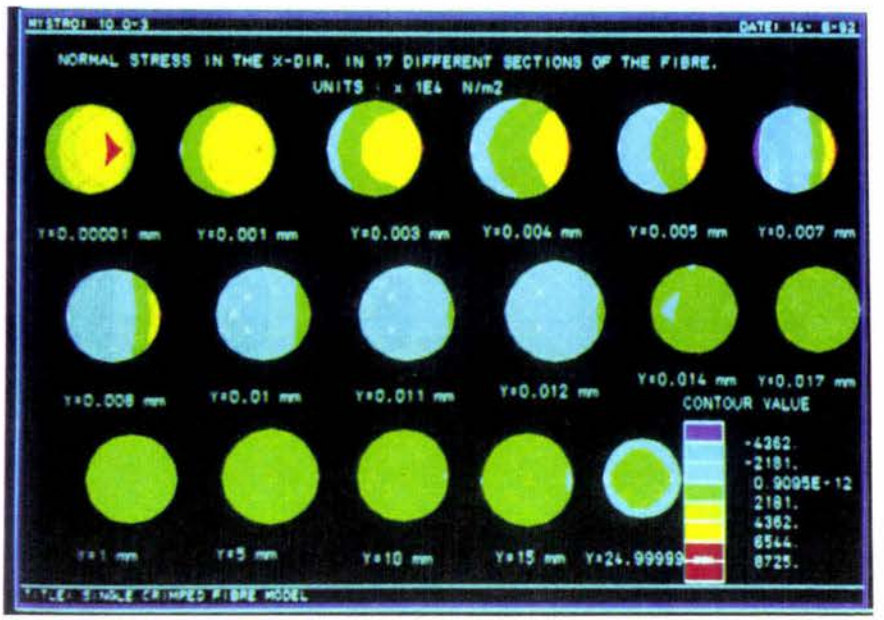

Figure 4.26: Contour of σ_x on the studied cross sections.

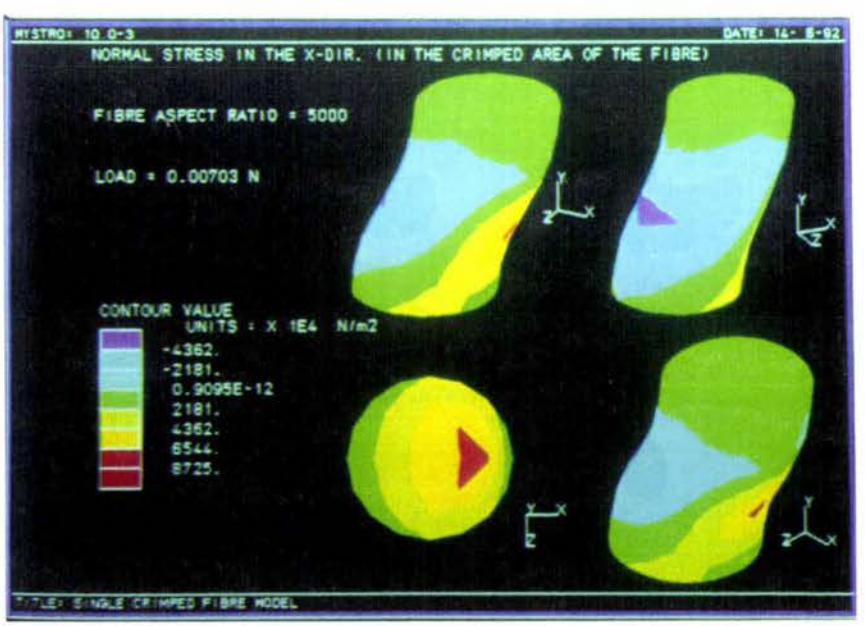

Figure 4.27: 3-D contour of σ_x in the crimped area.

4.3.1.3. Normal Stress in the z-Direction

The stress distribution in the z-direction of the crimped fibre like the x-direction is essentially different to that of the straight fibre (See Figure 4.20).

As Figure 4.29 (overleaf) shows due to the same reason as σ_x, a tensile region of σ_z appears on the straight part of the fibre. The status of the stress from section y=0.012 mm to the middle of the crimp can be explained with the same reasoning as for σ_x (taking into account a small inclination of the reaction load). The inclination causes the reaction load to have a compressive component in the z-direction in the concave part and in the convex part from section y=0.007 mm up to the straight part of the fibre. The situation of the reaction load from the middle of the crimp up to the section y=0.007 mm in the convex part is similar to the load situation for σ_x in this area.

The exceptional tensile region of σ_z in the concave part of the crimp (see Figures 4.29 and 4.30) can be explained with the Poisson's ratio effect. As Figures 4.21 and 4.23 show, a compressive region of σ_y appears at section y=0.00001 mm. This in turn, due to the Poisson's ratio effect, could cause a tensile region of σ_z in this area (note that the reaction load is perpendicular to this area). The tensile region gradually disappears with the increasing of the compressive component of the reaction load in the z-direction from the middle to the section y=0.007 mm.

Another exception is the compressive region in the centre of the fibre in the middle of the crimp. This is not expected because the reaction load does not create a z-component on this section. It can be explained with the same reason as for the tensile region of σ_z.

As the distribution graph of σ_y in the middle section in Figure 4.24 shows the value of σ_y at about the centre of the fibre is about zero. While at the same position a tensile region of σ_x exists (see Figure 4.27). As a result, due to Poisson's ratio a compressive region of σ_z appears in this area. See Appendix E for the maximum value of σ_z on the studied cross sections and for comparing the distribution graphs of σ_z with the graph of Figure 4.20.

4.3.1.4. Shear Stress on the xy-Plane

The shear stress situation of the model is more complicated than the normal stress components. It is attempted to explain the situation using the normal stress situation of the model.

Figure 4.31 shows the predicted load situation in both the convex and concave parts of the crimped area based on the results of sections 4.3.1.1 to 4.3.1.3.

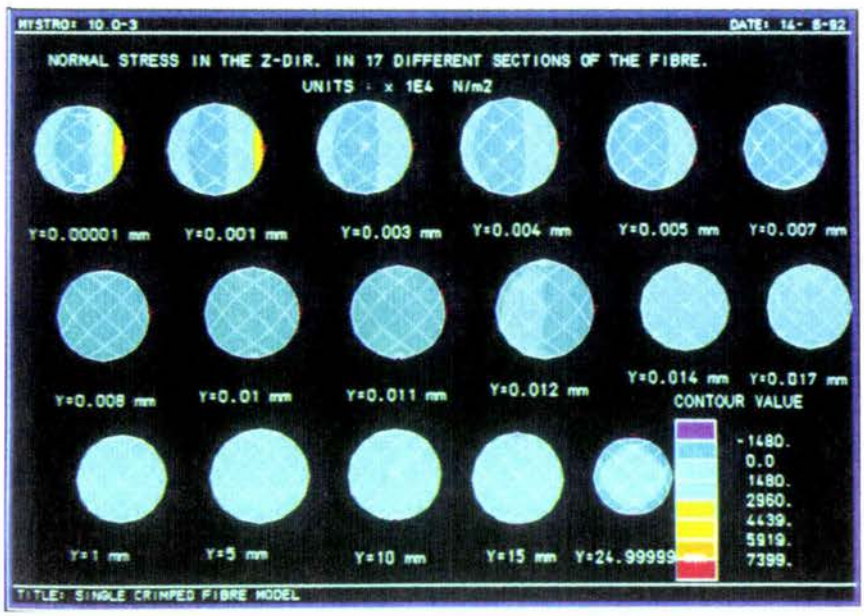

Figure 4.29. Colour contour of σ_z on the studied sections of the fibre.

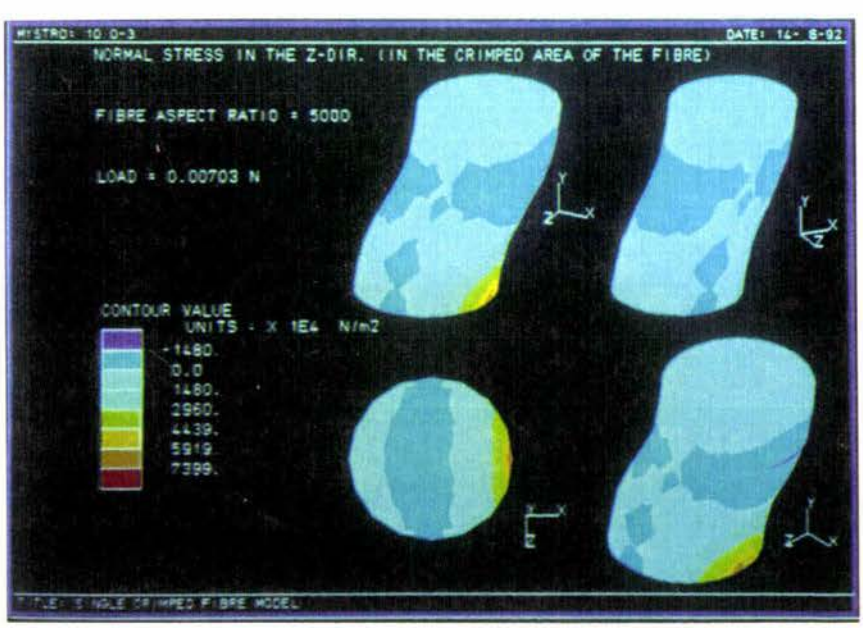

Figure 4.30: 3-D contour of σ_z in the crimped area.

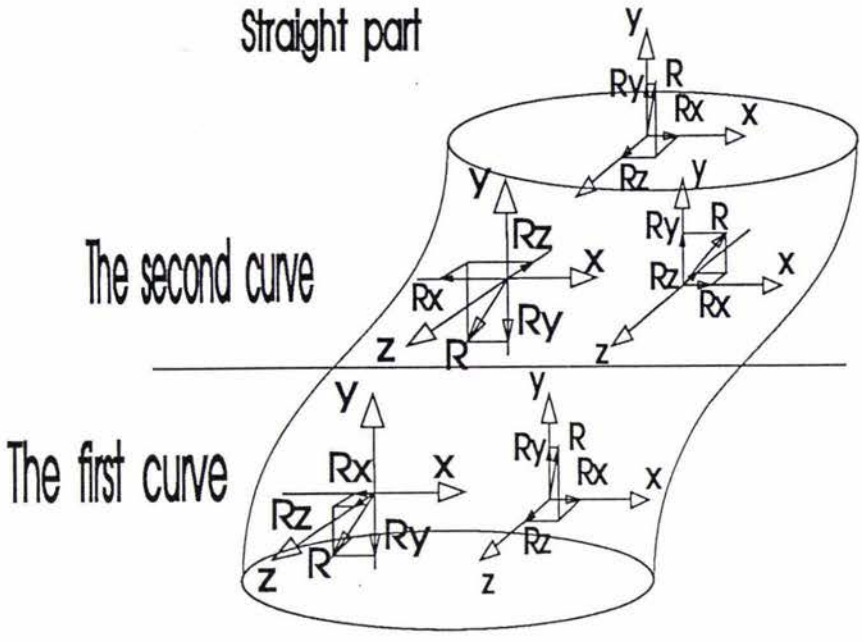

Figure 4.31: Load situation in the crimped area of the fibre.

A colour contour of τ_{xy} on the studied sections of the model and a 3-D contour for the crimped area are shown in Figures 4.32 and 4.33 (overleaf) respectively.

As Figure 4.31 shows, the reaction load components in both the x and y-directions on the xy-plane are compressive for the concave part and are tensile for the convex part. The compressive loads cause a compressive shear stress while the tensile loads cause a tensile shear stress on the xy-plane (see Figure 4.33).

4.3.1.5. Shear Stress on the xz-Plane

The load situation in the x and z-directions of Figure 4.31 show that a similar situation as τ_{xy} must occur for τ_{xz} , but as Figures 4.34 and 4.35 show, it is actually different. This can be explained with the generated torsions by the components of the reaction load in both the concave and convex parts (taking into account the sign of the torsions). Figure 4.36 shows the torsions and their signs.

The negative and positive torsions in the concave and convex parts change the situation of τ_{xz} in the crimped area respectively. As Figure 4.34 shows, instead of a tensile region of τ_{xz} appearing on the first and second quadrants, two compressive and tensile regions of it appear on the first and second quadrants respectively (see also Figure 4.37(a)) .

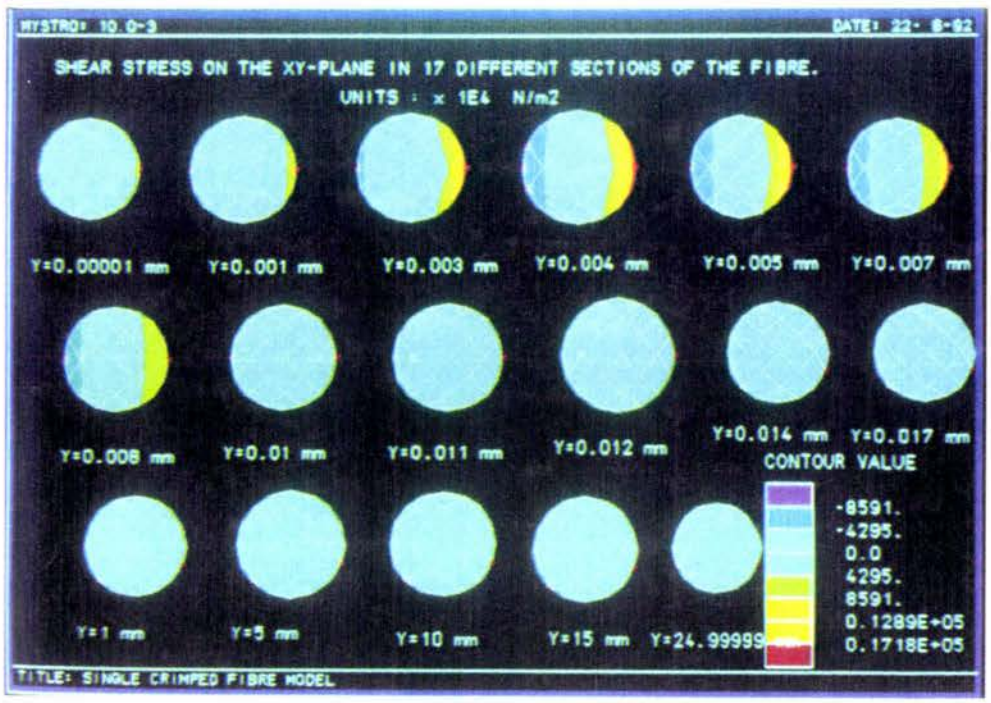

Figure 4.32: Colour contour of τ_{xy} on the studied cross sections.

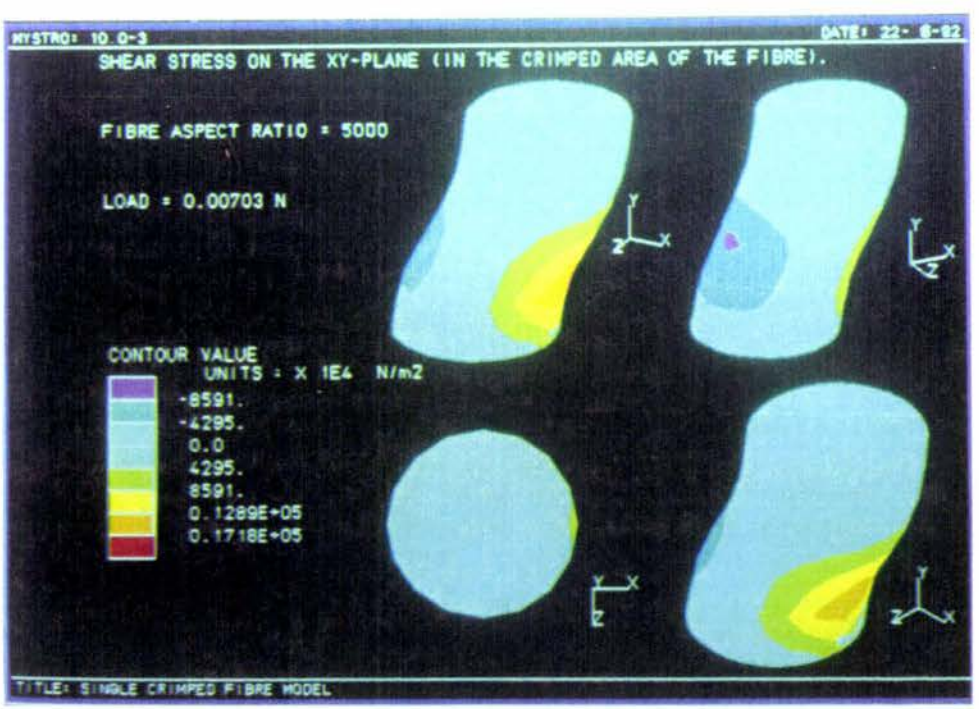

Figure 4.33: 3-D contour of τ_{xy} for the crimped area.

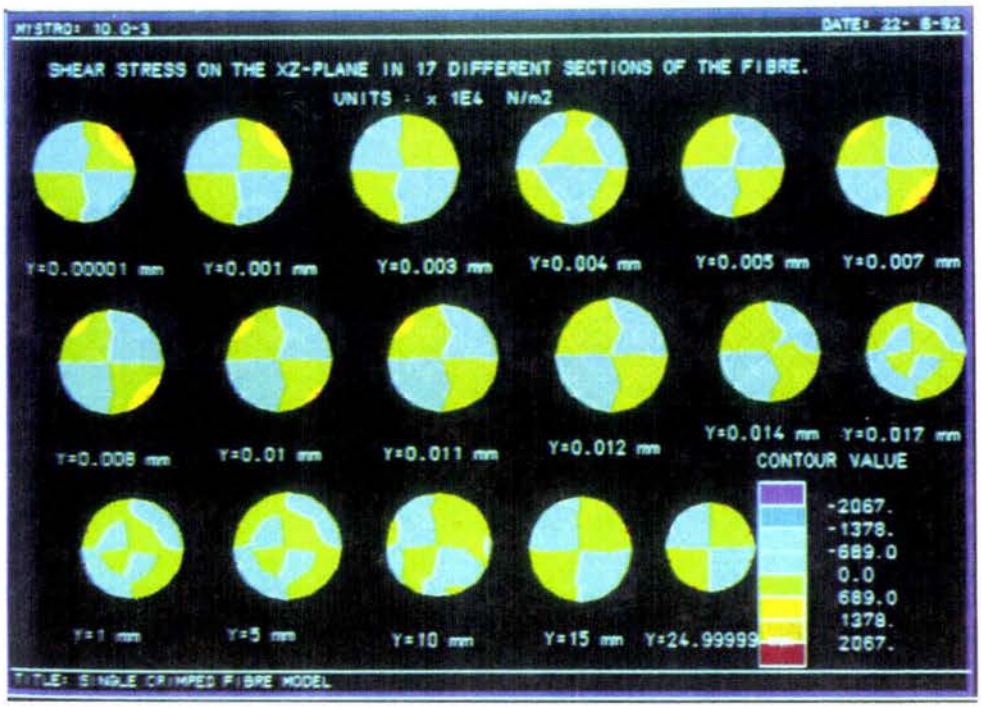

Figure 4.34: colour contour of τ_{xz} on the studied sections of the model.

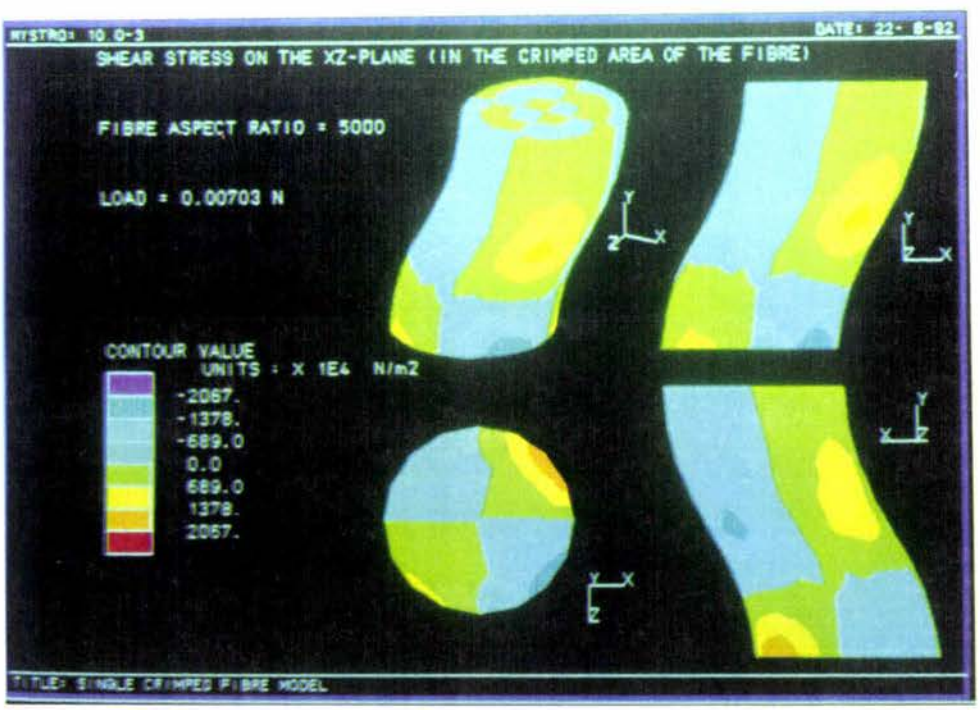

Figure 4.35: 3-D contour of τ_{xz} for the crimped area.

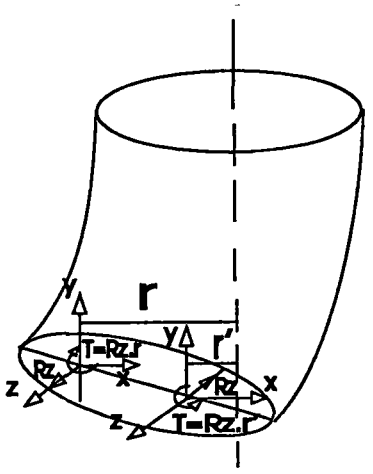

Figure 4.36: The generated torsions by the z-component of the reaction load.

As the direction of the z-component of the reaction load at about section y=0.006 mm to the straight part in the convex area changes, the sign of τ_{xz} is also changed (see Figures 4.37(b) and 4.34).

a) *b)*

Figure 4.37: The sign of τ_{xz} on the crimped area.

4.3.1.6. Shear Stress on the yz-Plane

The sign of the x-component of the reaction load is similar to the y-components in both the convex and concave parts of the crimped area. Therefore a similar situation as τ_{xz} happens for τ_{yz} with different values (see Figures 4.37 and 4.38) except the situation remains unchanged along the length of the fibre.

A little difference in the shape of the contours in Figures 4.37 and 4.34 might be due to the different values for the y and x-components of the reaction load.

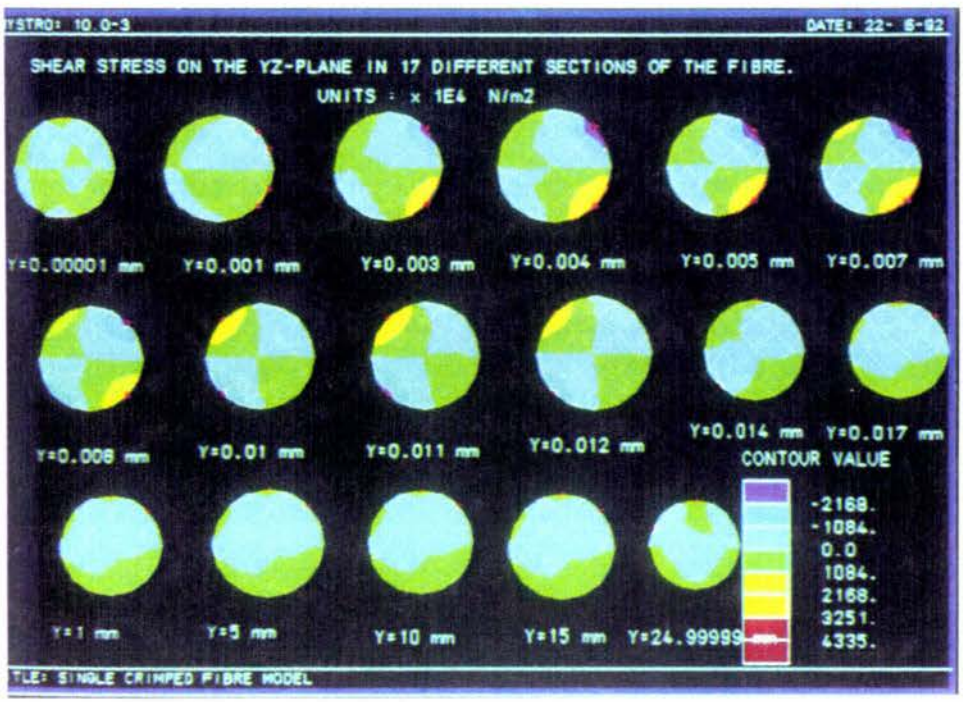

Figure 4.38: Colour contour of τ_{yz} on the studied cross sections.

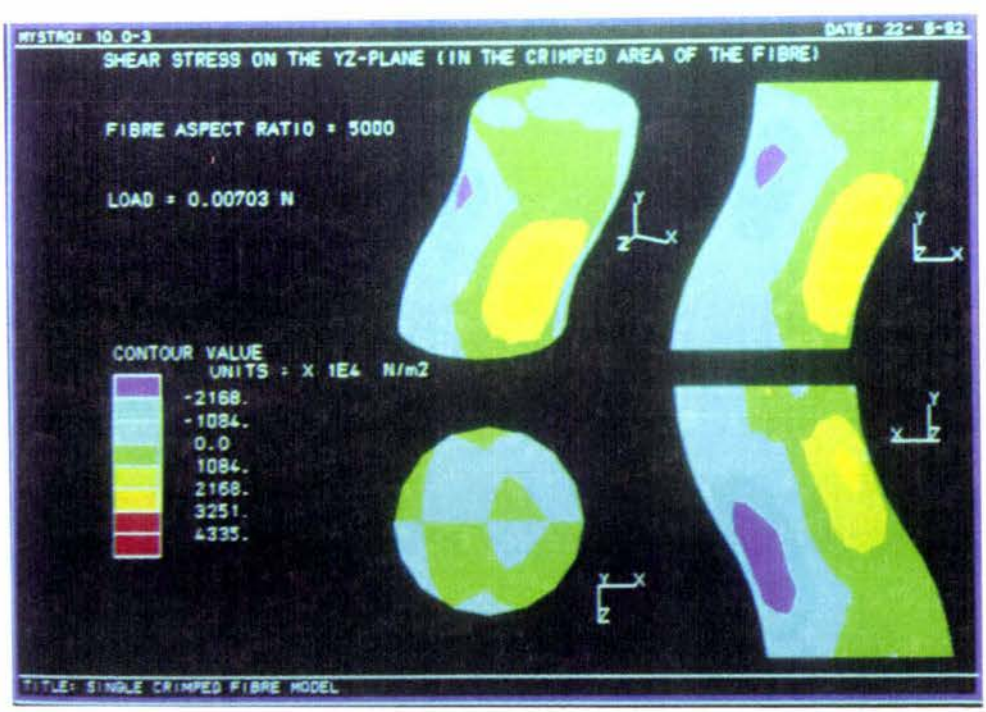

Figure 4.39: 3-D contour of τ_{yz} for the crimped area.

4.3.2. Failure Analysis

Failure analysis of a single crimped fibre is important for studying the matrix effects in the failure of a composite. Figure 4.39 shows the maximum values of the maximum principal stress on the studied cross sections.

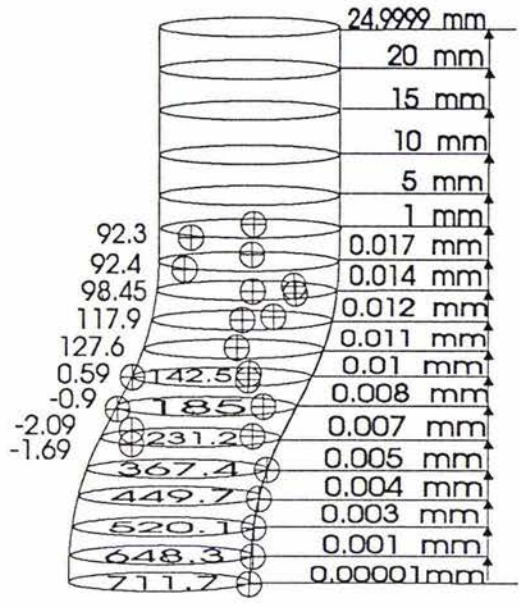

Figure 4.40: Maximum values of σ_1 on the studied cross sections.

As the maximum value of σ_1 happens in the middle of the crimp and according to the maximum normal stress criterion

$$711.7 \text{ MN/m}^2 < 3450 \text{ MN/m}^2$$

the fibre will fail at the middle of the crimp with the increasing of the load. Similarly based on the maximum strain criterion, failure will happen at section y=0.00001 mm with the increasing of the load

$$\varepsilon_1 = 0.00915 < \varepsilon_{uts} = 0.0454$$

See Figure 4.40(a) for the position and values of the maximum ε_1 (maximum principal strain).

The last important subject of the single crimped fibre model is about the position of the maximum shear stress. As Figure 4.40(b) shows, the maximum value of τ_{max} happens at the middle of the crimped area right on the outer ring of the fibre. It may initiate a crack and as Figure 4.41 shows the initiated crack could run through the fibre diameter and cause the fibre to fail with the increasing of the load. The possible path of failure is shown in Figure 4.42.

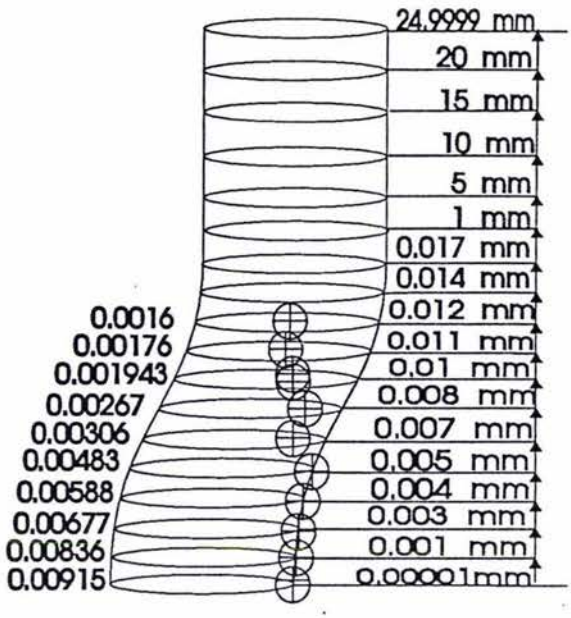

(a): Maximum principal strain.

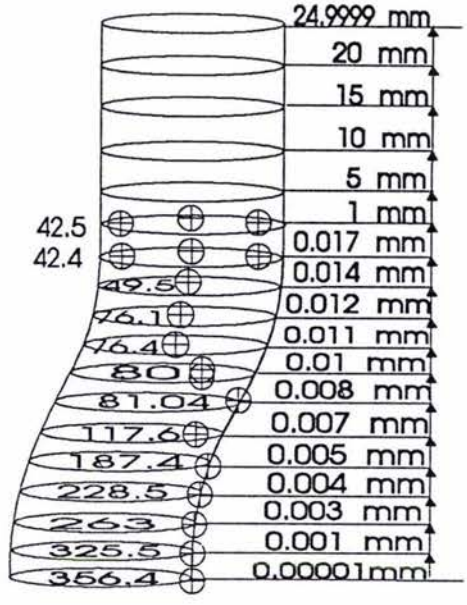

(b): Maximum shear stress.

Figure 4.41:

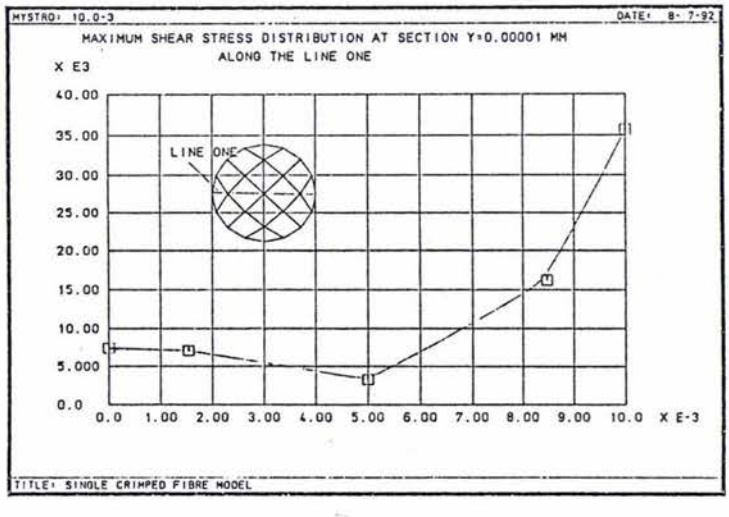

Figure 4.42: Maximum shear stress distribution at section y=0.00001 mm.

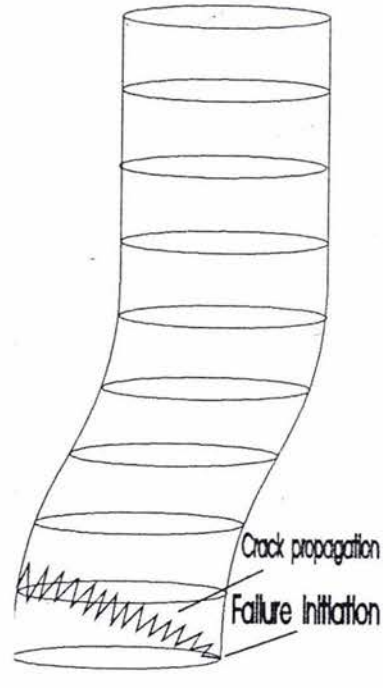

Figure 4.43: Predicted path of failure for the crimped fibre.

4.4. Interlaced Fibres Model

4.4.1. Stress Analysis

In order to perform a study on the stress and failure situations of two interlaced fibres a weft fibre was designed in the crimp area of the single crimped fibre model. The designed weft fibre prevents the movement of the warp fibre in all directions which causes a compressive load on the warp fibre (see Figure 4.44). This compressive load changes the stress status of the single crimped fibre in all directions in the crimped area.

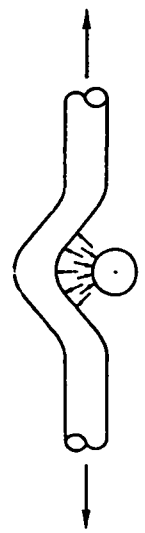

Figure 4.44: Representation of the compressive load in the connection point of the fibres.

4.4.1.1. Normal Stress in the y-Direction

The situation of σ_y except in the contact area of the fibres is similar to the single crimped fibre model (SCFM) (see Figure 4.45 (overleaf)). As Figure 4.46 (overleaf) shows, right in the middle of the crimp instead of appearing a maximum region of σ_y, as in Figure 4.21 for SCFM, a drop for the value of σ_y is seen. This drop changes the value and position of the maximum of σ_y, 22.5° about the centre of the warp fibre cross section, relative to the SCFM. This stress situation remains unchanged up to section y=0.005 mm and after that a similar situation as in Figure 4.21 appears on the studied cross sections. Figure 4.47 shows the distribution of σ_y at the middle of the crimp in the same position as Figure 4.24.

The compressive load which was discussed in section 4.4.1 causes the drop in the distribution curve of σ_y. The existing tensile load in the concave part of the crimp is high enough (see the values of σ_y for SCFM in Figure 4.25) for the compressive component of the connection load in the y-direction not to be able to generate a compressive stress region. The maximum values of σ_y on the studied cross sections are shown in Figure 4.48.

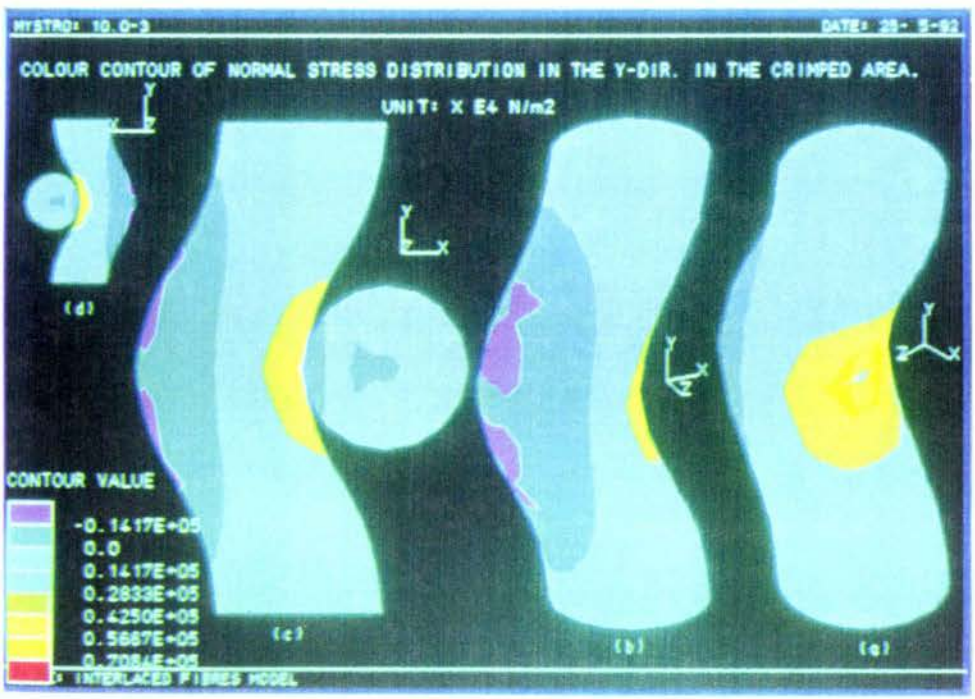

Figure 4.45: 3-D colour contour of σ_y in the crimped area.

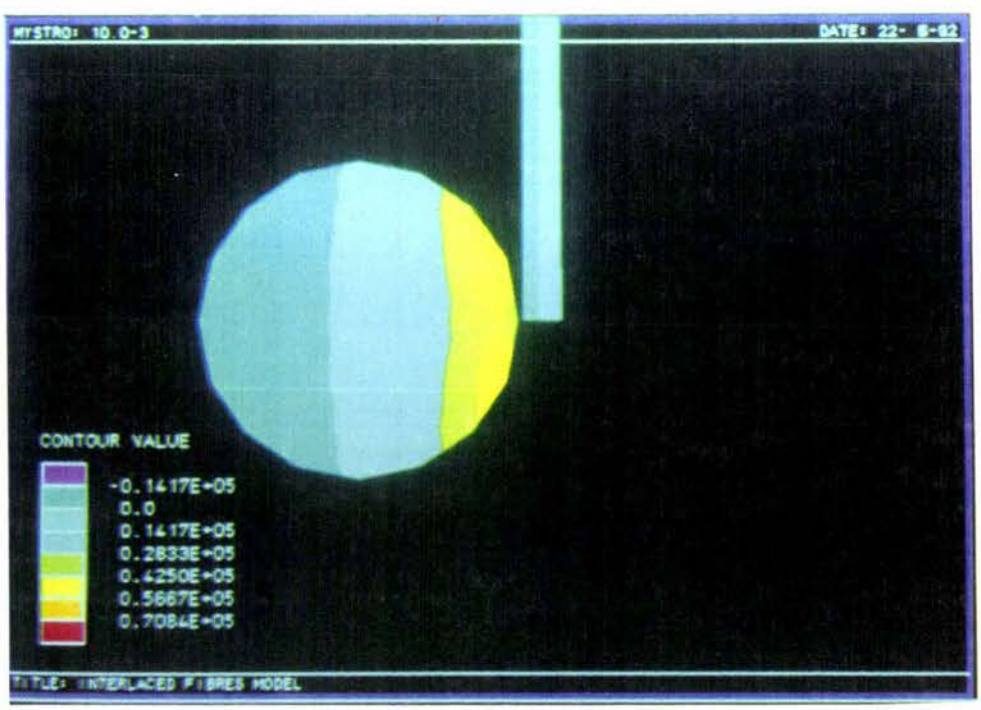

Figure 4.46: Colour contour of σ_y on middle cross section of the crimp.

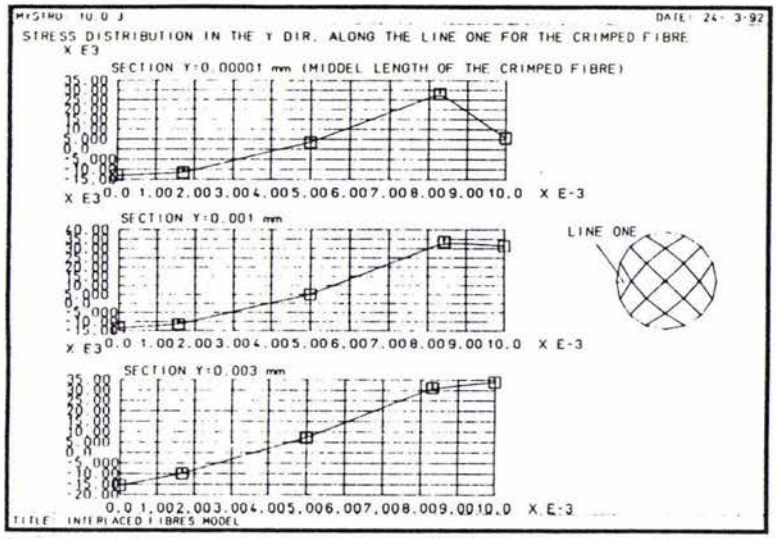

Figure 4.47: Distribution of σ_y on the middle cross section of the crimp.

Comparing the maximum value of σ_y with its theoretical value gives a stress concentration factor of magnitude (SCF = 7.62). This value of S.C.F. shows a decrease relative to the value for SCFM. Figures 4.45(c) and (d) show a compressive region of σ_y on the weft fibre right at the connection point. This is explained by the fact that the reaction of the connection load is also a compressive load on the weft fibre.

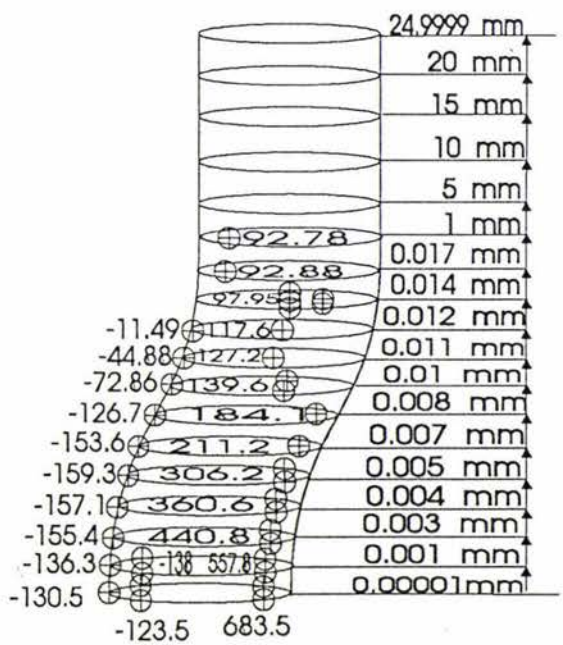

Figure 4.48: Maximum values of σ_y on the studied cross section.

4.4.1.2. Normal Stress in the x-Direction

The same as σ_y, a small difference is seen for σ_x relative to the results of SCFM. Most of the changes in the distribution of σ_x happen on the middle of the crimp and on section y=0.001 mm. Ignoring the difference between the values, the situation of σ_x for this model can be explained with the same reasons as for SCFM.

Figure 4.49 shows a 3-D colour contour of σ_x in the crimped area. This figure is very similar to Figure 4.27 except in the middle of the crimp area. The x-component of the compressive load in the connection point of the fibres is high such that it can change the sign of the σ_x region next to this point (see Figures 4.50(a) and (b)).

Above the section y=0.001 mm the value of the compressive load shows a big decrease such that a tension region of σ_x appears in the crimp area similar to that seen in Figure 4.26.

4.4.1.3. Normal Stress in the z-Direction

The effect of the weft fibre on σ_z is the same as σ_y which was discussed in section 4.4.1.1. The described reasons for the stress distribution for the single crimped fibre model are valid for this model except for the middle section and section y=0.001 mm. The weft fibre causes the position of the maximum value of σ_z to be replaced, relative to SCFM, by generating a compressive region of σ_z right at the connection point.

As Figures 4.51(a) and (b) show, the maximum value of σ_z appears at 45° to the horizontal line of the cross section. This phenomenon disappears above section y=0.001 mm and a similar situation as in Figure 4.29 happens for the rest of the studied sections. A 3-D contour of σ_z for comparing with Figure 4.30 is presented in Figure 4.52.

Figure 4.49: 3-D colour contour of σ_x in the crimped area.

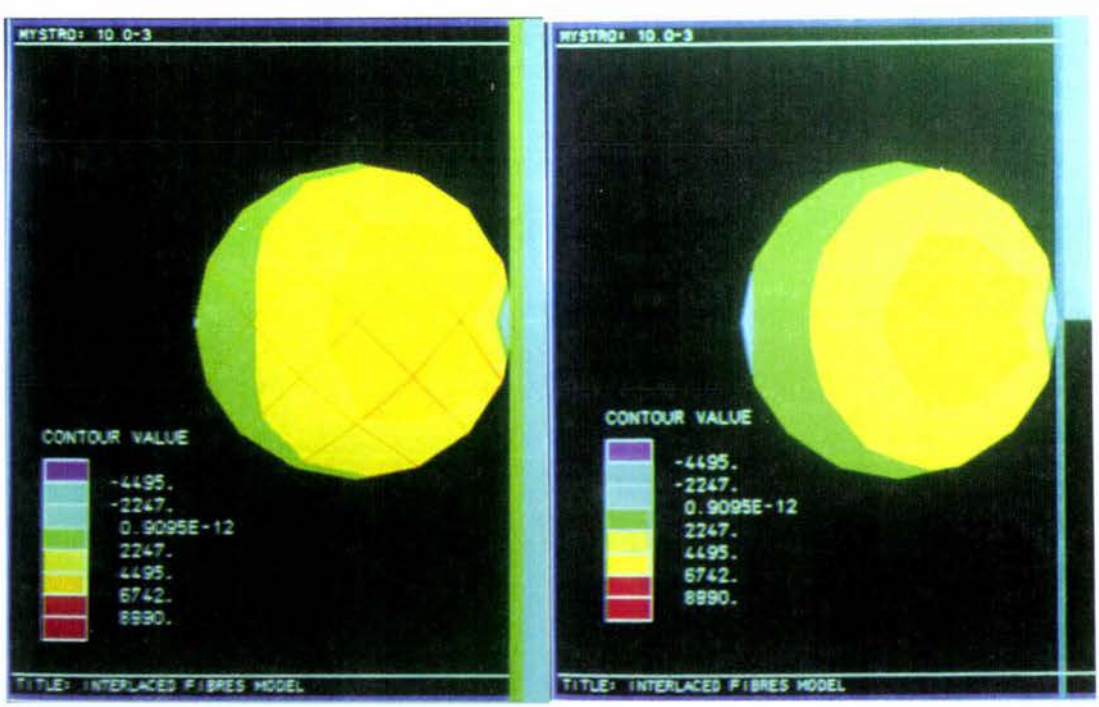

a) Middle of the crimp. *b) Section y=0.001 mm.*

Figure 4.50: Colour contour of σ_x on two cross sections in the crimped area of the fibre.

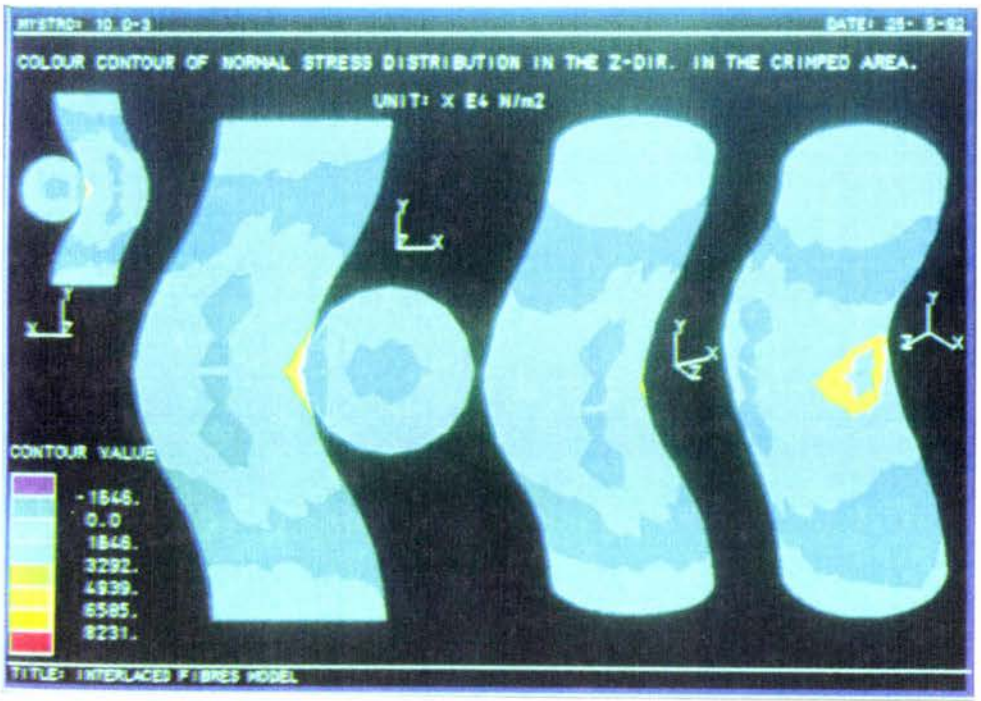

a) Middle of the crimp. *b) Section y=0.001 mm.*

Figure 4.51: Colour contour of σ_z on two cross sections in the crimped area of the fibre.

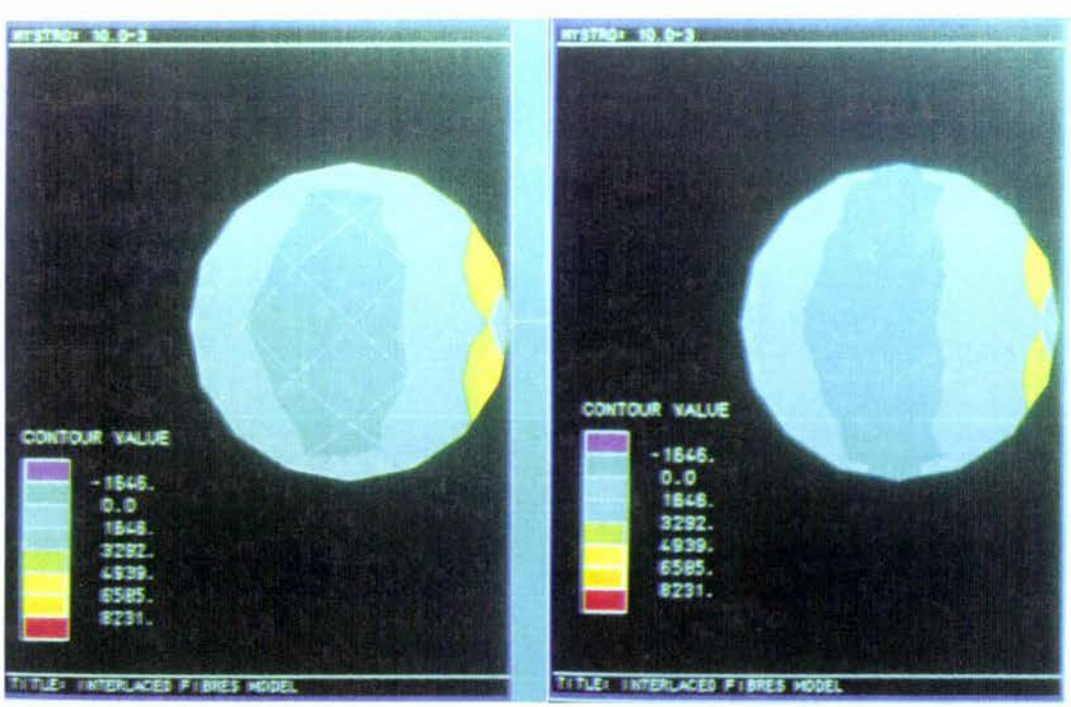

Figure 4.52: 3-D colour contour of σ_z in the crimped area.

4.4.1.4. Shear Stress on the xy-Plane

The situation of τ_{xy} is the same as SCFM (see Figures 4.53 (overleaf) and 4.33) except for the middle of the crimp and section y=0.001 mm (see Figures 4.54(a) and (b) (overleaf) and Figure 4.32). As Figure 4.54(a) shows a compressive region of τ_{xy} appears on the region next to the connection point and gradually disappears when the end of the first curve is approached. Appearance of the compressive region can be explained by the fact of the compressive connection load between the fibres. As a result of the compressive load, a compressive region of σ_z (see Figure 4.50) and a small tensile σ_y (see Figure 4.47) appear on this area which can change the situation of τ_{xy} for the area. Figure 4.53 shows that in the lower half of the crimp, in both the convex and concave parts equal values of τ_{xy} but with different signs appear. That is because the origin of the local xyz-axes was placed on the middle of the crimp.

Figure 4.55 shows that despite the different signs of the shear stress components in both halves of the crimp, a symmetric maximum shear stress appears in the crimp area.

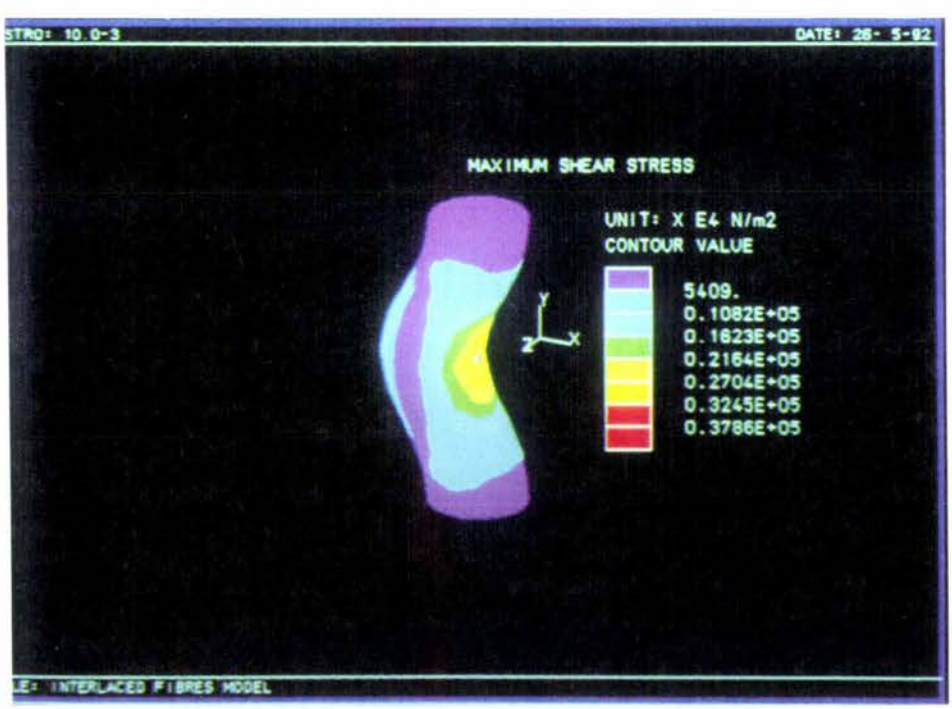

Figure 4.55: 3-D colour contour of τ_{max} in the crimped area.

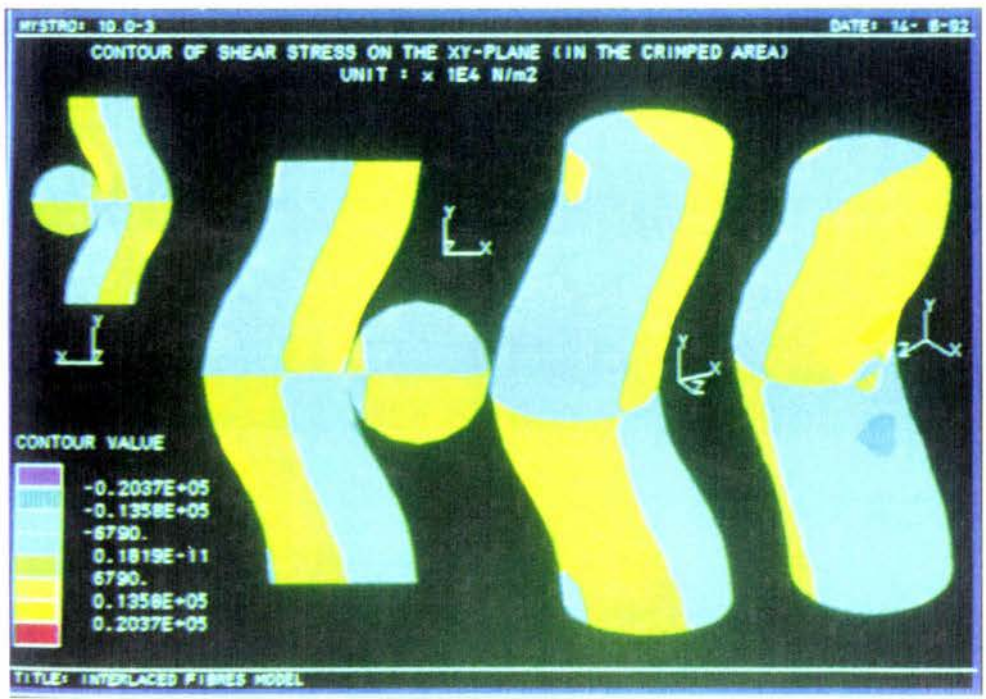

Figure 4.53: 3-D colour contour of τ_{xy} in the crimped area.

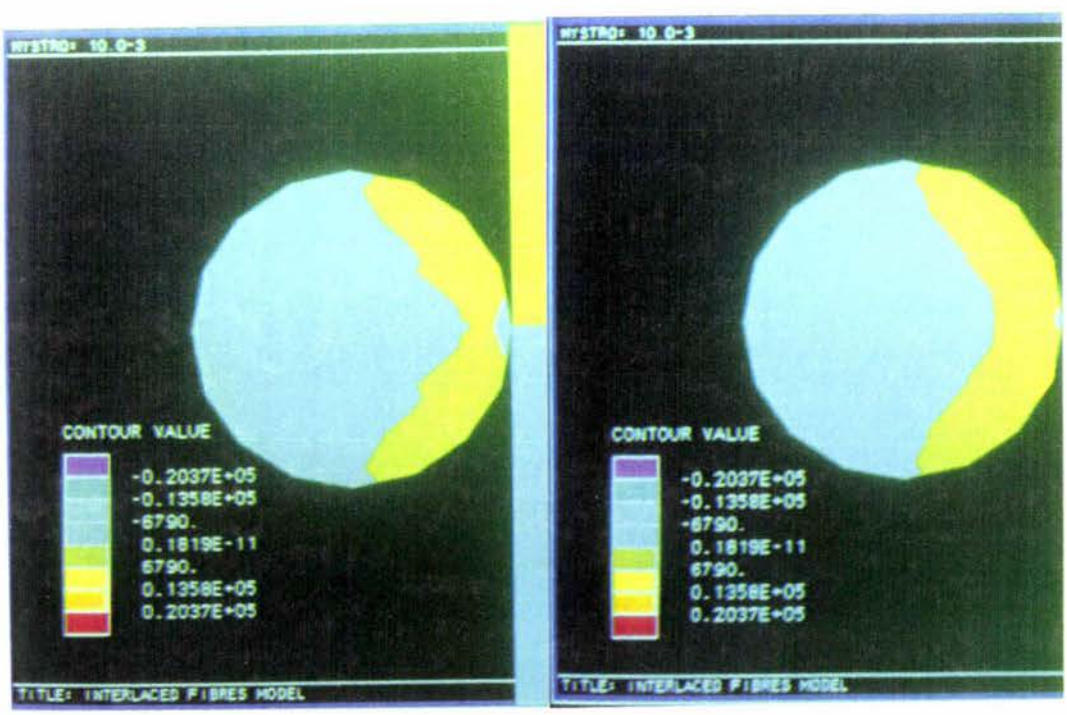

a) Middle of the crimp. *b) Section y=0.001 mm.*

Figure 4.54: Colour contour of τ_{xy} on two cross sections in the crimped area of the fibre.

4.4.1.5. Shear Stress on the yz-Plane

The situation of τ_{yz} for this model is similar to SCFM (see Figures 4.56 and 4.38) except the magnitudes differ.

Figures 4.57(a) and (b) (overleaf) show that the position and values of τ_{yz} are changed by the compressive connection load between the fibres. It also causes the manifestation of different values for the described torsion in section 4.3.1.5.

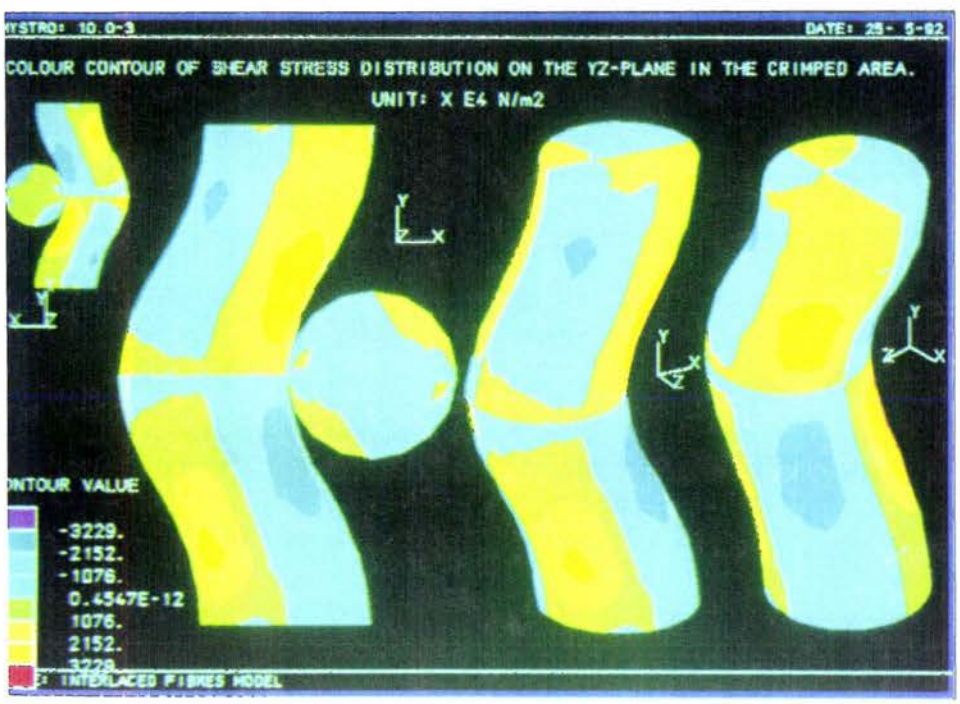

Figure 4.56: 3-D colour contour of τ_{yz} in the crimped area.

4.4.1.6. Shear Stress on the xz-Plane

Comparing Figures 4.58 (overleaf) and 4.35 indicate that a similar situation as for SCFM happens for τ_{xz} with the interlaced fibres. The exception here is a small difference between the values and position of the maximum which is seen in the middle of the crimp and section y=0.001 mm (see Figures 4.59(a) and (b) for comparison of the values). The same reason as in section 4.4.1.5. can cause the changes.

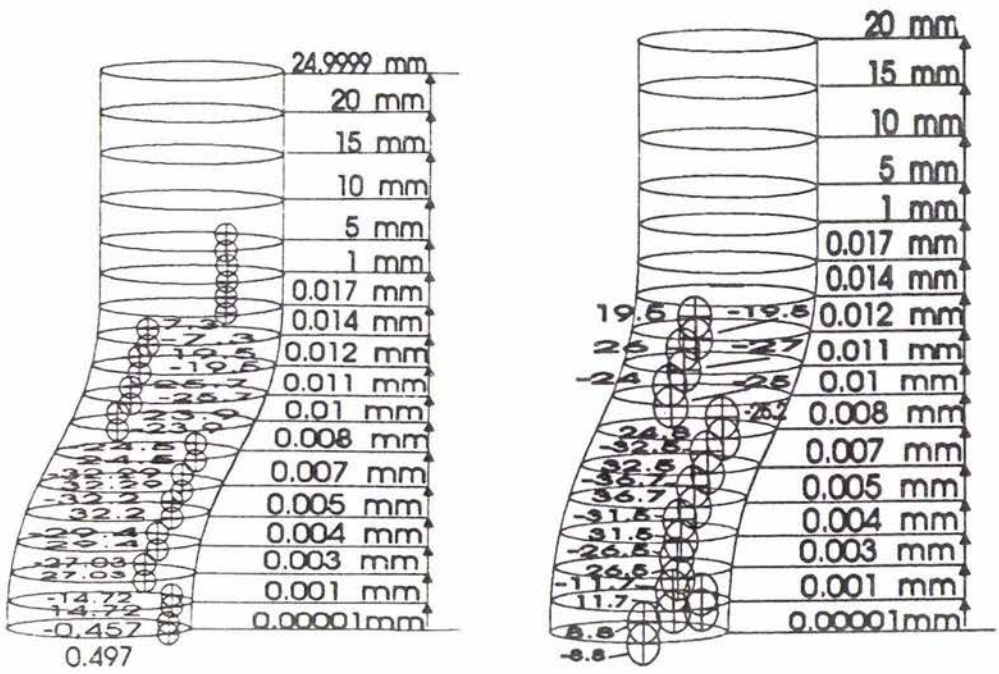

a) Interlaced fibres model *b) Single crimped fibre model*

Figure 4.57: Maximum values of τ_{yz} on the studied cross sections.

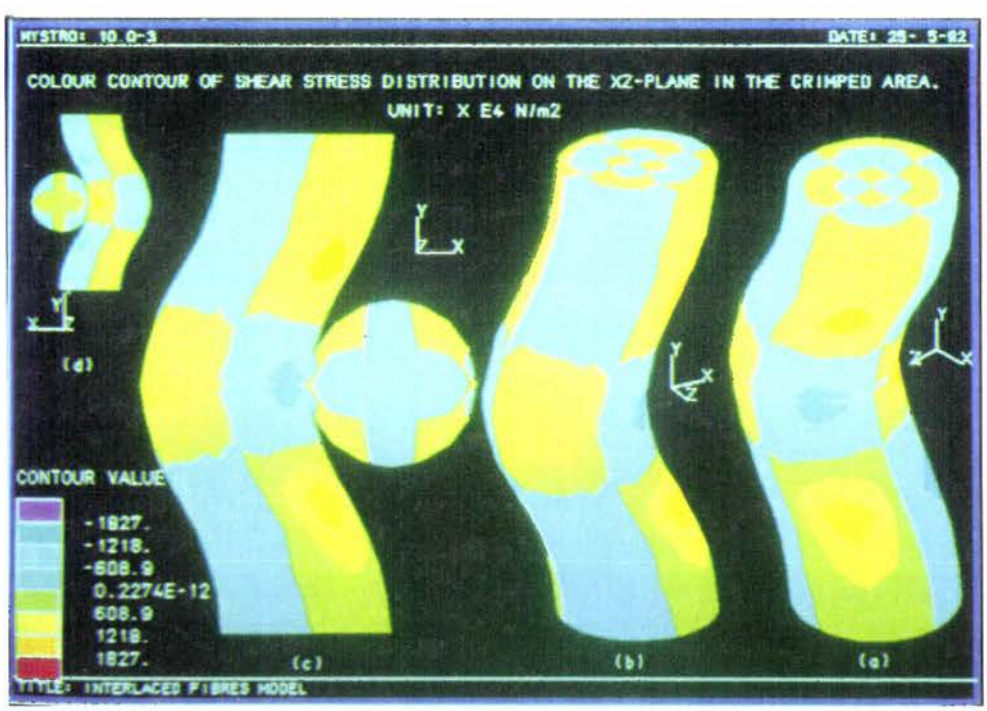

Figure 4.58: 3-D colour contour of τ_{xz} in the crimped area.

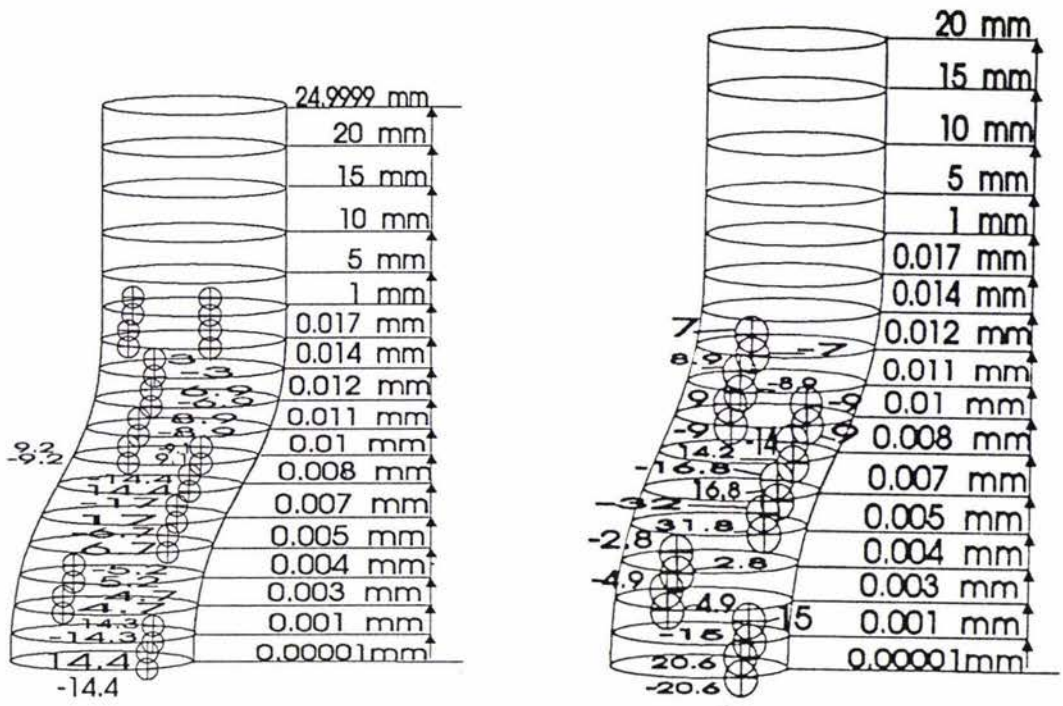

a) Interlaced fibres model *b) Single crimped fibre model*

Figure 4.59: Maximum values of τ_{xz} on the studied cross sections.

4.4.2 Failure Analysis

Applying the maximum normal stress criterion shows that with the increasing of the applied load the crimped fibre will fail like the SCFM from the middle of the crimp area. The only difference is that failure may initiate in two points because there are two maximum regions of σ_1 on this cross section (see Figure 4.60(b)). Therefore, while the SCFM fails from the middle of the crimp, the crimp fibre of the interlaced fibres model fails at 22.5° and -22.5° to the contact point of the fibres on the middle cross section of the crimp (see Figures 4.60(a) and 4.25).

According to the maximum normal strain criterion it seems that the model is safe under the applied load

$$[\ \varepsilon_1 = 0.008647\ ] < [\ \varepsilon_{uts} = 0.04539\ ]$$

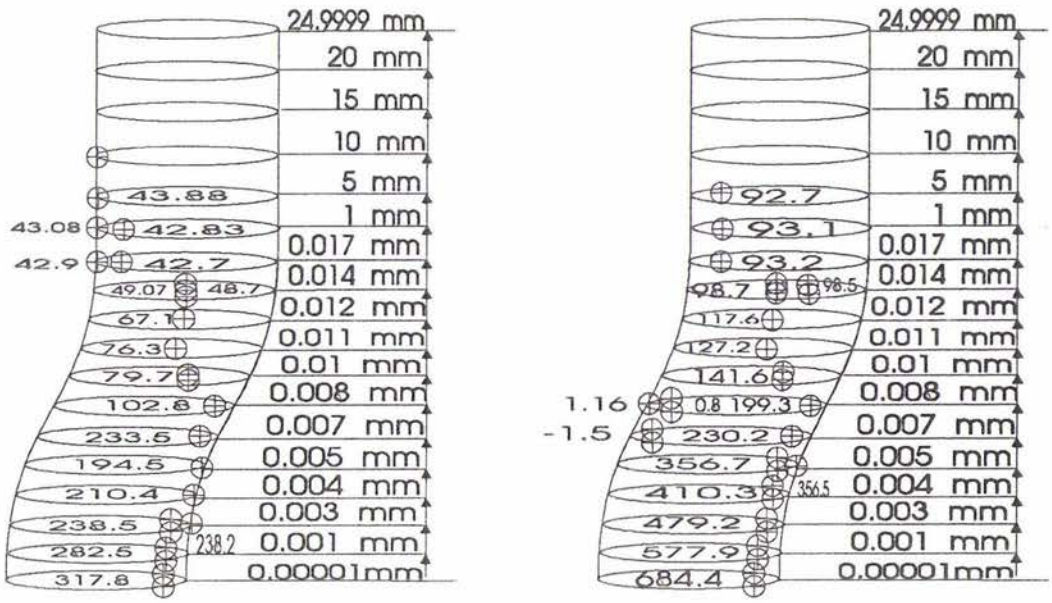

a) Maximum principal stress values. *b) Maximum shear stress values.*

Figure 4.60: Maximum values of σ_1 and τ_{max} on the studied cross sections.

As Figure 4.61 shows, the maximum value of [ε_1 =0.008647] occurs at the middle of the crimp area and right on the position of the maximum principal stress (see Figure 4.60(a)). The same failure as for the former criterion is predicted but as discussed before, under this criterion failure may occur at a lower load level than the former.

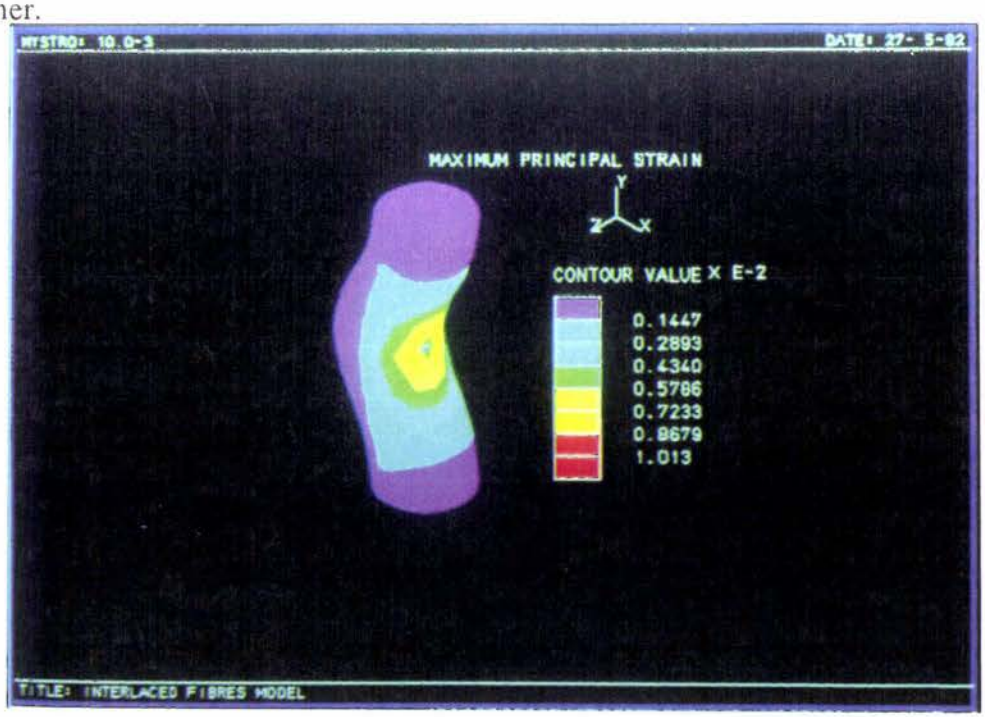

Figure 4.61: 3-D contour of ε_1 (maximum principal strain) in the crimp area.

As Figure 4.60(b) shows, the maximum values of τ_{max} also occur on the positions of σ_1 which are placed right on the outer surface of the fibre. This result confirms that the crimped fibre will fail from the middle of the crimp. The predicted path of failure for the crimped fibre is shown in Figure 4.62.

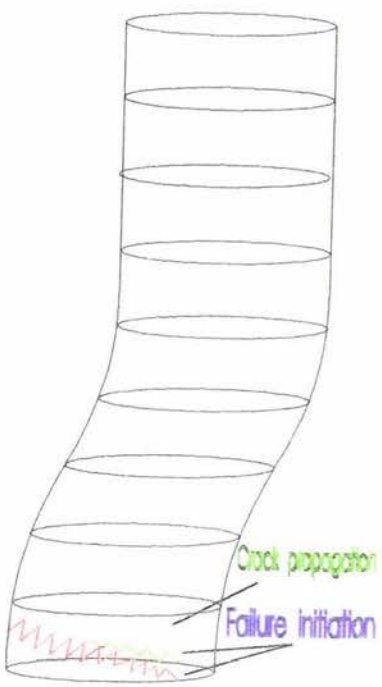

Figure 4.62: Predicted path of failure for the interlaced fibres model.

4.5. Single Crimped Fibre-Matrix Model

4.5.1. Thick Cylindrical Matrix or (Big Matrix Volume Fraction)

4.5.1.1. Stress Analysis

In order to study the effects of a matrix on the stress distribution of the fibre of the single crimped fibre model a cylindrical matrix around it was considered.

The stress situation for this model is different to that of SCFM. It is noted that the load which was applied to the single crimped fibre model is equal to the load which the fibre carries by itself in the composite situation (see section 3.4 for more details). Relative to SCFM, similar regions of stress appear on the cross sections of the model especially on the fibre area, but there are two exceptions. Firstly, a big difference is seen between the values and secondly the maximum values of the stress components, instead of appearing on the outer surface of the fibre, are shifted onto the fibre cross section area. The discussion here is limited to the fibre cross sections and the matrix stress situation will be discussed in section 4.6.

4.5.1.1.1. Normal Stress in the y-Direction

Comparing Figures 4.63 (overleaf) and 4.21 shows that, ignoring the values, the stress regions on the fibre's area are fairly similar. As Figure 4.64 (overleaf) shows, the maximum value of σ_y in the straight part from the end section toward the beginning of the crimp decreases and then increases again in the crimped area as expected. Comparing these values to the values of SCFM shows that the matrix acts such that the stress values decrease in the whole of the fibre. It appears that the matrix works like an energy absorber. As a result, the magnitude of SCF decreases to 1.4 from 8.78 for the SCFM. It is noted that this result is based on the perfect interface assumption. This value increases under a real interface condition because the matrix cannot absorb the crimp effect efficiently. This phenomenon could be considered as a reason for the appearance of the fibre failure mode after the debonding mode has occurred, this will be discussed later.

The effect of the thickness of the matrix cylinder on altering the stress values could be a subject for further research. But in this study a single crimped fibre with different thickness for the matrix was considered. The dimensions of this model was the same as the crimped fibre of the interlaced fibres plus the matrix model. The results of this experiment are similar to those of the interlaced fibres plus matrix model which will be discussed later. The only result which is considered here is that the matrix thickness is very important for the stress redistribution. The results show that for this model the magnitude of SCF increases to 3.74 from 1.4 for the model with the thicker matrix. As was discussed in chapter one the internal stress concentration factor is dependent upon the fibre volume fraction (v_f) i.e. SCF increases when the matrix thickness or the fibre distance decreases. Comparing the distribution graphs of σ_y for the middle of the crimp and the end section (see Figure 4.65) with the graph of Figure 1.1 shows the deviation of σ_y from the theoretical results for a crimped fibre.

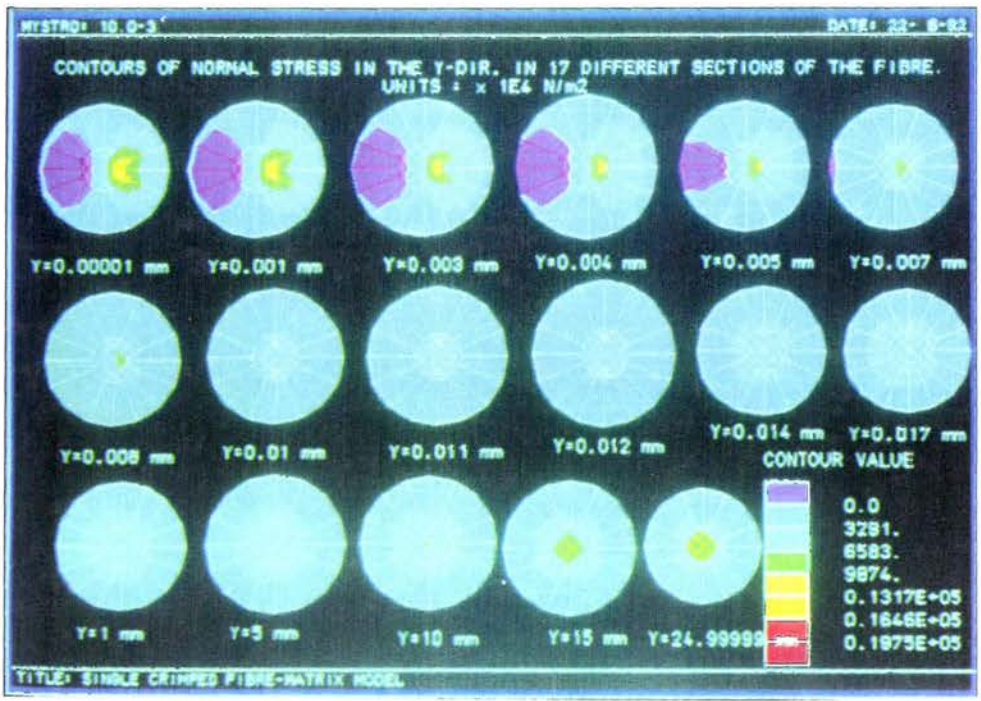

Figure 4.63: Colour contour of σ_y on the studied cross sections.

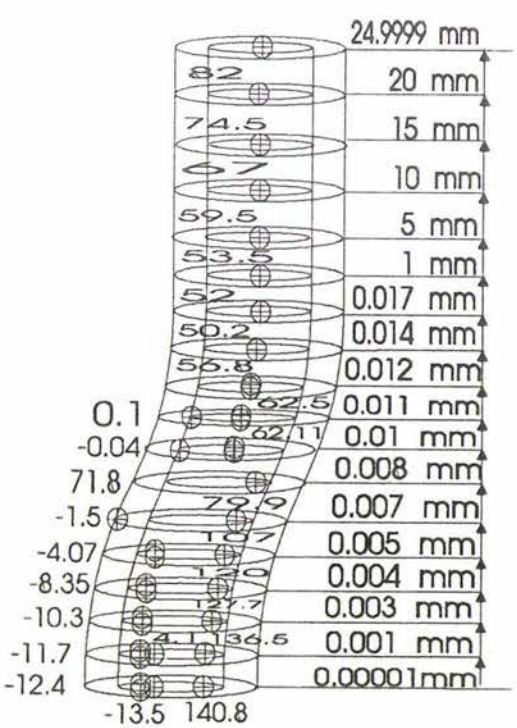

Figure 4.64: Maximum values of σ_y on the studied cross sections.

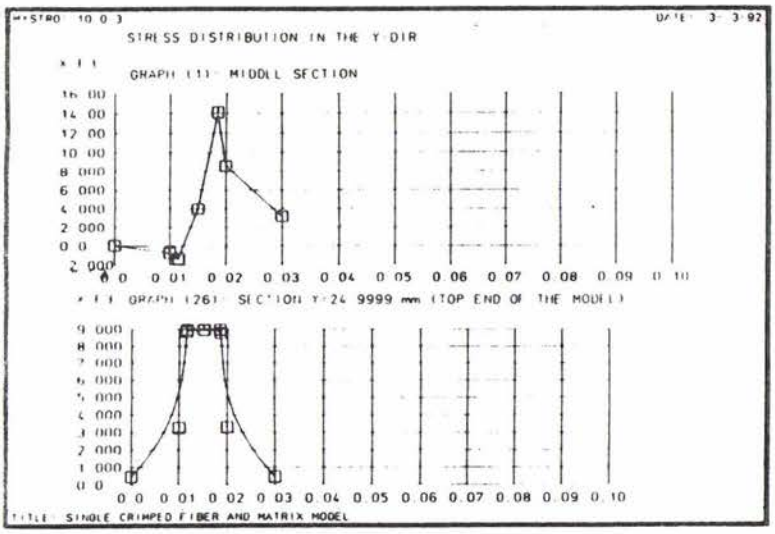

Figure 4.65: Distribution graphs of σ_y on the middle of the crimp and the end of the fibre.

4.5.1.1.2. Normal Stress in the x-Direction

Comparing Figures 4.66 and 4.26 shows that the stress situation (on the fibre area) in the x-direction is relatively similar to that of SCFM. A small difference is seen on section y=0.01 mm to y=0.014 mm. Comparing the distribution graphs of σ_x on these sections of the model with SCFM (see Figures 4.67(a) and (b) (overleaf)) show that the occurrances of the sign σ_x on the fibres area are not similar but the shape of the graphs are relatively identical and the values are close together. Hence, the mentioned changes are immaterial.

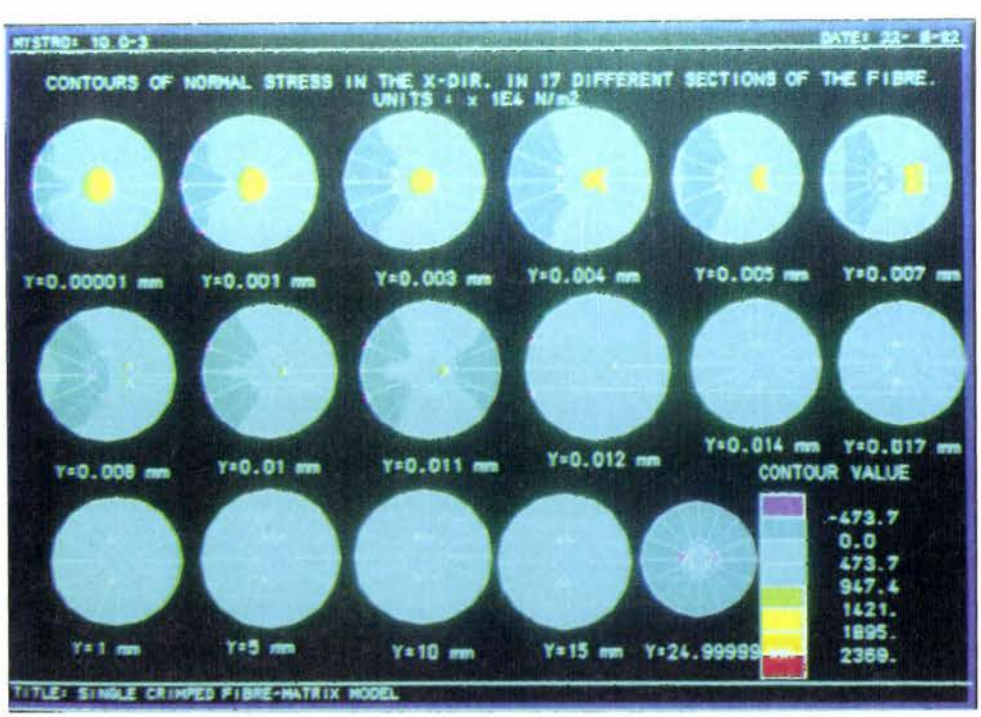

Figure 4.66: Colour contour of σ_x on the studied cross sections.

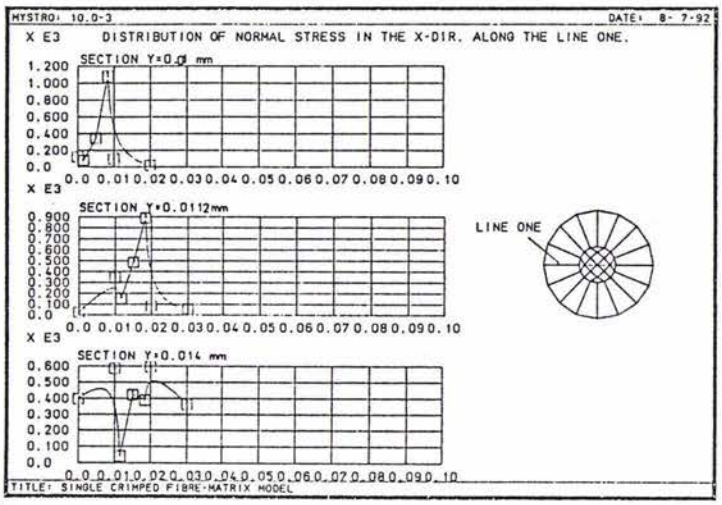

a) Single crimped fibre-matrix model (thick matrix)

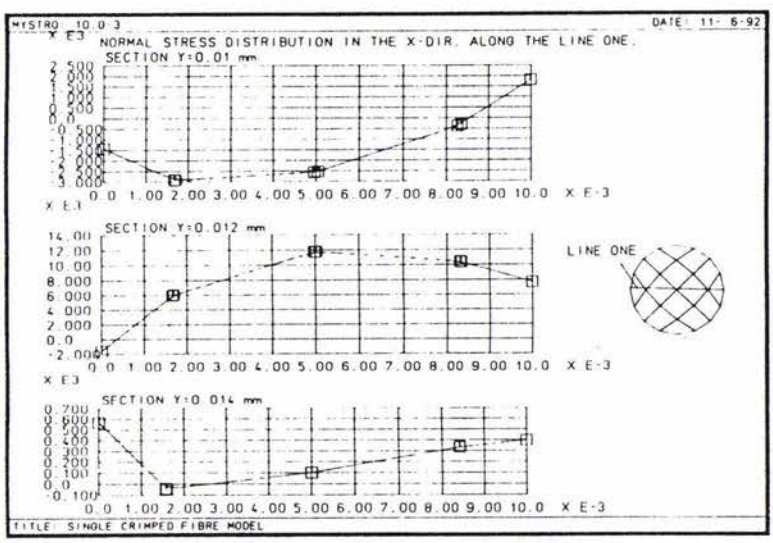

b) Single crimped fibre model.

Figure 4.67: Distribution of σ_x from section y=0.01 mm to y=0.014 mm

4.5.1.1.3. Normal Stress in the z-Direction

The situation of σ_z in the first curve of the crimp is similar to that in SCFM (see Figure 4.68(overleaf) and 4.29). However, it is different in the second curve until approaching the start of the straight part of the fibre.

Instead of a compressive region appearing as in Figure4.29, a tensile region of σ_z appears on the fibre's cross section. As was discussed earlier, despite changing the stress sign from section y=0.01mm to y=0.014 mm, the stress values are relatively close (see Figures 4.69 and 4.70 (overleaf)).

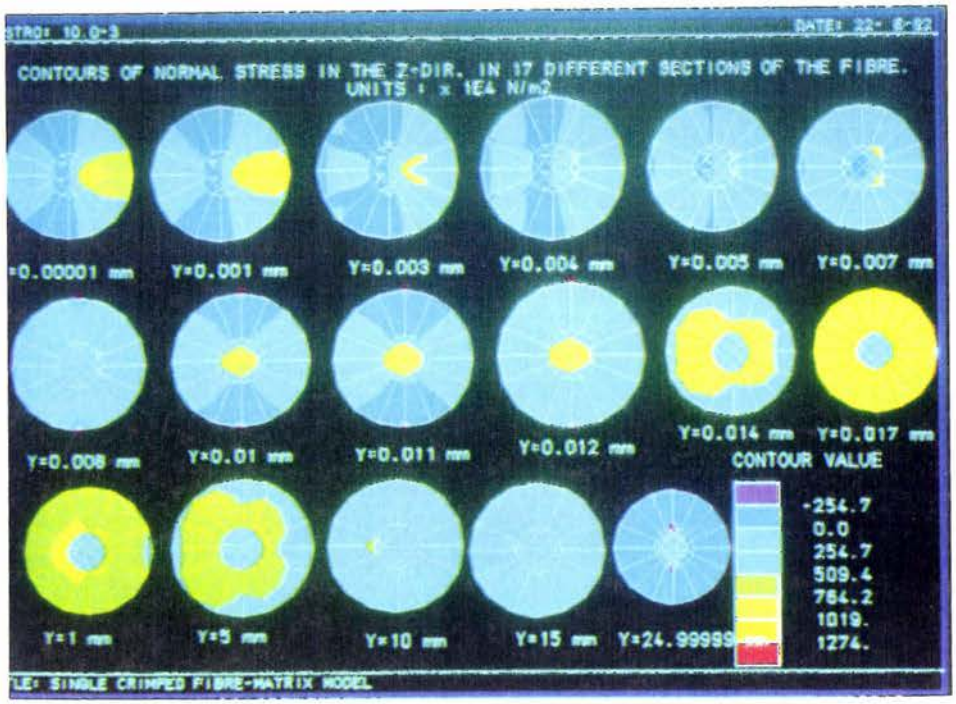

Figure 4.68: Colour contour of σ_z on the studied cross sections.

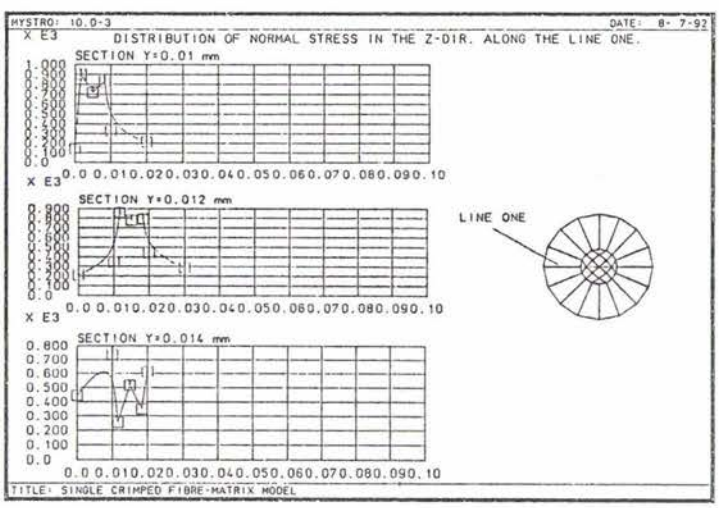

Figure 4.69: Distribution of σ_z for the single crimped fibre-matrix model.

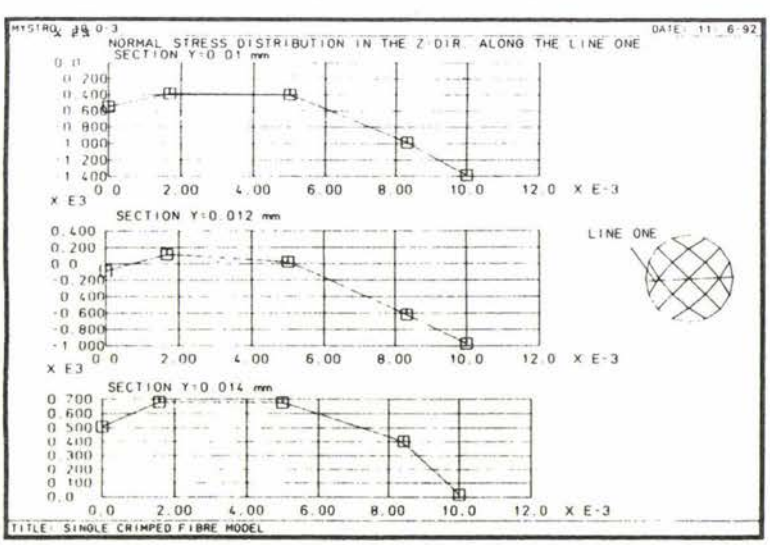

Figure 4.70: Distribution of σ_z for the single crimped fibre model.

From the discussion of the normal stress components the prediction of the direction of the reaction load in both the concave and convex parts is shown in Figure 4.71. By comparing Figures 4.71 and 4.31 it is concluded that the matrix, rather than introducing a big change in the stress values, changes the reaction load direction in a small region in the crimped area near the straight part. As will be seen, this change in the load direction, unlike the SCFM, cannot cause a significant deviation in the shear stress components.

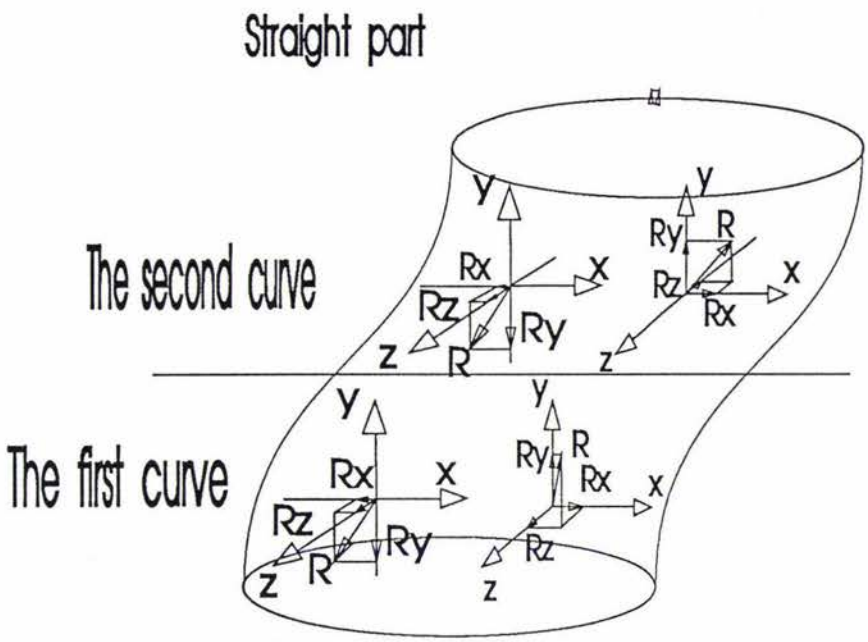

Figure 4.71: Prediction of the reaction load in the crimped area of the model.

4.5.1.1.4. Shear Stress on the xy-Plane

The same situation as in Figure 4.32 of the SCFM is seen in Figure 4.72 (overleaf) for τ_{xy}. From the middle section of the crimp to the end of the first curve, the x-component of the reaction load in both the concave and convex parts increases. Hence two maximum tensile and compressive regions of τ_{xy} appear in the vicinity of the interface in the concave and convex parts respectively.

4.5.1.1.5. Shear Stress on the xz-Plane

Ignoring the values, a good agreement for the sign of τ_{yz} is seen on both the fibre and matrix areas with the SCFM (see Figure 4.73 (overleaf) and 4.34).

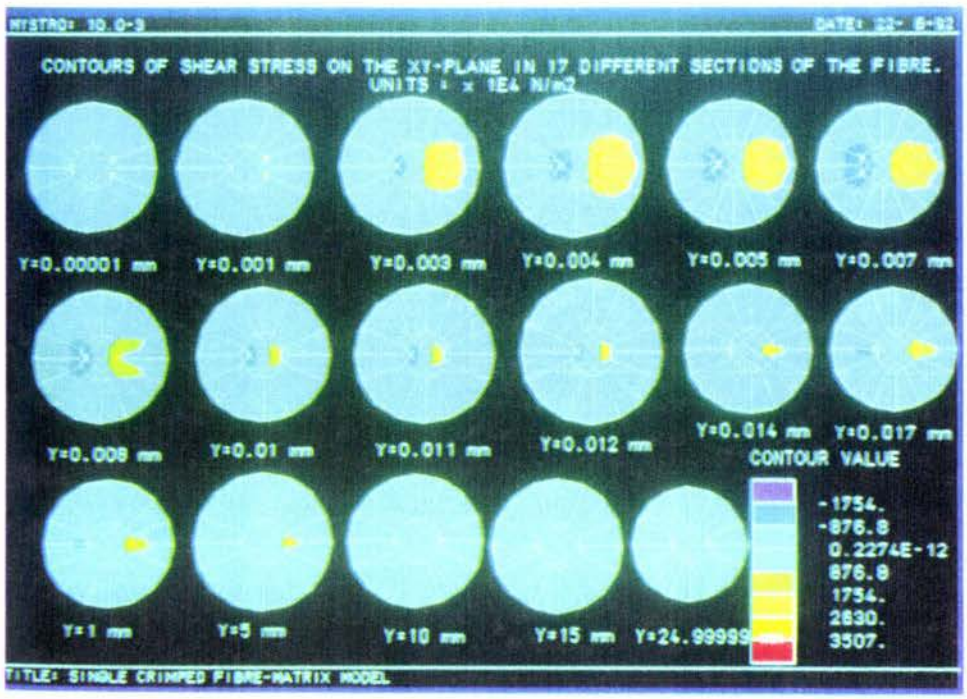

Figure 4.72: Colour contour of τ_{xy} on the studied cross sections.

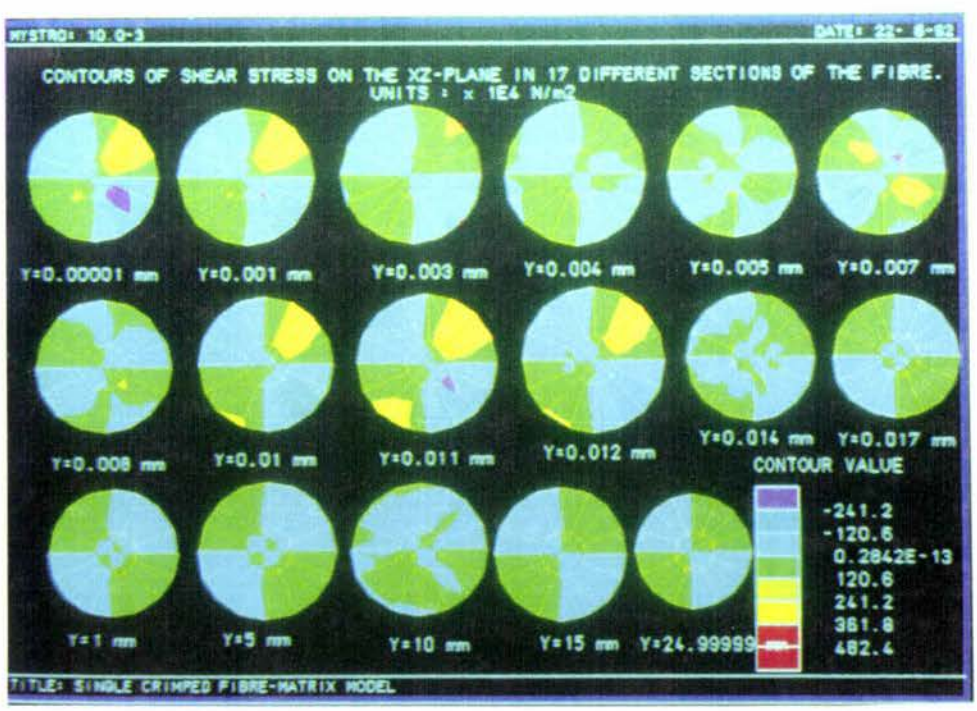

Figure 4.73: Colour contour of τ_{xz} on the studied cross sections.

4.5.1.1.6. Shear Stress on the yz-Plane

A relatively similar situation as in Figure 4.37 happens on the whole area of the studied cross sections of the model but a different situation is seen on the fibre's area (see Figure 4.74.

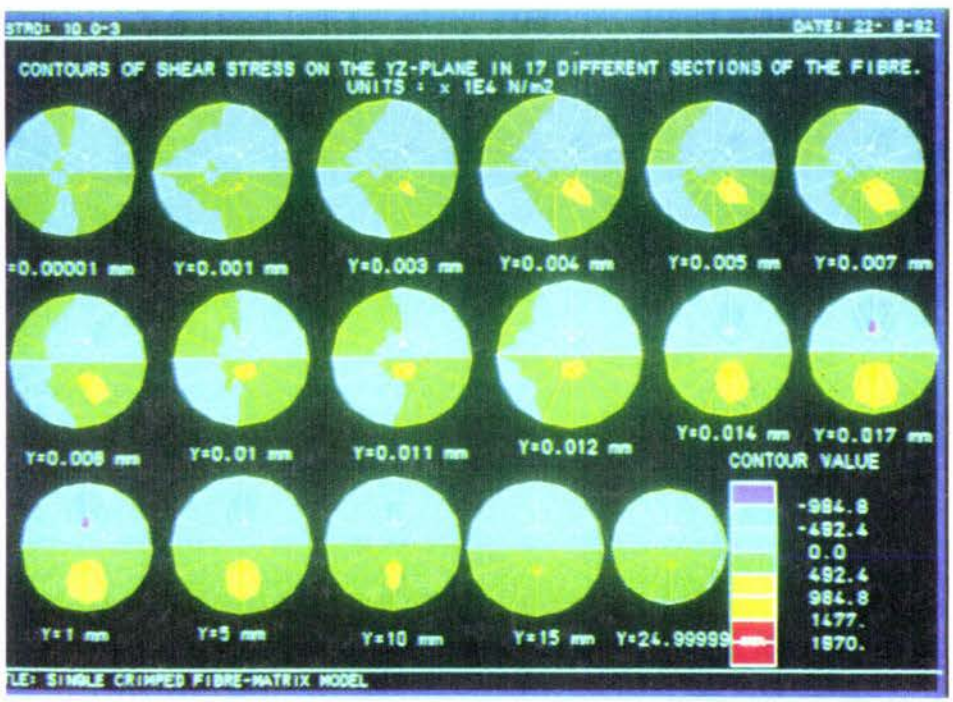

Figure 4.74: colour contour of τ_{yz} on the studied cross sections.

From the discussion of the shear stress components on the different planes it is concluded the small changes in the values and direction of the reaction load can govern the following situations:

A) For τ_{xy} : Due to the small changes of the x-component of the reaction load, it is the y-component which governs the situation of τ_{xy}, so there is little difference between the fibre's area.

B) For τ_{xz} : As both the x and z-components of the reaction load suffer some changes, the introduced changes by the x-component to the situation of τ_{xz} are compensated by the z-component and vice-versa.

C) For τ_{yz} : As the y-component of the reaction load remains unchanged, relative to the SCFM, the z-component by generating torsion in both the concave and convex parts of the crimp governs the situation of τ_{yz}.

4.5.1.2. Failure Analysis

The same failure criteria as for the straight fibre-matrix model are examined in this section.

4.5.1.2.1. Maximum Normal Stress Criterion

According to this criterion the fibre is safe under the applied load because the maximum value of σ_1 , which happens at the middle of the crimp (see Figure 4.75(a)), is placed in the safe region of Figure 4.8(a) i.e.

$$\sigma_1 = 140.8 \text{ MN/m}^2 < \sigma_{uts} = 3450 \text{ MN/m}^2$$

Ignoring the matrix and interface failure modes, with the increasing of the applied load a crack may initiate at the position of the maximum of σ_1 and propagates as in Figure 4.75(b) along the two possible paths.

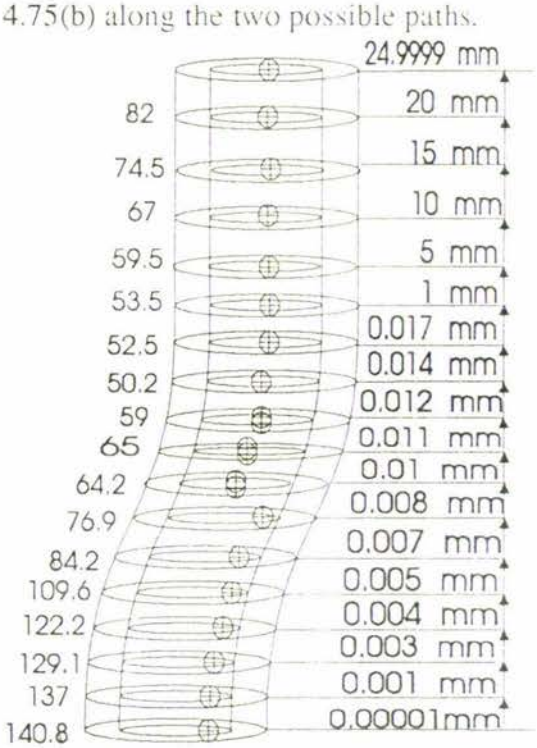

a) Maximum value of σ_1.

b) Predicted paths of failure.

Figure 4.75

Different paths of failure are predicted by applying the same criterion to the matrix. As the graphs of Figure 4.76 show, the maximum value of σ_1 in the matrix area occurs at the middle of the crimp right on the interface of the fibre and matrix. According to the criterion, the matrix under the applied load is in a critical situation because the maximum value of σ_1=80 MN/m^2 lies on the boundary of the criterion (see Figure 4.8(b))

$$\sigma_{uts} = 40 \text{ MN/m}^2 < \sigma_1 = 80 \text{ MN/m}^2 < \sigma_{uts} = 90 \text{ MN/m}^2$$

(Lower bound) (Upper bound)

Regarding the critical situation of the matrix, failure will initiate at the matrix area before the fibre failure mode appears. Rather than the matrix failure, interface failure (debonding) is also possible. Comparing the values of σ_1 in Figure 4.76 on the interface area shows that instead of transverse propagation of the initiated crack to the matrix area it may propagate along the interface and cause a debonding in the concave part. The possible paths of failure are shown in Figure 4.77.

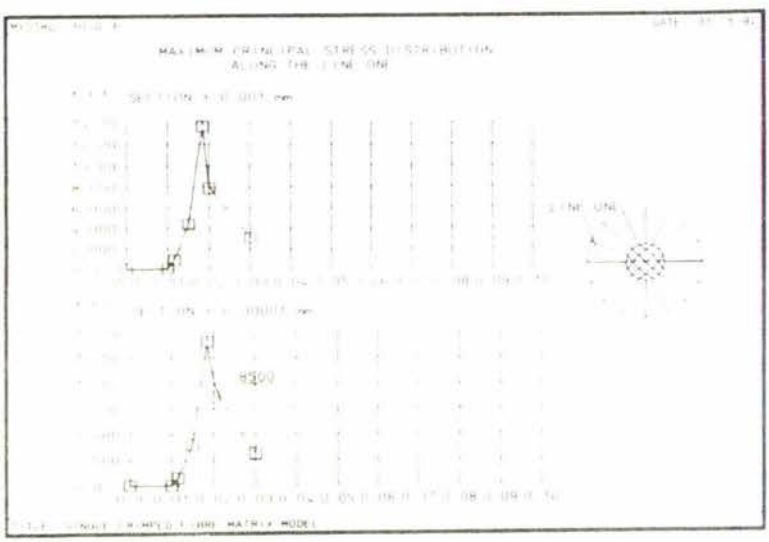

Figure 4.76: Distribution of σ_1 on sections y=0.00001 mm and y=0.001 mm.

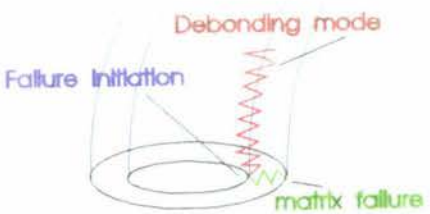

Figure 4.77: Predicted paths of failure.

4.5.1.2.2. Maximum Normal Strain Criterion

Different failure results are gained based on this criterion. As Figure 4.78 shows the maximum strain for the composite occurs at the middle of the crimp and on the outer

surface of the matrix cylinder. The maximum value of ε_1 for the fibre occurs in section y=0.007 mm and on the interface (see Figure 4.79 (overleaf)). According to this theory the fibre is safe under the applied load

$$\varepsilon_1 = 0.002799 < \varepsilon_{uts} = 0.0454$$

Ignoring the matrix and interface situations, with the increasing of the applied load a crack(s) will initiate at section y=0.007 mm and then may propagate in two directions transverse to the fibre or along its length (see Figure 4.80(a)). It is possible that the debonding mode occurs before the fibre failure mode because the maximum value of ε_1 for the fibre area occurs on the interface.

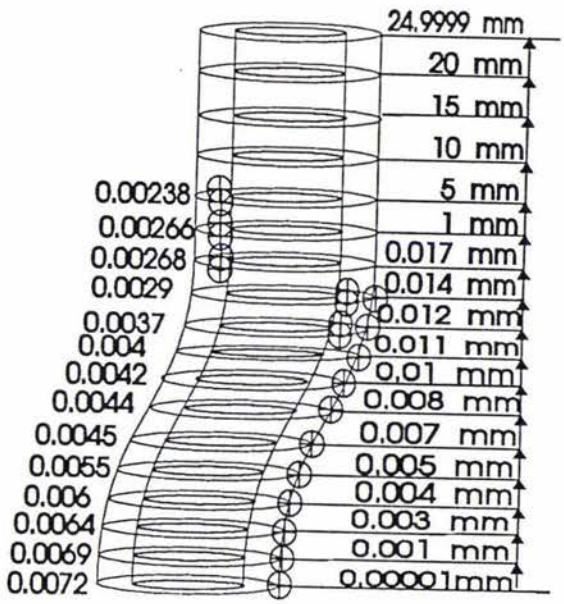

Figure 4.78: maximum values of ε_1 on the studied cross sections.

Based on the theory and according to Figure 4.78, the matrix is safe under the applied load

$$\varepsilon_1 = 0.00702 < \varepsilon_{uts} = 0.01 \text{ to } 0.0225$$

With the increasing of the applied load it is clear that a crack will initiate in the position of the maximum of ε_1 and then transversely propagate to the matrix area. It is noted that under a real interface situation the occurrance of the debonding mode before the matrix failure mode is also possible. See Figure 4.80(b) for the failure prediction paths.

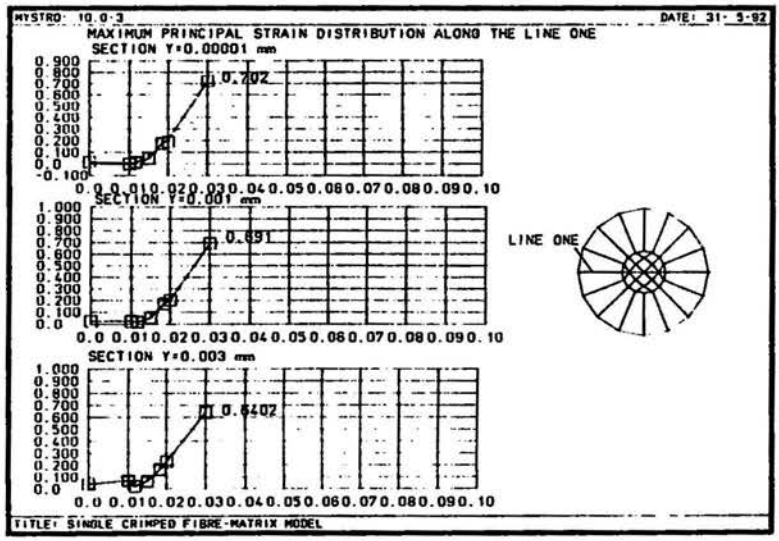

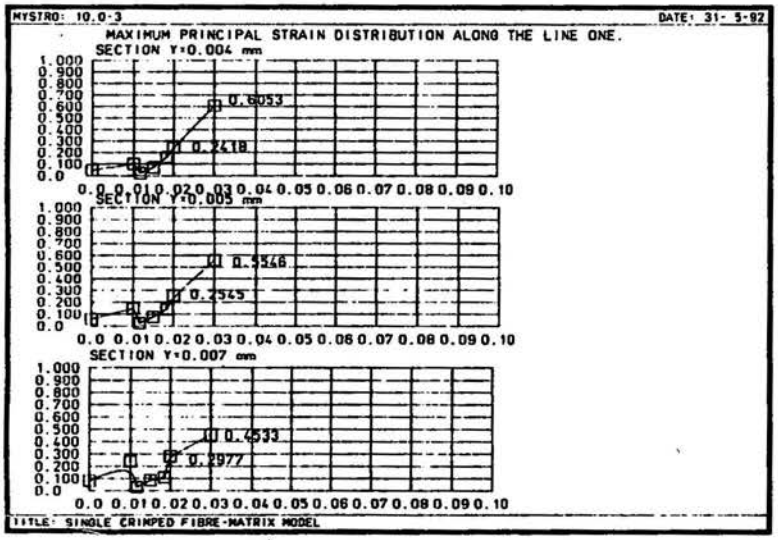

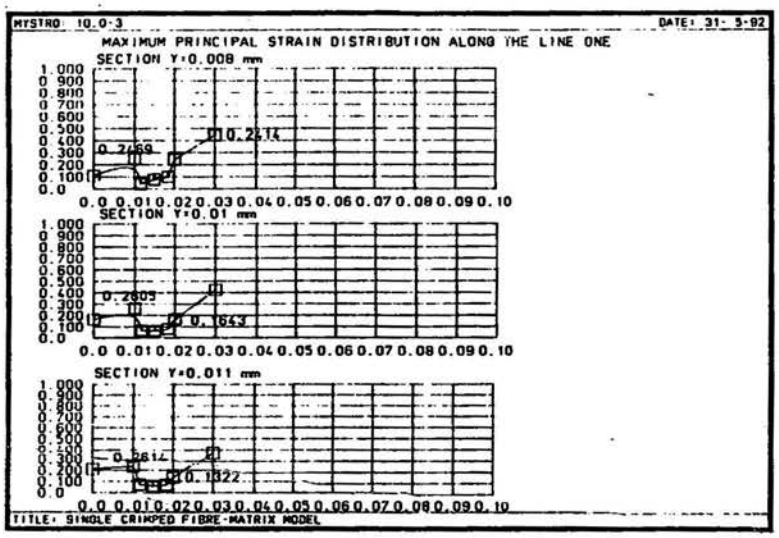

Figure 4.79: Distribution graphs of ε_1.

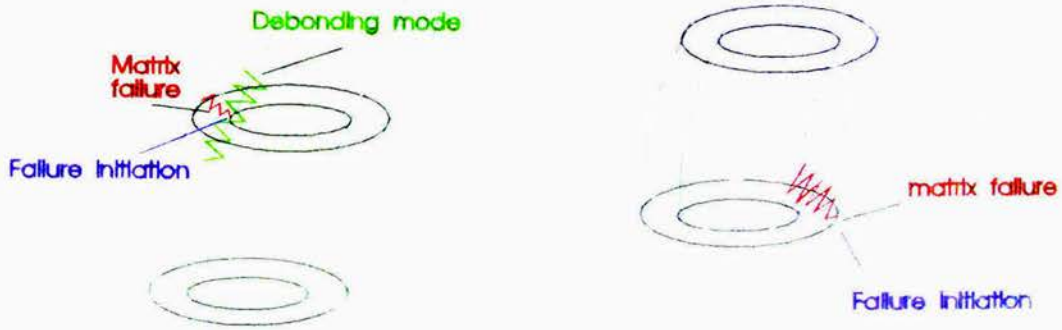

a) Fibre consideration *b) Matrix consideration*

Figure 4.80: Failure prediction paths

4.5.1.2.3. Maximum shear Stress Criterion

The maximum values of τ_{max} on the studied cross sections are shown in Figure 4.81(a). The distribution graph of τ_{max} on the middle of the crimp shows that the maximum value of this quantity in the matrix area occurs on the interface (see Figure 4.81(b)). According to this theory the matrix is in a critical situation because

$$0.5\ \tau_{uts} = 20\ MN/m^2 < \tau_{max} = 40\ MN/m^2 < 0.5\ \tau_{uts} = 45\ MN/m^2$$

(Lower bound) (Upper bound)

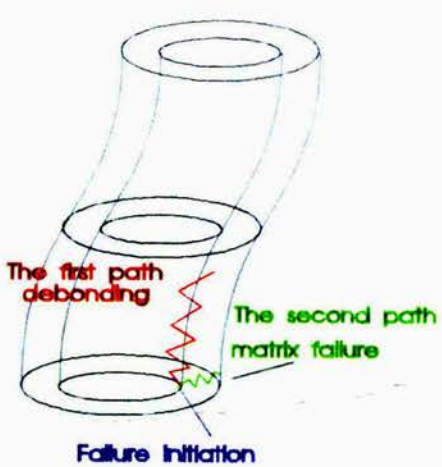

Figure 4.82: Predicted path of failure.

Both the matrix failure and debonding failure modes may occur, but considering a real interface condition debonding mode may find more chance to occur first.

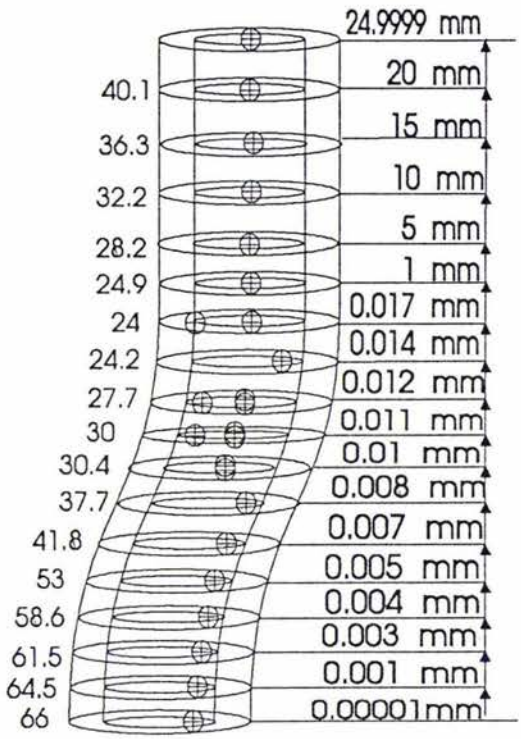

a) Maximum values of τ_{max}.

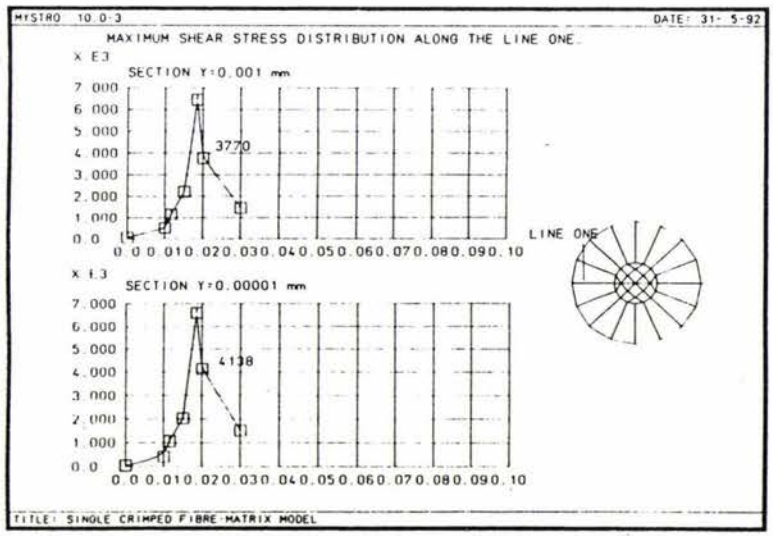

b) Distribution graph of τ_{max}.

Figure 4.81

4.5.1.2.4. Maximum Distortional Energy Theory

The maximum values of σ_v on the studied cross sections and its distribution graph on the middle of the crimp, where the maximum happens, are shown in Figures 4.83(a) and (b) respectively. Based on this criterion, similar to the last section, the matrix is in a critical situation because

$$\sigma_{uts} = 40 \text{ MN/m}^2 < \sigma_v = 80 \text{ MN/m}^2 < \sigma_{uts} = 90 \text{ MN/m}^2$$
(Lower bound) (Upper bound)

This criterion predicts that, under a real interface condition, the debonding mode may occur first and will be followed by the matrix failure. The same paths of failure as in Figure 4.82 may happen.

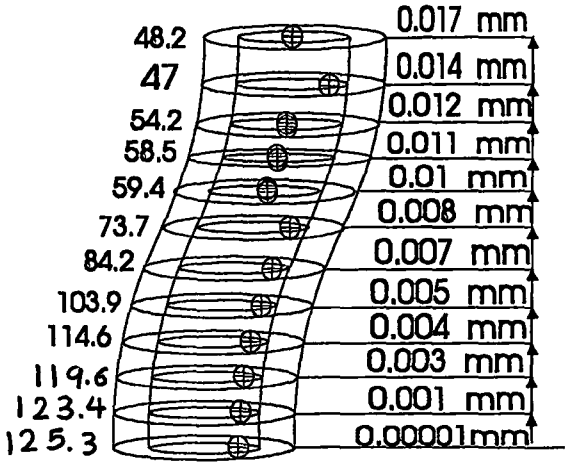

a) Maximum values of σ_v.

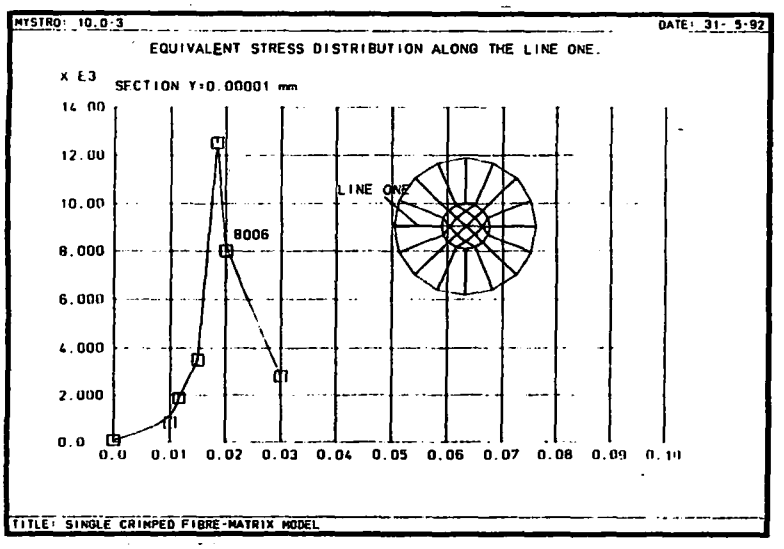

b) Distribution graph of σ_v.

Figure 4.83

4.5.2. Thin Cylindrical Matrix or (Small Matrix Volume Fraction)

As discussed in section 4.5, to study the effects of the matrix volume fraction a new model similar to the crimped fibre of the interlaced fibres plus matrix model was designed. It is most helpful to study the results of this model before looking at the interlaced fibres plus matrix model.

4.5.2.1. Stress Analysis

Figures 4.84 to 4.86 show the normal stress components in the x, y, and z-directions on the studied cross sections respectively. Ignoring the difference between the values, an excellent similarity is seen for σ_x and σ_y on the fibres area with the results of the last model in Figures 4.66 and 4.63. A small difference occurs in the second curve of the crimp for σ_z, but the stress situation for the rest of the cross sections is similar to Figure4.68. The difference between the stress values is high such that it can change the order of appearance of the failure modes. In addition to normal stress components, shear stress on different planes on the studied cross sections are fairly similar to the results of the SCFM (compare Figure 4.87 to 4.89 with Figures 4.72, 4.74, and 4.73 respectively).

Comparing the results of this model with the single crimped fibre without a matrix gives a better understanding of the matrix volume fraction effects. An excellent similarity is seen between the normal and shear stress components of this model with the single crimped fibre model of section 4.3 (compare Figures 4.84 to 4.89 with Figures 4.26, 4.21, 4.29, 4.32, 4.37, and 4.34 respectively). This confirms the prediction of the reaction load situation in both the concave and convex parts of the crimp in section 4.3 (see Figure 4.31).

The effect of the matrix volume fraction on the S.C.F. was discussed in section 4.5.1.1.1 and its effect on the failure modes is the subject of the next subsection.

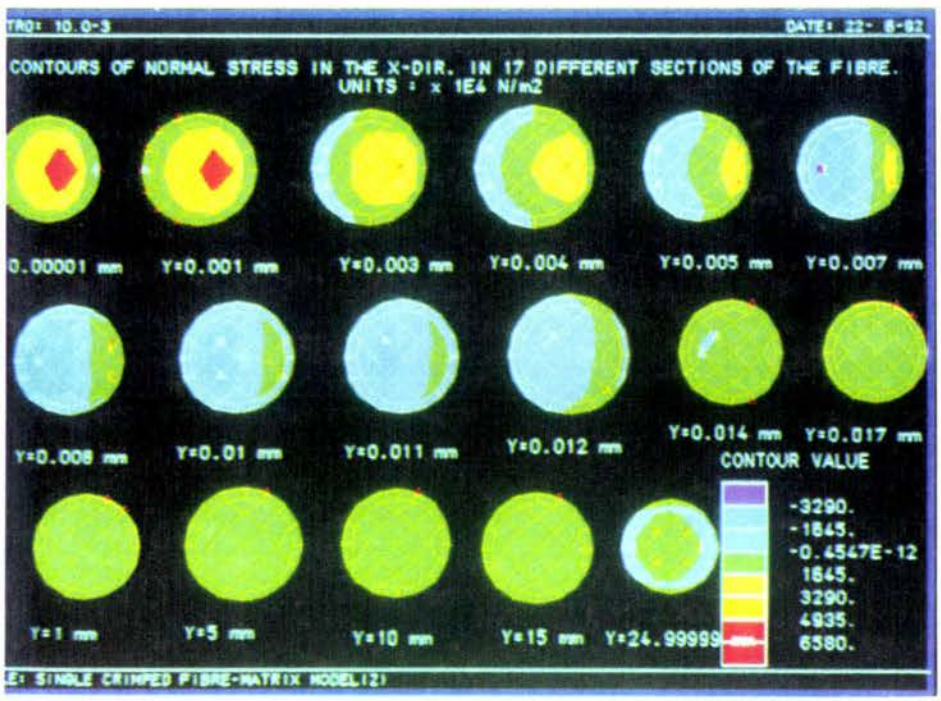

Figure 4.84: Colour contour of σ_x on the studied cross sections.

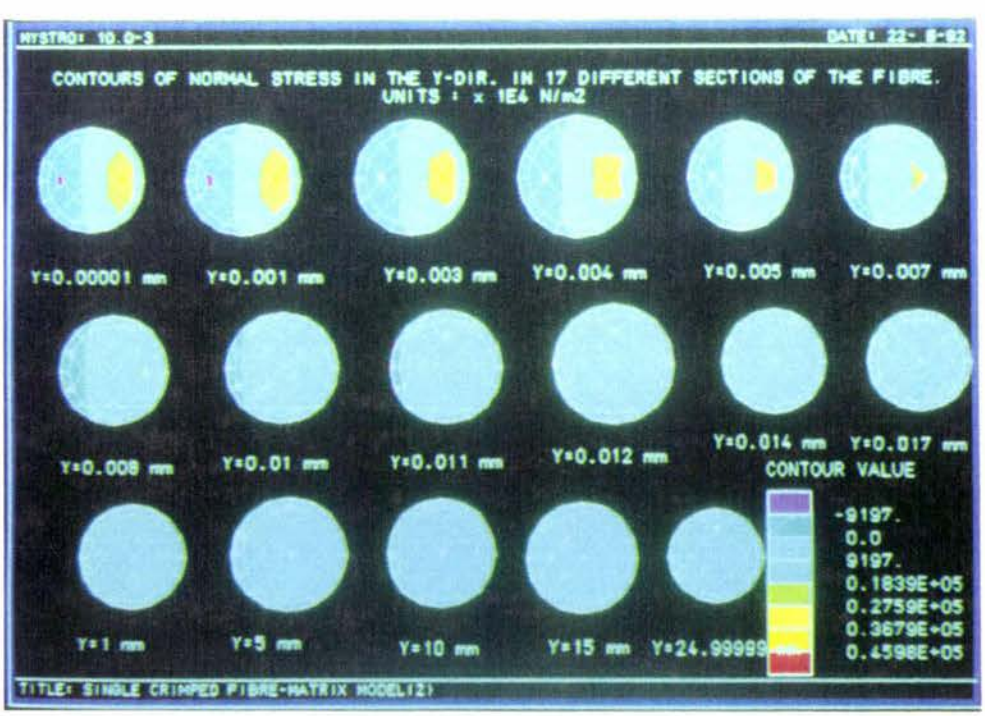

Figure 4.85: Colour contour of σ_y on the studied cross sections.

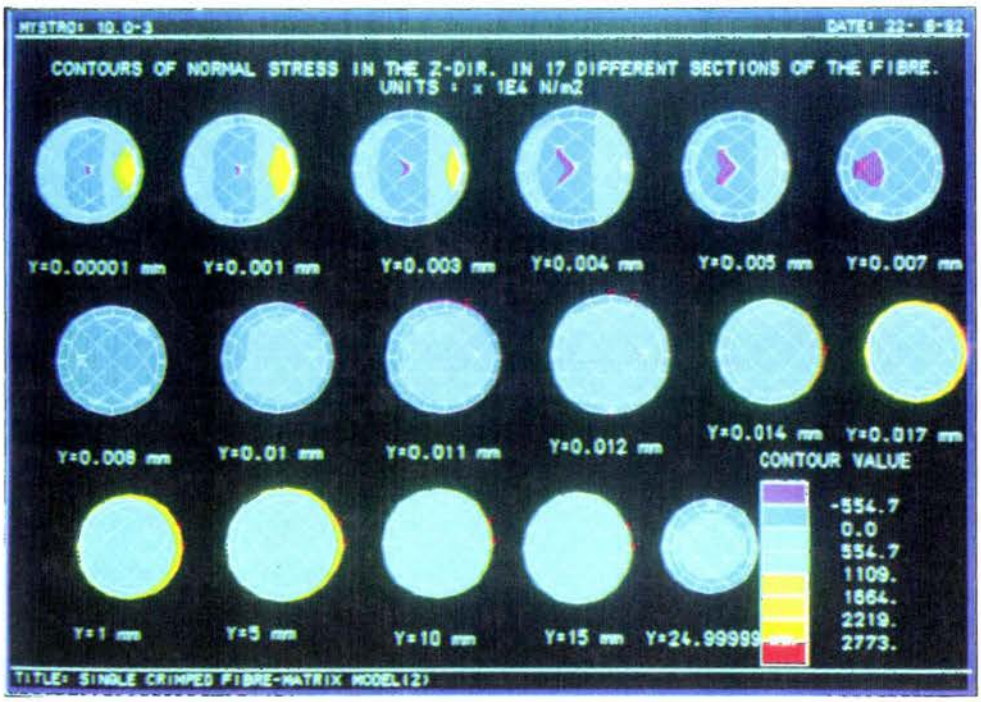

Figure 4.86: Colour contour of σ_z on the studied cross sections

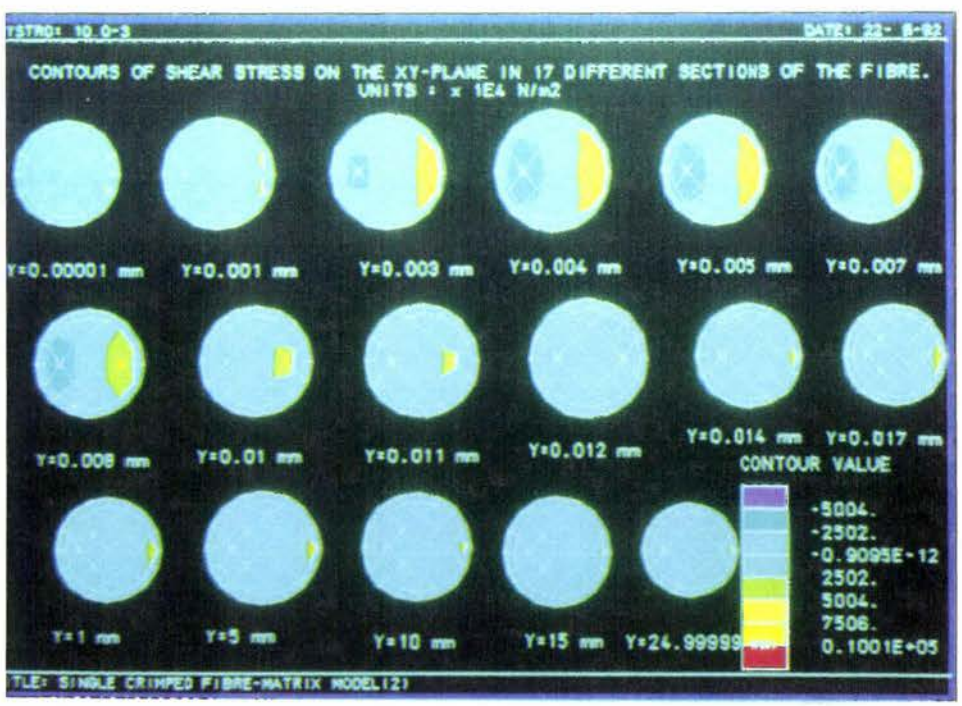

Figure 4.87: Colour contour of τ_{xy} on the studied cross sections.

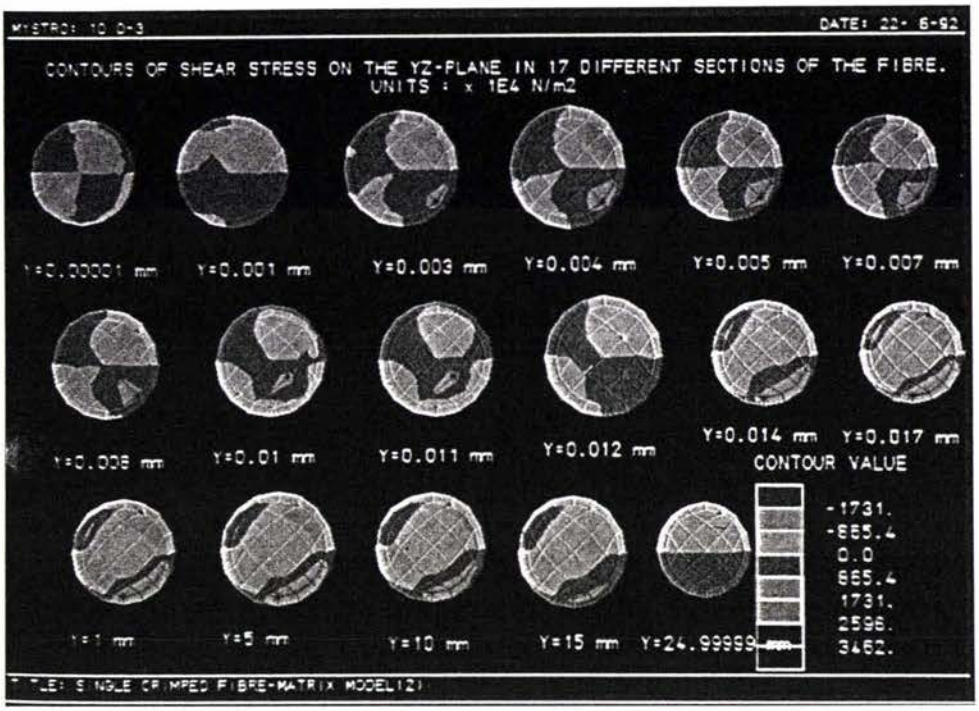

Figure 4.88: Colour contour of τ_{yz} on the studied cross sections.

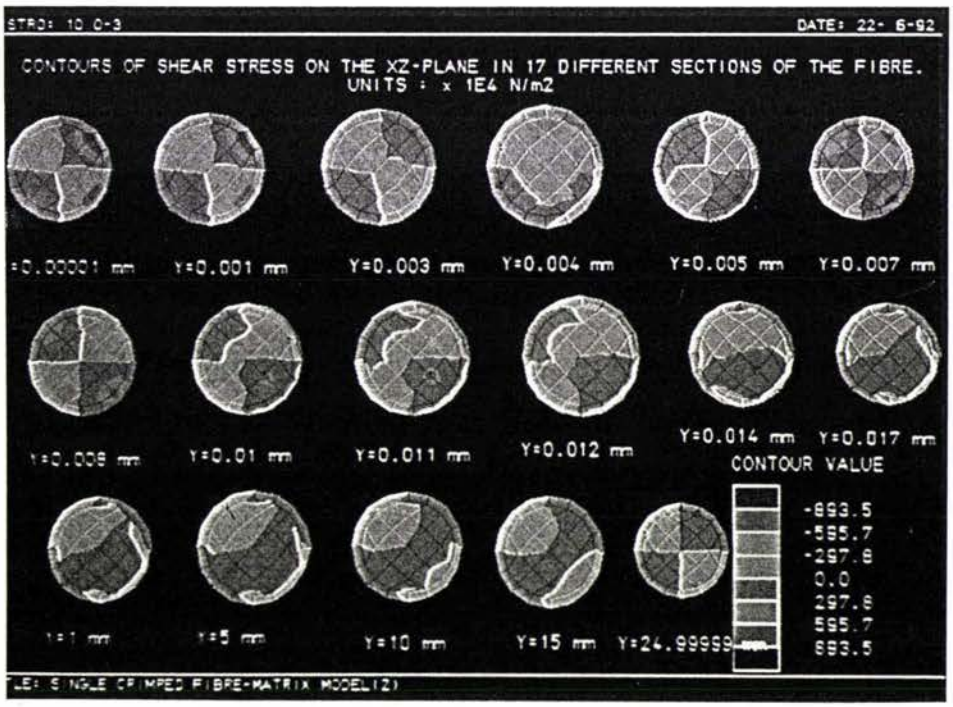

Figure 4.89: Colour contour of τ_{xz} on the studied cross sections.

4.5.2.2. Failure Analysis

4.5.2.2.1. Maximum Normal Stress Criterion

As Figure 4.90(a) shows, the same as the last model, the maximum value of σ_1 occurs on the middle of the crimp. Comparing the values of σ_1 to the last model indicates that the model with the thinner matrix, based on this criterion, fails in a lower level of the applied load

$$\sigma_1 = 335.8 \text{ MN/m}^2 < \sigma_{uts} = 3450 \text{ Mn/m}^2$$

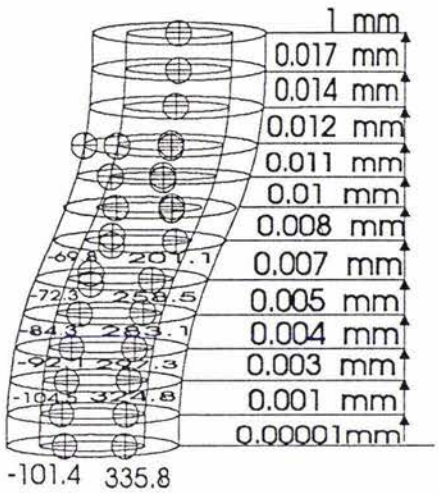

a) Maximum value of σ_1.

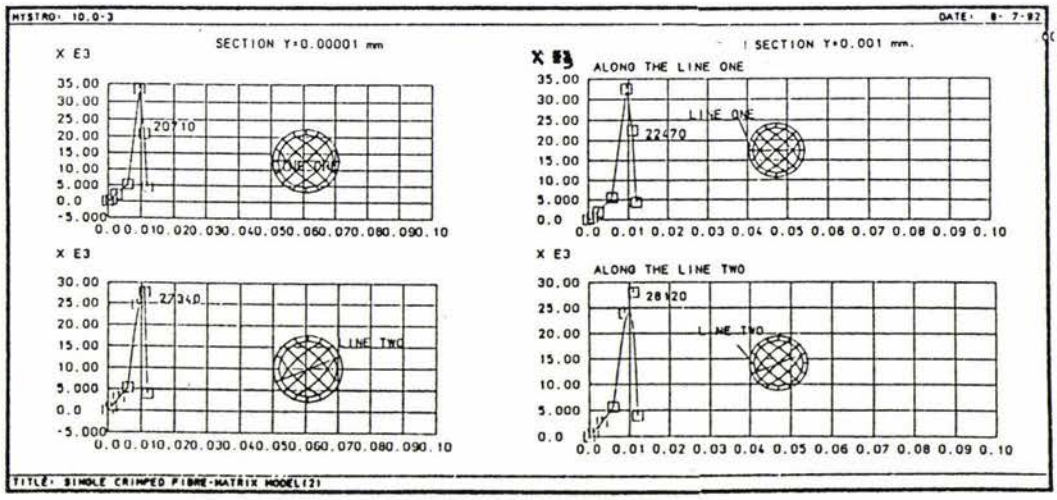

b) Distribution graphs of σ_1.

Figure 4.90

Applying the criterion to the matrix yields a different result. As Figure 4.90(b) shows the maximum value of (σ_1 =281.2 MN/m^2) in the matrix area happens on section y=0.001 mm along the line two on the interface. This value lies out of the safety region of the criterion for the matrix

$$\sigma_{uts} = 40 \text{ to } 90 \text{ MN/m}^2 < \sigma_1 = 281.2 \text{ MN/m}^2$$

This result predicts a much lower failure load for the model. The failure is initiated in the interface region and propagates as a debonding mode along the length of the fibre and after that will run across the matrix.

4.5.2.2.2. Maximum Normal Strain Criterion

The maximum value of ε_1 occurs on the middle of the crimp on the outer surface of the matrix cylinder while the maximum value in the fibre area occurs on section y=0.001 mm in the interface region (see Figures 4.91(a) and (b) (overleaf)). Comparing Figures 4.91(b) and 4.79 indicates that the gradient of strain in a thick matrix region is less than that in a thin region. This theory predicts a lower level load for failure of the fibre relative to the crimped fibre with thicker matrix model. Based on this criterion the fibre is safe

$$\varepsilon_1 = 0.007708 < \varepsilon_{uts} = 0.0454$$

but with increasing of the load, as the maximum value of ε_1 occurs on the interface region and the strength of the interface is lower than the fibre, initiation of the failure by the debonding mode is more possible than by the fibre failure mode.

Applying the criterion to the matrix yields a different result relative to the above failure prediction. Based on this theory the matrix is in a critical situation because

$$\underset{\text{(Lower bound)}}{\varepsilon_{uts} = 0.01} < \varepsilon_1 = 0.0102 < \underset{\text{(Upper bound)}}{\varepsilon_{uts} = 0.0225}$$

Based on the interface strength, one of the matrix or debonding modes of failure may occur first. If it is assumed that the interface is as strong as the matrix, matrix failure mode occurs first but in a real situation it is more possible that the failure starts with the debonding mode.

4.5.2.2.3. Maximum Shear Stress Criterion

Figure 4.92(a) (imminently shown) shows the maximum shear stress distribution along two different lines on the middle section of the crimp, sections y=0.001 mm, and y=0.002 mm. The comparison of the graphs shows that, while the maximum shear stress occurs at the middle of the crimp on the fibre area (see Figure 4.92(b)) the maximum of this quantity for the matrix area occurs at section y=0.001 mm (see

chapter 5 for the reason). According to this theory and regarding the values of Figure 4.92(a), the model has already failed because

$$0.5\,\tau_{uts} = 20 \text{ to } 45 \text{ MN/m}^2 < \tau_{max} = 139.4 \text{ MN/m}^2$$

This criterion gives the same result as for the maximum normal stress theory.

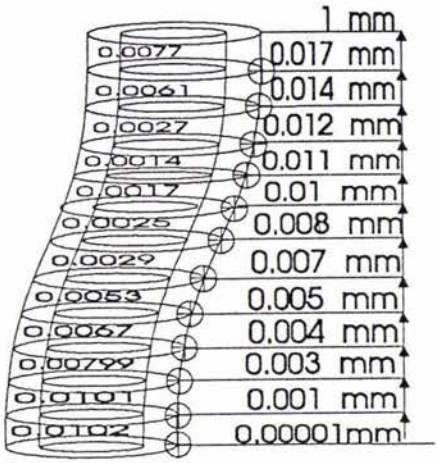

a) Maximum values of ε_1.

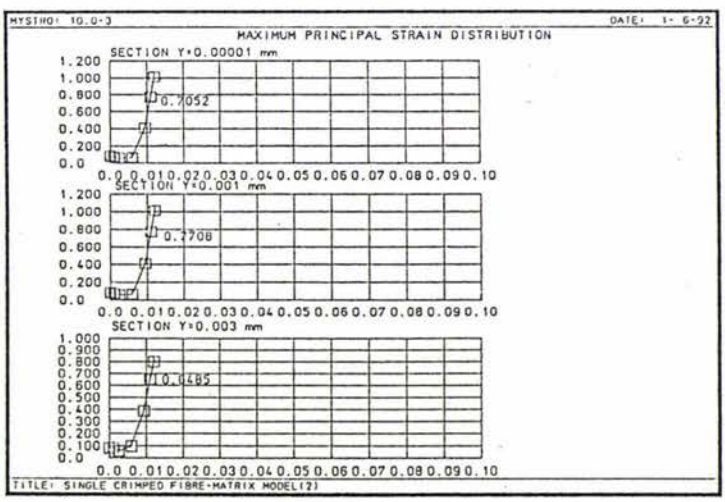

b) Distribution graphs of ε_1.

Figure 4.91

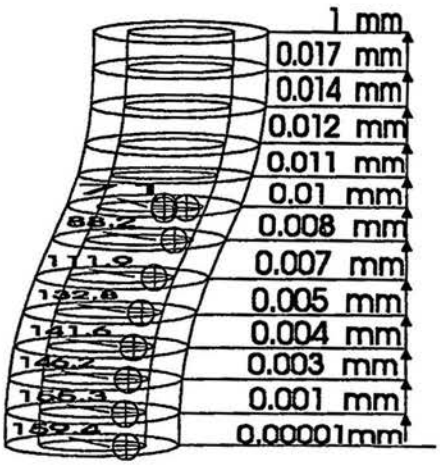

a) Maximum values of τ_{max}

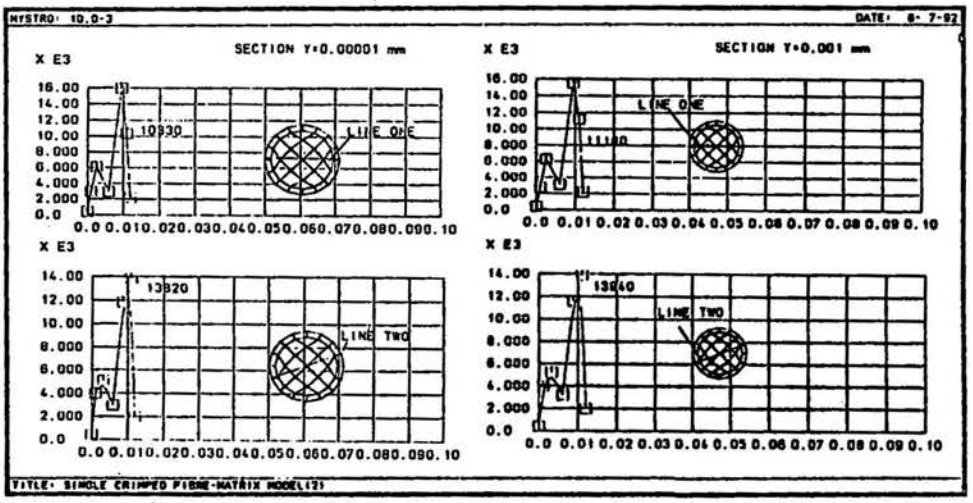

b) Distribution graphs of τ_{max}

Figure 4.92

4.5.2.2.4. Maximum Distortional Energy Theory

The position of the maximum value of σ_v on the fibre and matrix areas are the same as the maximum shear stress of the last section (see Figure 4.93(a) and (b) (overleaf)). The results show that, based on this theory the composite has already failed because

$$\sigma_{uts} = 40 \text{ to } 90 \text{ MN/m}^2 < \sigma_v = 286 \text{ MN/m}^2$$

This theory also predicts a lower load for failure.

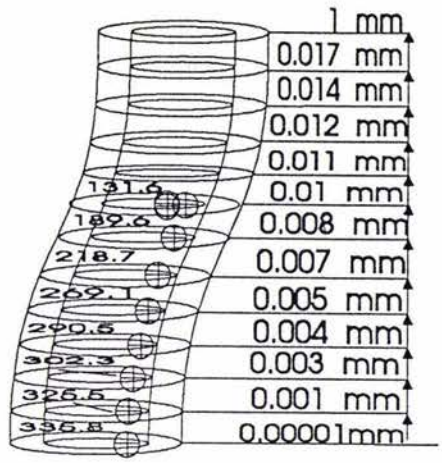

a) Maximum values of σ_y.

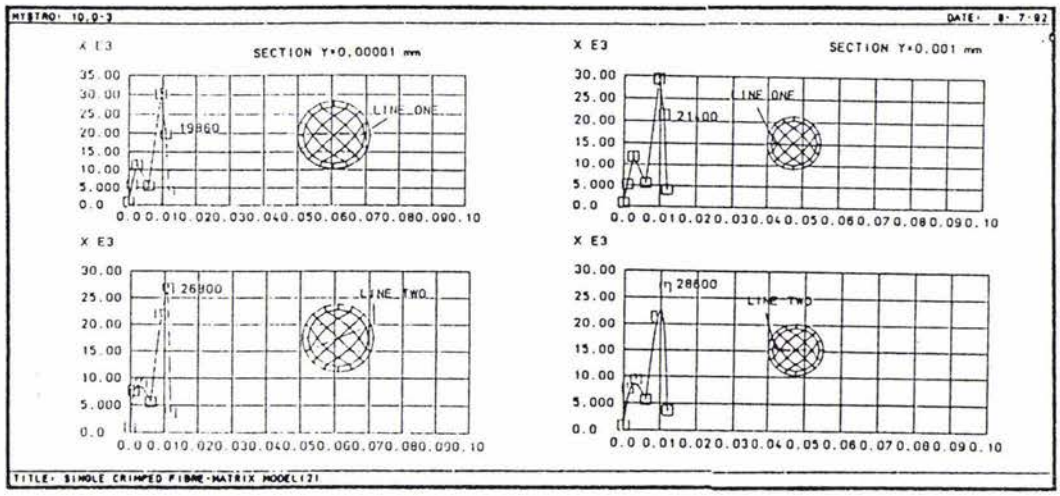

b) Distribution graphs of σ_y.

Figure 4.93

4.5.2.2.5. Conclusion

From the discussion of this model and of the model of section 4.5, the following are concluded:

I) The matrix volume fraction has a significant effect on the S.C.F..

II) The stress situation on the fibre area is in good agreement with the result of the single crimped fibre without a matrix. This result confirms the load prediction of section 4.3.1.1.

III) With the new matrix volume fraction, both the debonding and matrix failure modes occur about the middle of the crimp.

IV) The results of the failure criteria show that the model is in a critical situation and based on some of them the composite has already failed. Hence, increasing the applied load is not allowed. This means that the failure will never initiate by the fibre failure mode, unless the fibre suffers some manufacturing problems.

V) Based on the last two criteria, it is predicted that the debonding mode occurs before the matrix failure mode takes place. The predicted path of failure is shown in Figure 4.94.

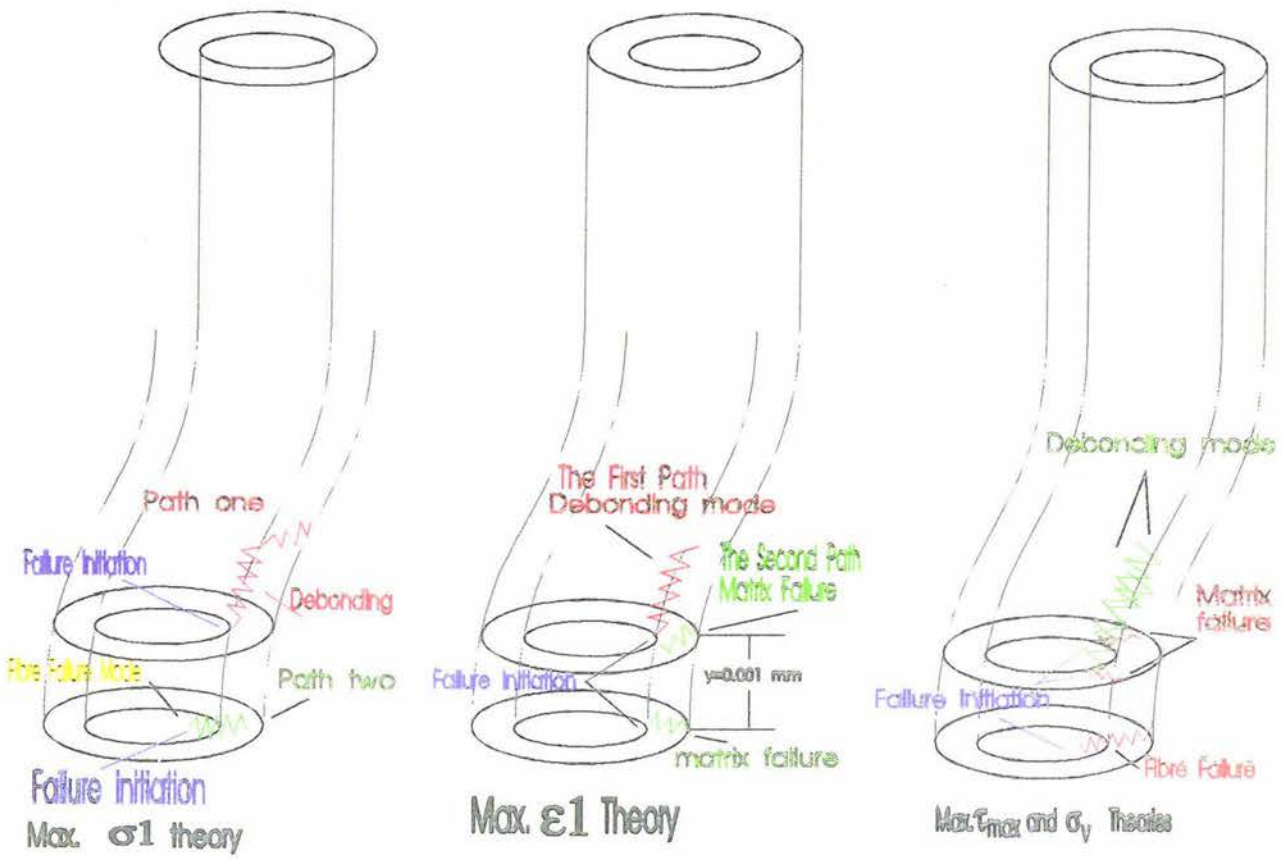

Figure 4.94. Predicted path of failure.

4.6. Interlaced Fibres-Matrix Model

4.6.1. Stress Analysis

It is important to note the following from sections 4.3 and 4.4. It was concluded that the compressive load between the weft and warp fibres decreases the peak values of the stress components in the vicinity of the connection point and changes the stress situation in this region.

The stress situation of the interlaced fibres-matrix model is very similar to that in the model of section 4.5.2. Therefore, here just the differences which are the effects of the weft fibre will be discussed.

4.6.1.1. Normal Stress in the y-Direction

The weft fibre decreases the values of σ_y in the model of section 4.5.2 in the region close to the connection point. Ignoring the small changes of the values, the colour contours of the studied cross sections are identical to that of Figure 4.85. Comparing the graphs of Figures 4.95(a) and (b) (overleaf) indicates, while the end values of the graphs of σ_y for the model of section 4.5.2 gradually decrease, for the interlaced fibres-matrix model these values increase from the middle to section y=0.001 mm and then again decrease after section y=0.003 mm. These changes of the stress values are not shown in the colour contours of sections y=0.00001 mm and y=0.001 mm (see Figures 4.96(a) and (b)) because the y-component of the compressive contact load between the fibres is not big enough to change the sign of the stress in this region.

The stress concentration factor for the interlaced fibres-matrix model (SCF=3.786) shows a small increase relative to the model of section 4.5.2 (SCF=3.748). This can be explained using Figure 4.97. The matrix localized the connection load effects, so the introduced stress by this load, based on the finite element analysis (FEA) result, is predicted to be like that in Figure 4.97. That is why a small increase is seen in the magnitude of SCF relative to the model of section 4.5.2. The maximum values of σ_y on the studied cross sections of both the models are shown in Figure 4.98.

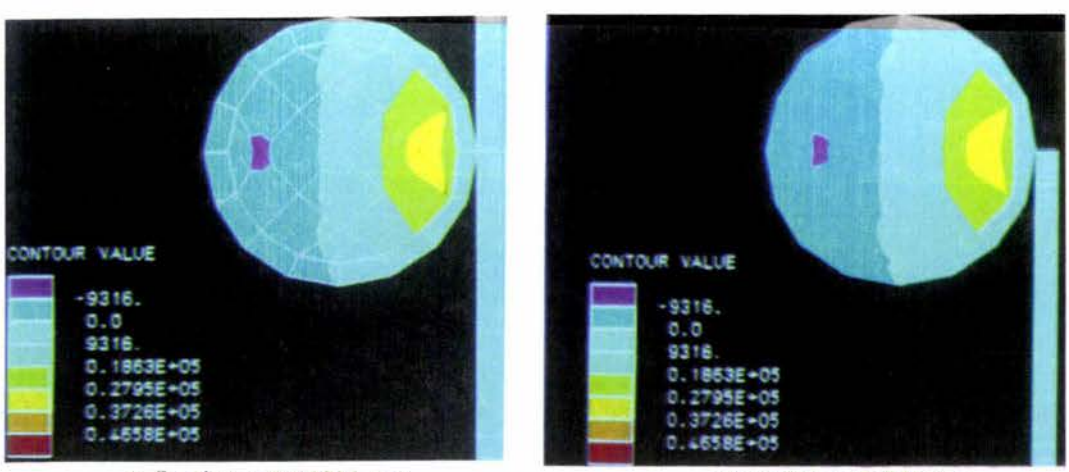

a) Section y=0.00001 mm. *b) section y=0.001 mm.*

Figure 4.96: Colour contour of σ_y in the crimped area.

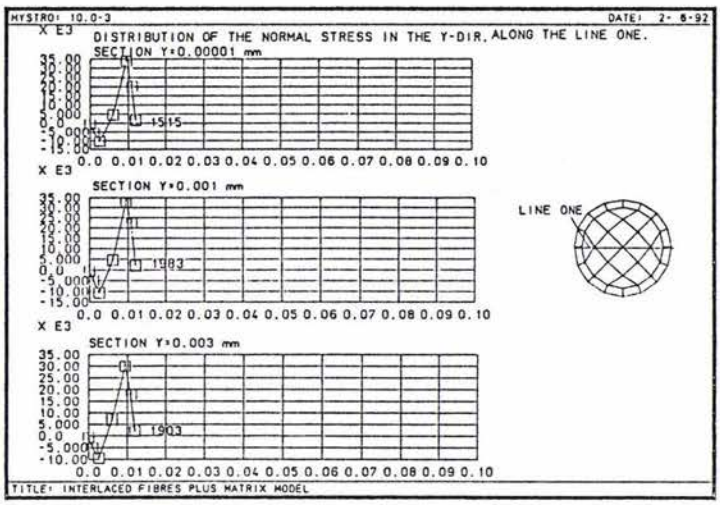

a) Interlaced fibres-matrix model.

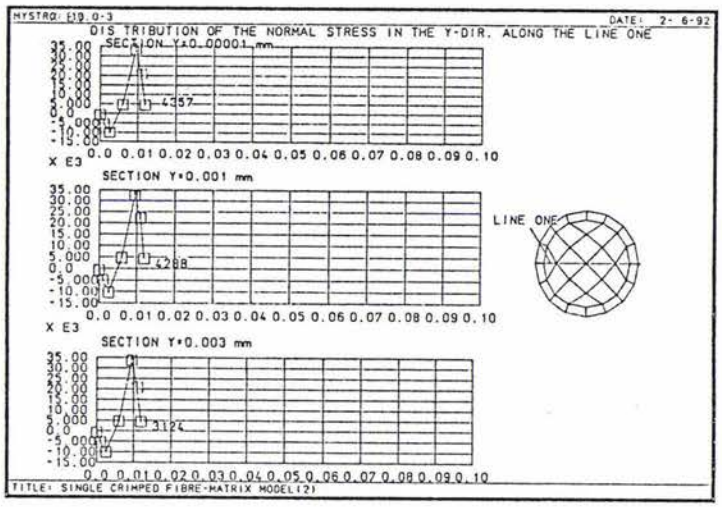

b) Model of section 4.5.2.

Figure 4.95: Distribution of σ_y in the crimp area.

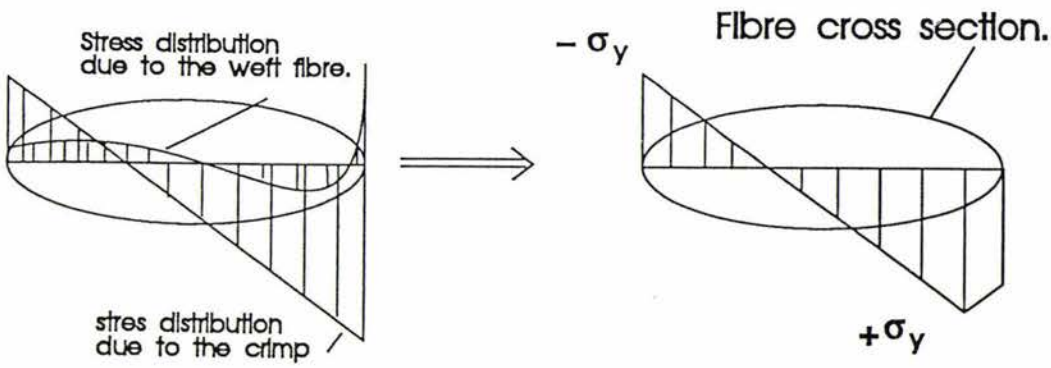

Figure 4.97: Prediction of the weft fibre effect on the stress distribution.

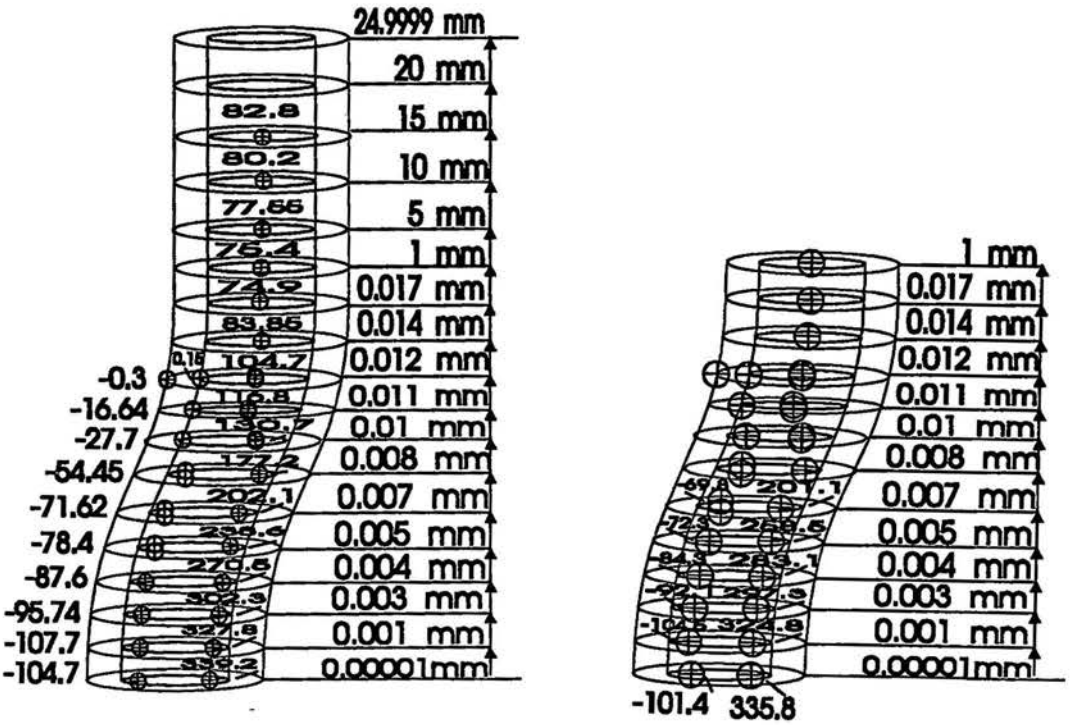

a) Interlaced fibres-matrix model. *b) Model of section 4.5.2.*

Figure 4.98: Maximum values of σ_y on the studied cross sections.

4.6.1.2. Normal Stress in the x-Direction

A small difference is seen on the contours of σ_x on sections y=0.00001 mm and y=0.001 mm relative to the same sections of the model of section 4.5.2 (compare Figures 4.99(a) and (b) with Figure 4.84). Figure 4.99(a) shows that instead of a compressive region an unexpected tensile region of σ_x appears near to the connection point and disappears on section y=0.001 mm. This is probably generated by the designed connection curve which was discussed in section 3.2. This curve probably acts as an imperfection which can change the stress distribution in its area. Comparing Figure 4.99(a) with the stress contour of section y=0.00001 mm in Figure 4.84 indicates that the compressive region has been moved towards the interface by the weft fibre.

Rather than the discussed tensile region the connection load between the fibres changes the values of the compressive region next to the connection load. Comparing the graphs of Figure 4.100(a) and (b) shows that on section y=0.00001 mm while the value of σ_x = -0.647 MN/m^2 for the model of section 4.6., it decreases to σ_x = -14.97 MN/m^2 for the interlaced fibres-matrix model.

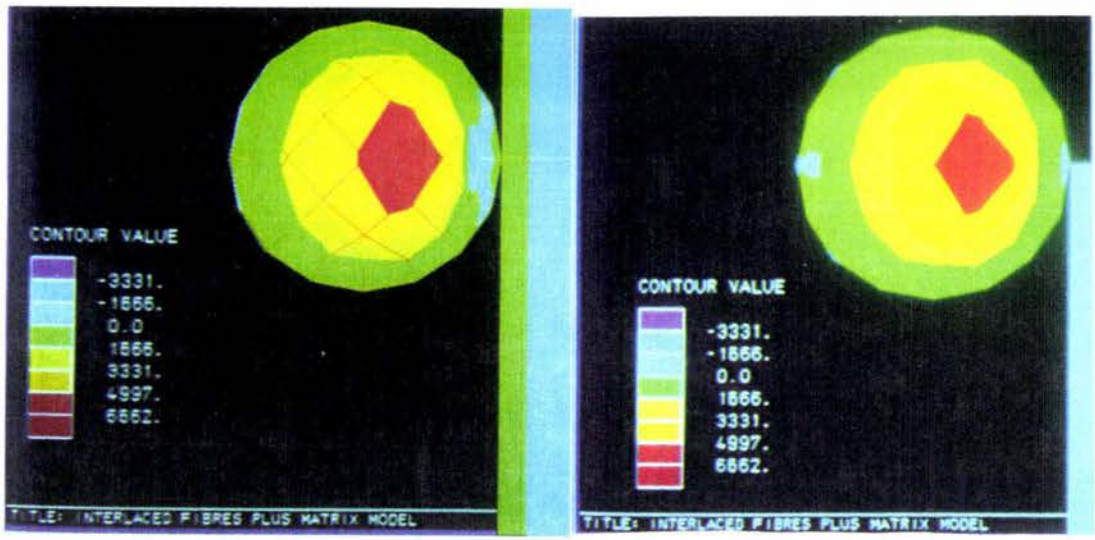

a) Section y=0.00001 mm. *b) section y=0.001 mm.*

Figure 4.99: Colour contour of σ_x in the crimped area.

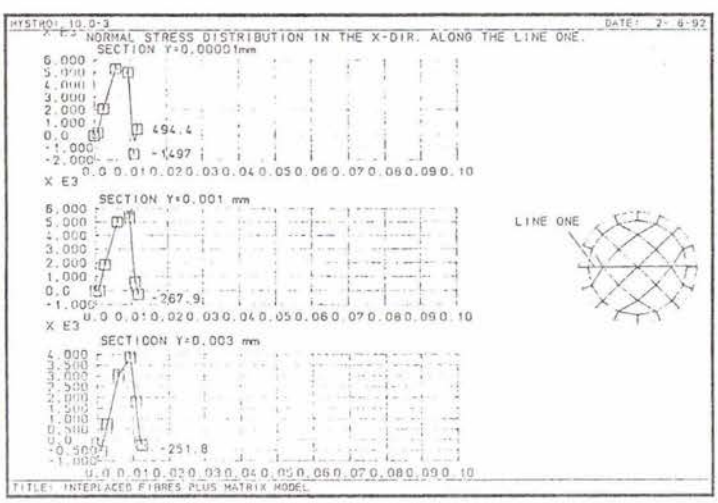

a) Interlaced fibres-matrix model.

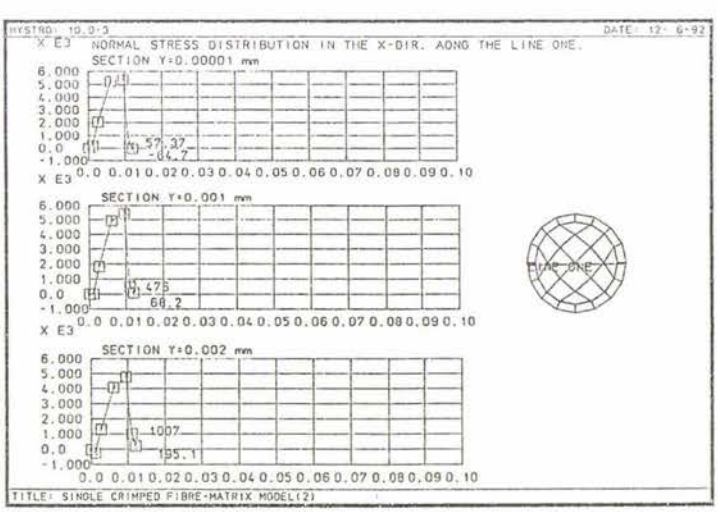

b) Model of section 4.5.2.

Figure 4.100: Distribution of σ_x in the crimp area.

4.6.1.3. Normal Stress in the z-Direction

The weft fibre causes the high stress regions of section y=0.00001 mm in Figure 4.86 to extend to the matrix area for the interlaced fibres-matrix model (see Figures 4.101 (a) and (b) (overleaf)). This means that instead of decreasing the value of σ_z in the vicinity of the connection point, because of the compressive load between the fibres, the value actually increases (compare the end values of the graphs of Figures 4.103 and 4.102). This might be explained by the same reason as for σ_x. Above this section, the graphs of figure 4.103 show that in section y=0.001 mm the value of σ_x decreases, which is expected because the effect of the weft fibre appears as a compressive stress. The compressive load causes some differences in the stress values in whole of the model also. Despite the differences, the colour contours of σ_z on the studied cross sections are identical to Figure 4.86.

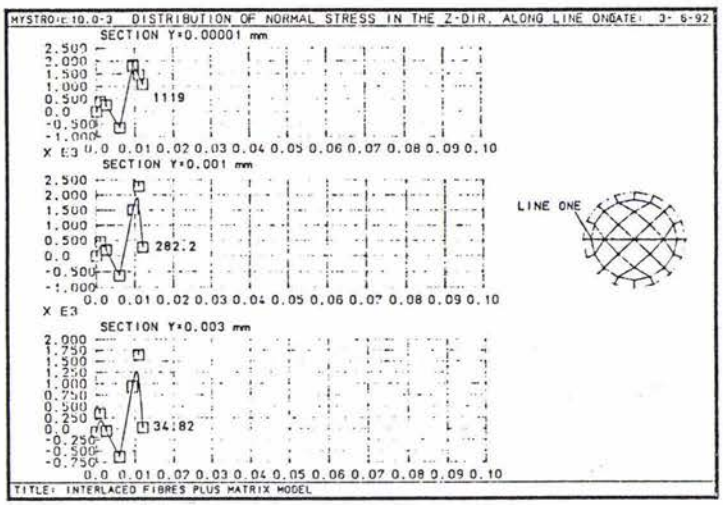

a) Interlaced fibres-matrix model.

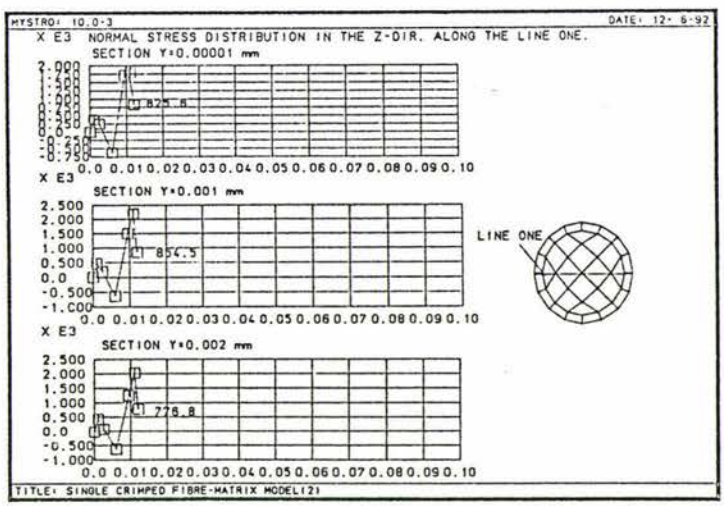

b) Model of section 4.5.2.

Figure 4.102: Distribution of σ_z in the crimp area.

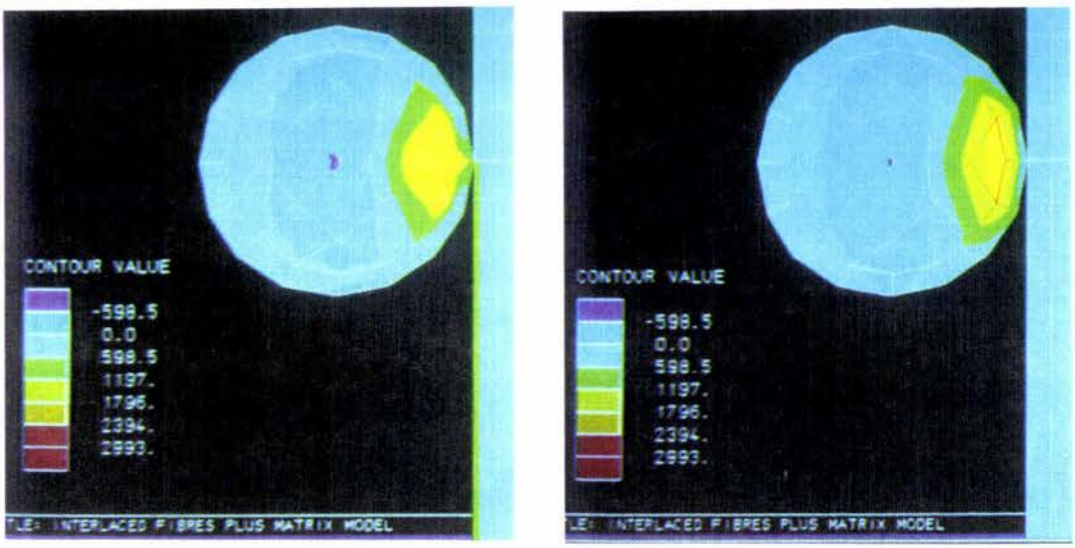

a) Section y=0.00001 mm. *b) section y=0.001 mm.*

Figure 4.101: Colour contour of σ_z in the crimped area.

4.6.1.4. Shear Stress Components

The colour contours of the shear stress components on the xy, yz, and xz-planes (which are not shown here) are very similar to Figures 4.87, 4.88, and 4.89 respectively. In this section only a comparison between the values of these quantities with the same quantities of the model of section 4.5.2 is presented.

The difference between the values is not very great because the matrix localizes the weft fibre effects so that only small changes occur for the normal stress components which govern the shear stress on the different planes (compare Figures 4.103(a), (b), (c) with Figures 4.104(a), (b), and (c) respectively). The value and position of the maximum shear stress is more important than the shear stress components which will be discussed in the failure analysis section.

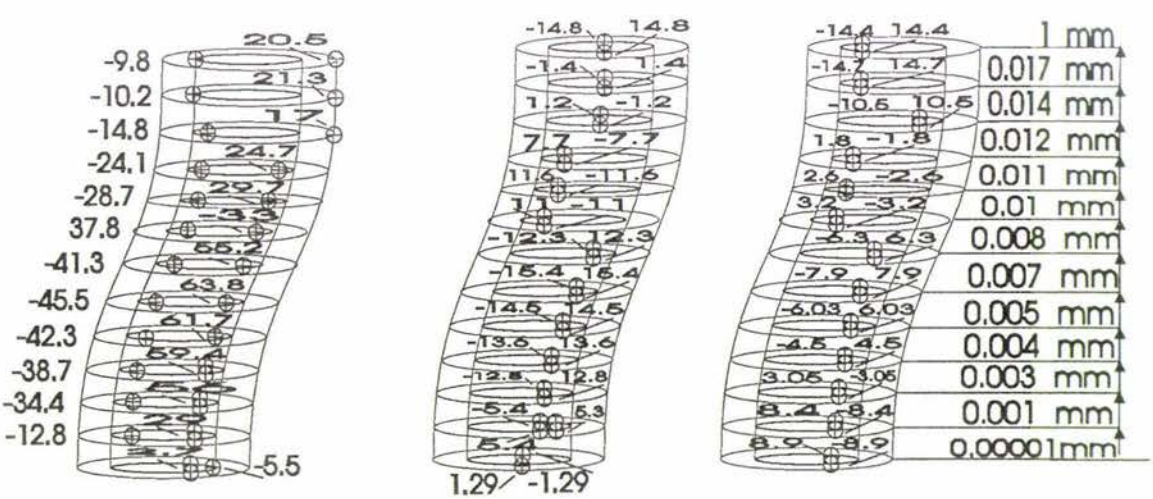

a) xy-plane b) yz-plane c) xz-plane

Figure 4.103: Maximum values of the shear stress components for the interlaced fibres-matrix model.

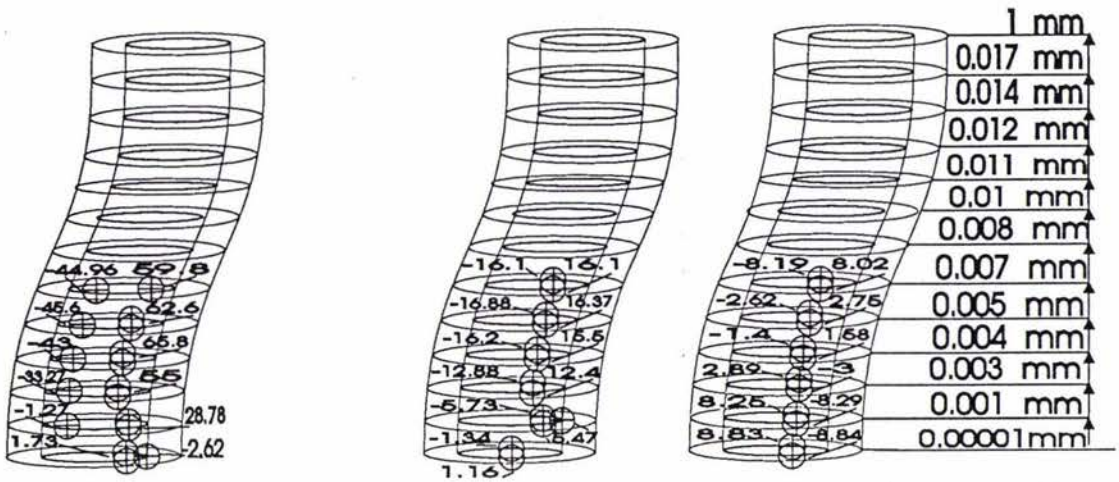

a) xy-plane b) yz-plane c) xz-plane

Figure 4.104: Maximum values of the shear stress components for the model of section 4.5.2.

4.6.2. Failure Analysis

4.6.2.1. Maximum Normal Stress Criterion

Applying this theory to the fibre yields the result that, ignoring the matrix and interface situations, the model is safe under the applied load (see Figure 4.105(a) for the position of maximum of σ_1)

$$\sigma_1 = 339.2 \text{ MN/m}^2 < \sigma_{uts} = 3450 \text{ MN/m}^2$$

and will fail from the middle of the crimp area with increasing load. A different result is found by applying this criterion to the matrix. According to the graphs of the maximum principal stress on section y=0.001 mm the maximum value of σ_1 in the matrix area occurs at the interface along the line two (see Figures 4.106(a) and (b)). Based on this theory the model under the applied load has already failed

$$\sigma_{uts} = 40 \text{ to } 90 \text{ MN/m}^2 < \sigma_1 = 281.3 \text{ MN/m}^2$$

The Failure, using this criterion, will initiate at the interface where the maximum of σ_1 occurs but it may propagate transverse to matrix area or, subject to the interface strength, along the length of the fibre as a debonding phenomenon. The graphs of Figure 4.106(b) indicate that the latter path, i.e. debonding, is more possible than the former one because normally under a real situation the interface is the weaker part of a composite. The predicted paths of Failure are shown in Figure 4.105(b).

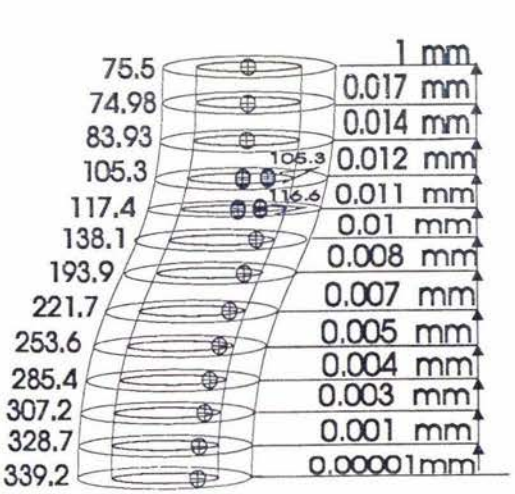

a) Maximum values of σ_1.

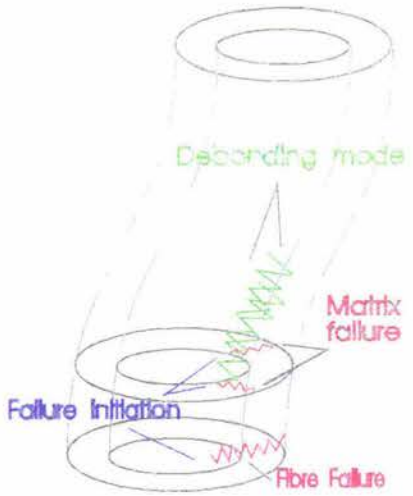

b) Predicted paths of failure.

Figure 4.105

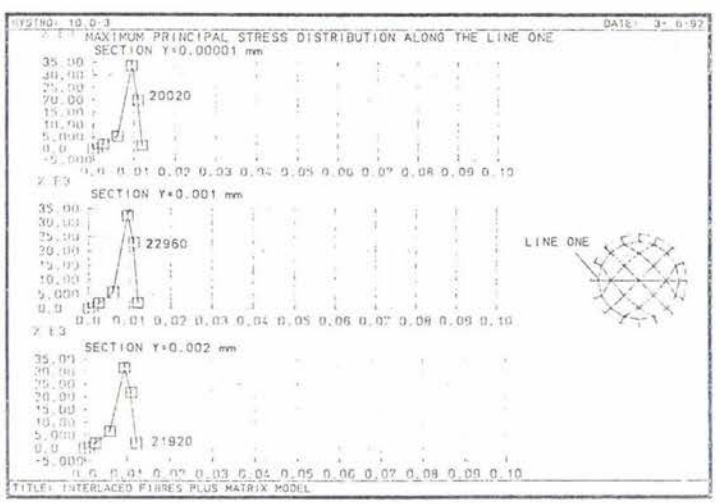

a) Along the line one.

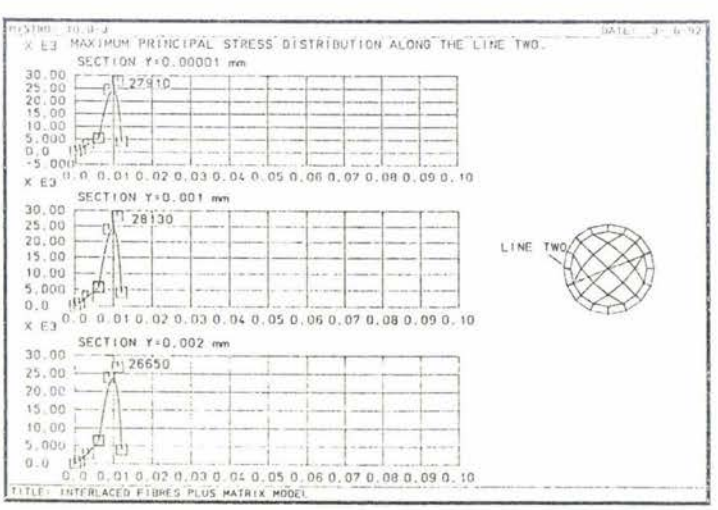

b) Along the line two.

Figure 4.106: Distribution of σ_1 in the crimped area.

4.6.2.2. Maximum Normal Strain Criterion

The maximum principal strain on the fibre area, similar to that which was found for the model of section 4.5.2, occurs on section y=0.001 mm at the interface region (see Figures 4.107). Applying the theory to the fibre gives

$$\varepsilon_1 = 0.007973 < \varepsilon_{uts} = 0.0454$$

which indicates that the fibre can carry a higher level load. With the increasing of the load as the maximum of ε_1 happens in the interface it is possible that, as was described in section 4.5.2.2.2, the debonding mode happens before the fibre failure mode (see Figure 4.108(b) (overleaf)).

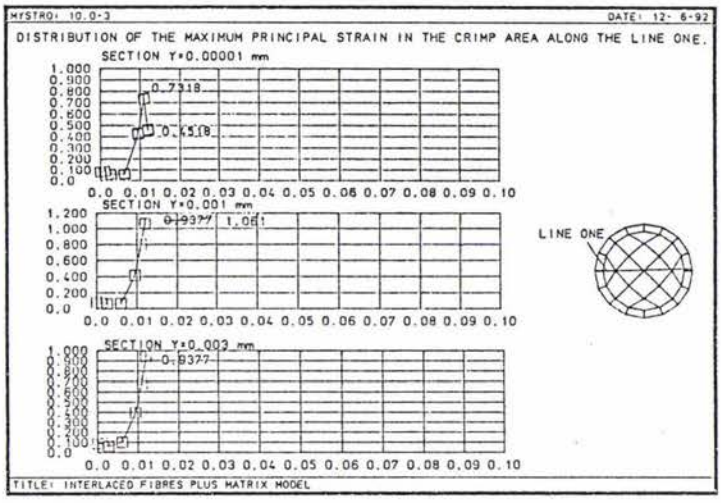

Figure 4.107: Distribution of ε_1 in the crimped area.

Comparing the values of Figures 4.107 and 4.108(a)(overleaf) shows that, unlike in section 4.5.2.2.2. the maximum value of ε_1 on the matrix area occurs at section y=0.001 mm. The drop in the distribution graph of ε_1 on the matrix area which is shown in Figure 4.107 (section y=0.00001 mm) is the effect of the compressive load between the weft and warp fibres. Based on this theory , under the applied load the matrix is in a critical situation i.e.

$$\underset{\text{(Lower bound)}}{\varepsilon_{uts} = 0.01} < \varepsilon_1 = 0.01061 < \underset{\text{(Upper bound)}}{\varepsilon_{uts} = 0.0225}$$

The failure will initiate at the outer surface of the matrix and then propagate through the thickness of the matrix cylinder (see Figure 4.108(b) (overleaf) for predicted paths of failure).

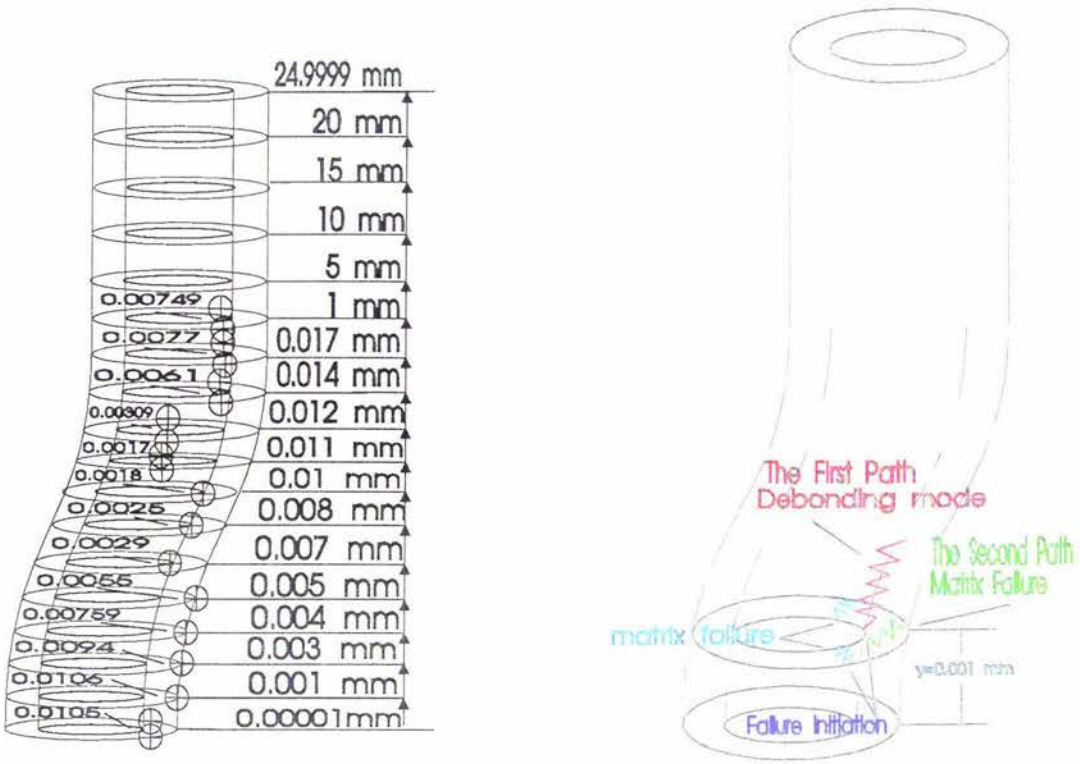

a) Maximum values of ε_1. *b) Predicted paths of failure.*

Figure 4.108

4.6.2.3. Maximum Shear Stress Criterion

As was found for the previous model the maximum value of τ_{max} occurs in the middle of the crimp on the fibre area (see Figure 4.109).

Comparing the distribution graphs of Figure 4.110 shows that, for the matrix area, the maximum value of τ_{max} occurs along the lines two and three in section y=0.001 mm. Applying the criterion gives

$$0.5\ \sigma_{uts} = 20 \text{ to } 45\ \text{MN/m}^2 \quad < \quad \tau_{max} = 137.8\ \text{MN/m}^2$$

Based on this result the matrix has already failed. The Failure occurs at the position of the maximum value of τ_{max} in the interface region and, as was described for the maximum normal stress criterion, the initiated crack may run in one of the two possible directions. It is likely that the debonding mode occurs first and is followed by the matrix failure mode (see Figure 4.105(b) for the predicted paths of failure).

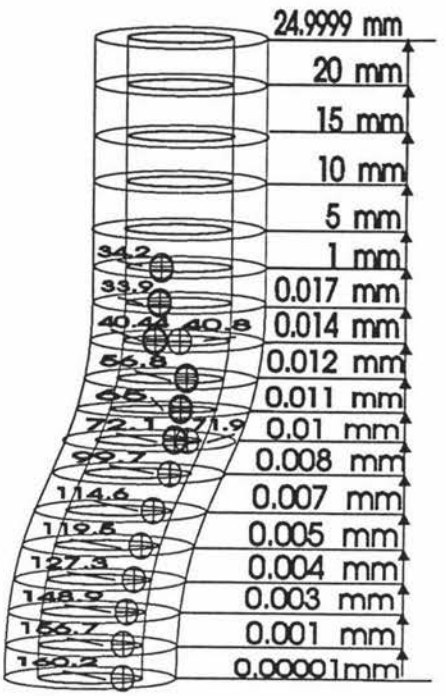

Figure 4.109: maximum values of τ_{max}.

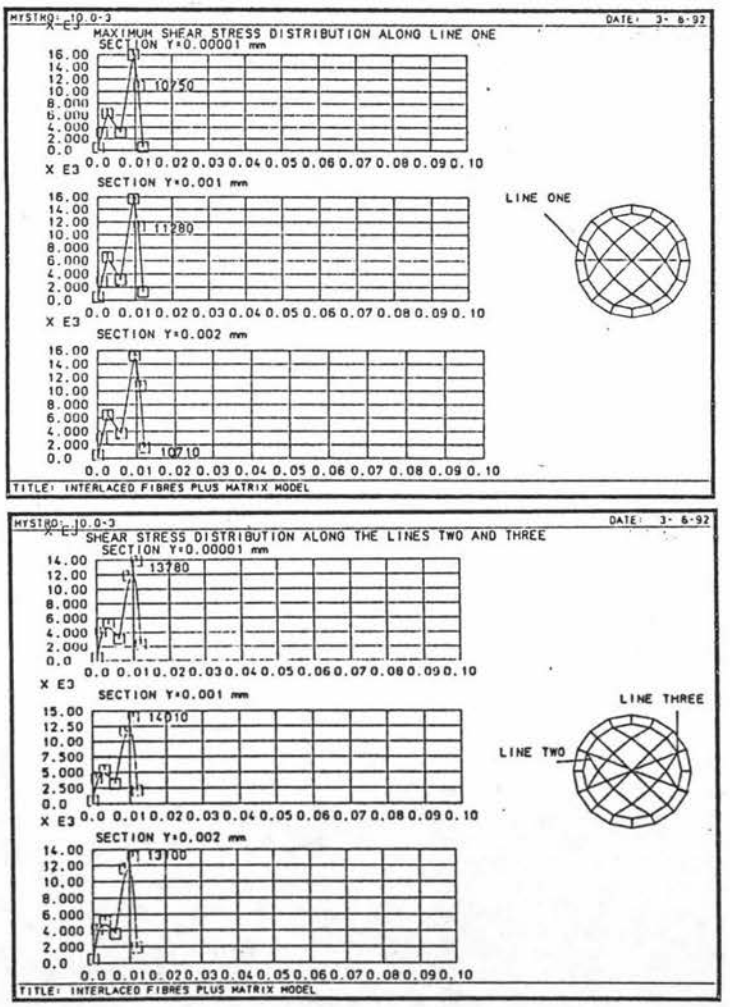

Figure 4.110: Distribution graphs of τ_{max} in the crimped area.

4.6.2.4. Maximum Distorsional Energy Theory

The position of the maximum value of σ_v on the fibre and matrix are the same as the maximum shear stress criterion (see Figures 4.111 and 4.112). Based on this theory, the same as the last section, under the applied load the matrix has already failed because

$$\sigma_{uts} = 40 \text{ to } 90 \text{ MN/m}^2 < \sigma_v = 271.9 \text{ MN/m}^2$$

The failure is predicted to occur in the same position as the last criterion and propagates as in Figure 4.105(b).

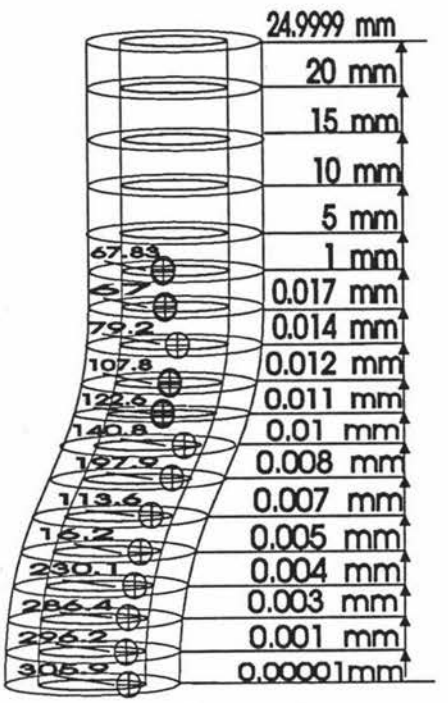

Figure 4.110: maximum values of σ_v.

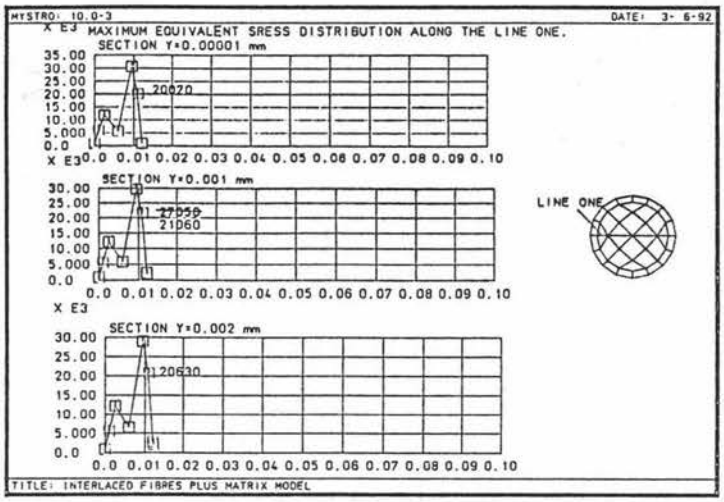

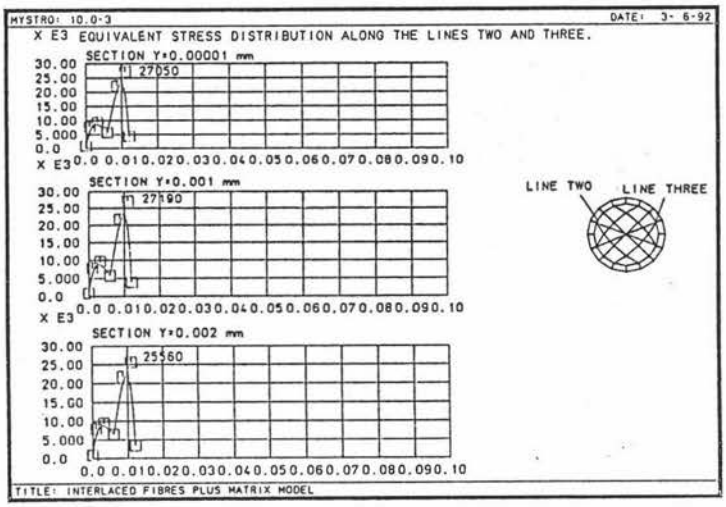

Figure 4.111: Distribution graphs of σ_y in the crimped area.

CHAPTER 5:

General Discussion and Conclusions

5.1. Introduction

In this chapter it is desirable to compare the results of the five models together. The discussion here is divided into the following sections:

I) Comparing the results of a straight fibre with the crimped fibre without matrix to study the effects of curvature on the failure and stress distribution.

II) Comparing the results of the crimped fibre with the crimped fibre-matrix models with different matrix volume fractions to study the effects of the matrix volume fraction on stress distribution and failure.

III) Comparing the results of the crimped fibre-matrix with the straight fibre-matrix to study the stress distribution through the matrix thickness.

IV) Comparing the results of the crimped fibre with the interlaced fibres to study the effects of the weft fibre on the failure and stress distribution.

V) Comparing the results of the interlaced fibres-matrix with the crimped fibre-matrix and the interlaced fibres model to study the effects of the matrix on the failure and stress distribution of the warp fibre.

5.2. Results Comparison

I) How does a crimp affect the stress distribution of a straight fibre?

Regarding the FEA results of section 4.3, a big change is introduced in the stress distribution by a curvature along the length of the fibre. The crimp introduces a misalignment for the reaction of the applied load. The misalignment generates a big moment in this area which governs the stress distribution (see section 4.3.1.1).

In this study based on the considered geometry for the crimp, a SCF of magnitude 8.78 was found on the fibre area. This quantity (SCF) could play a major role in the failure of the fibre. The resultant moment also introduced a big compressive region of stress in the convex part of the crimp which affects the equivalent (von Mises) stress. It is noted that, any increase in the equivalent stress decreases the design load for the composite. In addition to the above changes, it changes the values of the x and z-components which can affect the principal and maximum shear stresses. These changes also decrease the design load for the composite.

II) How does a matrix affect the stress distribution of a crimped fibre?

The designed cylindrical matrix, depending upon the matrix volume fraction, caused different changes in the results of the crimped fibre.

A) Big Matrix Volume Fraction.

With a thick matrix cylinder, big changes were seen for the maximum stress values relative to the crimped fibre. The SCF value was decreased to 1.4 from 8.78 for the crimped fibre model. Despite the big changes in the values, the stress nature for the fibre area was found to be only slightly different to the contours of stress for the crimped fibre.

Although the matrix, due to the smaller modulus of elasticity, carries a small fraction of the applied load, it allows the stress on the fibre to redistribute through the matrix thickness. As a result the composite can be designed for carrying a higher level of load.

B) Small Matrix Volume Fraction

The FEA results show that with a smaller matrix volume fraction the magnitude of the SCF increases to 3.74 from 1.4 in section (A). Comparing the stress distribution graphs for the thin and thick matrix cylinders shows that the gradient of the stress and strain distribution curves are bigger for the former than the latter. As a result the design load for the composite is decreased relative to section (A) but shows an increase with respect to the results of the crimped fibre without matrix model. The nature of the normal and shear stress components on the fibre area for the model with thin matrix cylinder was found in good agreement with the results of the crimped fibre model.

III) Considering the crimped fibre-matrix model from the failure point of view, the order of occurrance of the failure modes and the place of the failure initiation are different to those of the straight fibre-matrix model. For the straight fibre-matrix model it was predicted that the failure based on the maximum shear stress and von-Mises criteria may initiate on the interface at section y=10 mm and under the normal stress and strain criteria also on the interface but at the middle of the fibre's length. Meanwhile, for the crimped fibre-matrix model it was predicted that, except under the maximum strain criterion where the failure occurs at section y=0.007 mm, the failure initiates at the middle of the crimp area at the interface. For all criteria the failure for the crimped fibre-matrix model with the small matrix volume fraction was predicted to occur at section y=0.001 mm on the interface region.

The reason for the different position of the failure initiation of the crimped fibre with the two different matrix volume fractions can be explained by the geometry of the model. This model was generated with the same configuration as the crimped fibre of the interlaced fibres-matrix model. Therefore, the designed connection curve (see section 3.) could act as an imperfection and thus deviation of the stress values at the middle section of the crimp occurs. This was confirmed by the results of the interlaced fibres-matrix model. The maximum values of the stress components appeared at the same position as this model. Regarding the above result a

recommendation is made to consider further work on contact geometry of the weft and warp fibres.

IV) The effects of a weft fibre can be studied by comparing the results of the crimped fibre with the interlaced fibres model. The weft fibre changed the stress regions of the crimped fibre next to the connection point. The compressive load between the fibres decreased the stress values in the whole model. As a result the stress concentration factor for the interlaced fibres (SCF = 7.6) shows a decrease relative to the crimped fibre. Ignoring the values, the nature of the normal and shear stress components were the same except for the sections y=0.00001 mm and y=0.001 mm due to the compressive connection load. The positions of the maximum stress values were also changed and as a result the path of failure initiation changed too.

V) The results of the interlaced fibres-matrix model, which is the major aim of this investigation, are compared with the single crimped fibre-matrix (the model with the small matrix volume fraction). The comparison shows that, in contrast to the interlaced fibres without matrix model, the weft fibre in this model increases the stress values on the crimped fibre. It was found that both the designed connection curve (see section 3.2, Figure 3.6) and the matrix size (see Figure 4.97) can affect the connection load between the fibres to cause this change. This was confirmed by comparing the normal stresses in the x and z-directions of the model with the available data for the crimped fibre-matrix model. The comparison showed that, instead of a compressive region of σ_x appearing in the vicinity of the connection point, a tensile region appeared. The same phenomenon was seen for σ_y. It was concluded that the designed connection curve acts as an imperfection (see also section (III) of this chapter) and the matrix changes the direction of the compressive contact load in a small region on the fibre area near to the interface (see Figure 4.97).

5.3. Conclusion

From the above discussion the following was concluded for a simple cell (i.e. the interlaced fibres-matrix model) of a woven roving mat composite:

1) The stress concentration factor on the warp fibre depends on the matrix volume fraction or gap between the fibres. As a result wherever the fibres make direct contact the fibre failure mode may happen before the other failure modes.

2) The position of the maximum value of the stress components depends upon the configuration of the fibre contact area.

3) Despite the high formability of the woven composites their strength decreases with any curvature along the length of their warp fibres.

4) Based on the examined failure criteria, subject to perfect manufactured fibres, the failure of a woven composite initiates on the interface area in the concave part of the crimp. Assuming the interface is the weakest part of a composite, the initiated crack propagates along the length of the fibre as a debonding failure mode. This will be

followed by matrix failure and finally the woven composite cell will collapse by the fibre fracture mode.

5) If it is considered that the matrix in the convex part of the crimp does not move along with the fibre it is possible that , due to the fibre straightening out, the fibre debonding mode occurs in this area as well (see chapter one).

5.4. Recommendations

A woven roving composite may consist of a huge number of cells and the warp fibre can have many curvatures along its length (see Figure 5.1). Thus, for better understanding of the composite stress situation and failure behaviour, the following models are recommended for further study using MYSTRO and LUSAS softwares:

1) Studying the stress and failure behaviour of a fibre with three crimped areas along its length with and without the matrix (see Figure 5.2).

2) Studying the stress and failure behaviour of the above model with three weft fibres with and without the matrix (see Figure 5.3).

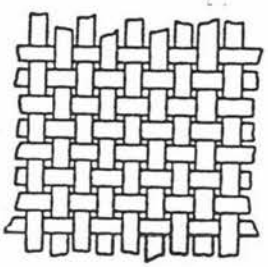

Figure 5.1: Configuration of a woven roving composite.

Figure 5.2: A warp fibre with three curvatures along its length.

Figure 5.3: The warp fibre plus three weft fibres.

3) Studying the effects of two parallel crimped fibres on each other with and without the matrix (see Figure 5.4).

4) Studying the failure and stress situation of the model of section 3 with the weft fibres with and without the matrix (see Figure 5.5).

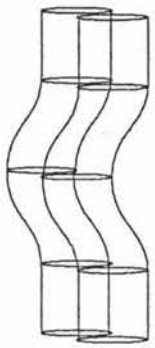

Figure 5.4: Two parallel crimped fibres.

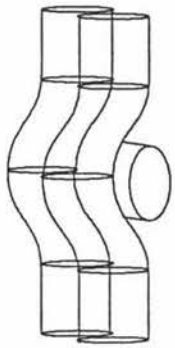

Figure 5.5: Interlaced fibres.

5) Studying the model of section 4 with residual stress consideration.

6) Studying the model of section 5 with the temperature effects consideration.

7) Studying the effects of the internal voids in the matrix area on the internal stress concentration using MYSTRO and LUSAS by modelling a void in the matrix area.

8) Studying the above sections with an imperfect interface is not possible because the Elasto-Plastic Interface facility provided in MYSTRO is not suitable for modelling the fibre and matrix interface.

References

1. Chou, T.W. " Strength and Failure Behaviour of Textile Structural Composites," Proceedings of the American Society for Composites, 1st Tech. Conf., Technomic Publishing Co., Inc., Lancaster, PA,(1986).

2. Ishikawa, T. and T. W. Chou. " Stiffness and Strength Behaviour of Woven Fabric Composites," Journal of Materials Science, 17:3211 (1982).

3. Ishikawa, T. and T. W. Chou. " Nonlinear Behaviour of Woven Fabric Composites " Journal of Composite Materials, 17:399 (1983).

4. Ishikawa, T. and T. W. Chou. " Elastic Behaviour of Woven Hybrid Composites," Journal of Composite Materials, 16:2 (1982).

5. Ishikawa, T. and T. W. Chou. : Stiffness and Strength Properties of Woven Fabric Composites ," Progress in Science and Engineering of Composite Materials, Proceeding of the Fourth International Conference on Composite Materials (1982).

6. Zienkiewicz O.C. The Finite Element Method, 3rd Edition McGraw-Hill (1985).

7. Seng C. Tan. " A Progressive Failure Model for Composite Laminates Containing Openings," Journal of Composite Materials, 25:556 (1991).

8. Fu-Kuo Chang and Larry B. Lessard. " Damage Tolerance of Laminated Composites Containing an Open Hole and Subjected to Compressive Loadings: Part I-Analysis," Journal of Composite Materials, 25:1 (1991).

9. Soutis, C. and N. A. Fleck. " Static Compression Failure of Carbon Fibre T800/924C Composite Plate with a Single Hole," Journal of Composite Materials, 24:536 (1990).

10. Sun C. T. and Chu. G. D. " Reducing Free Edge Effect on Laminate Strength by Edge Modification," Journal of Composite Materials, 25:142 (1991).

11. Fu-Kuo Chang, Jose Luis Perez and Kuo-Yen Chang. " Analysis of Thick Laminated Composites," Journal of Composite Materials, 24:801 (1990).

12. Morely, J. G. High-Performance Fibre Composites. Academic Press Limited, London, (1987).

13. Carl Zweden, H. Thomas Hahn, Tsu-Wei Chou, Delaware Composites Design Encyclopedia, Volume 1: Mechanical Behaviour and Properties of Composite Materials. Technomic Publishing Company, Inc. (1989).

14. Yoshida, H., T.Ogasa and R. Hayashi. " Statistical Approach to the Relationship between ILSS and Void Content of CFRP," Composite Science and Technology25:331 (1986).

15. Keith T. Kedward and James M. Whitney. Delaware Composites Design Encyclopedia, Volume 5: Design Study. Technomic Publishing Company, Inc. (1990).

16. Smith E. W. and Pascoe K. J., " Biaxial Fatigue of a Glass-Fibre Reinforced Composite, Part 2: Failure Criteria For Fatigue and Fracture," Biaxial Fatigue and Fracture, Mechanical Engineering Publications London PP 397-421 (1989).

17. Tsai, S. W. and H. T. Hahn. " Introduction to Composite Materials," Technomic Publishing Co., Inc., Lancaster, PA (1980).

18. Askenazi, E. K. " Problems of the Anisotropy of Strength," Mekanica Polimerov, vol. 1, No. 2, PP 79-92 (1965).

19. Tsai, S. W. and Edward M. Wu. " A General Theory of Strength for Anisotropic Materials," Journal of Composite Materials, 5:58 (1971).

20. Narayanaswami, R. and H. M. Adelman, " Evaluation of the Tensor Polynomial and Hoffman Strength Theories for Composite Materials " Journal of Composite Materials, 4:366 (1977).

21. Evans, K. E. and W. C. Zhang. " The Determination of the Normal Interaction Term in the Tsai-Wu Tensor Polynomial Strength Criterion," Composites Science and Technology, 30:251 (1987).

22. Hashin, Z. and Rotem. " A Fatigue Failure Criterion of Fibre Reinforced Materials," Journal of Composite Materials, 4:448 (1973).

23. Nahas, M. N. " Survey of Failure and Post-Failure Theories of Laminated Fibre-Reinforced composites," Journal of Composites Technology and Research, 8:138 (1986).

24. Weeton, J. W., Peters, D. M. and K. L. Thomas. Engineers' Guide to Composite Materials, American Society for Metals (1983).

25. Hall D. An Introduction to Composite Materials, Cambridge University Press (1981).

26. Mystro and Lusas User Manual. FEA Ltd., Forge House, 66 High St., Kingston Upon Thames, Surrey, KT1 1HN, UK.

27. Shigley, J. E. Mechanical Engineering Design, 5th Edition, McGrow-Hill, (1989).

28. Chang, F. K. and K. Y. Chang. " A Progressive Damage Model for Laminated Composites Containing Stress Concentrations," Journal of Composite Materials 21:834, (1987).

29. Feng, W. W. " A Failure Criterion for Composite Materials," Journal of Composite Materials, 25:88, (1991).

30. Christensen, R. H. " Tensor Transformations and Failure Criteria for the Analysis of Fibre Composite Materials Part II," Journal of Composite Materials, 24:796, (1990).

Appendix (A)

A great review of the existing composite's failure criteria is found in Smith and Pascoe [16]. A few of the latest failure criteria is presented in this paper.

I) Failure Criterion for Notched [0/90/ 45]s Laminates under off-Axis Loading.

The notched laminate would fail if

$$\sigma_{yy}\,|_{x=d_o} = \sigma_o$$

where σ_o is laminate strength without free edge stress and notch effects, σ_{yy} is the normal stress. d_o is the critical distance from the notch root at which the normal stress is equal to the unnotch ultimate stress at failure of the notched specimen and could be found from the following math. expression

$$\frac{\sigma_o}{\sigma_N^{\infty}} = \beta_1 + \beta_2 \left(\frac{1}{d_o}\right)^{0.5} + \beta_3 \left(\frac{1}{d_o}\right)^{0.5} + \beta_4 \left(\frac{1}{d_o}\right)^{0.5}$$

see Sun and Chu [10] for β's calculation.

II) Static compression failure criterion for composite plates with a single hole [9].

Prediction of stable crack growth is based on a critical stress value and the stress distribution adjacent to the circular hole. It is postulated that microbuckling occurs over a distance lb from the discontinuity when the average stress over the distance lb reaches the stress of the unnotched laminate,

$$\sigma^{\infty} = \sigma_o \left[\frac{1-\xi}{A+B\sqrt{1+D\xi^2} + C\sqrt{1+E\xi^2}}\right]$$

where σ^{∞} is the stress at which microbuckling occurs and

$$\xi = \frac{1}{1 + l_b/R}$$

Microbuckling begins when $l_b = 0$, at a stress σ_i^{∞} given by the above equation.

III) A set of Failure criteria incorporated with in situ ply strength distributions are proposed to predict failure and the mode of failure of each ply in laminated composites.

A) Matrix Tensile Cracking

For predicting tensile cracking failure ($\sigma_y \geq 0$), the failure criterion has the form [28]

$$\left(\frac{\sigma_y}{Y_t}\right)^2 + \frac{\int_0^{\gamma_{xy}} \sigma_{xy}\, d\gamma_{xy}}{\int_0^{\gamma^u_{xy}} \sigma_{xy}\, d\gamma_{xy}} = e^2_M$$

where σ_y and σ_{xy} are the transverse tensile stress and shear stress in each layer, respectively. γ^u_{xy} is the ultimate shear strain and Y_t is the transverse tensile strength.

B) Matrix Compression Failure

For predicting matrix compression failure ($\sigma_y < 0$), the failure criterion is similar to that of the tensile matrix cracking criterion. It is expressed as:

$$\left(\frac{\sigma_y}{Y_c}\right)^2 + \frac{\int_0^{\gamma_{xy}} \sigma_{xy}\, d\gamma_{xy}}{\int_0^{\gamma^u_{xy}} \sigma_{xy}\, d\gamma_{xy}} = e^2_M$$

C) Fibre Buckling Failure

For predicting fibre buckling ($\sigma_X < 0$) , the failure criterion is based on the fibre buckling strength theory proposed by Lessard and Chang [8]. The criterion is expressed as:

$$\frac{\sigma_x}{X_c} = e_b$$

where X_C is a function of load distribution and mechanical properties of fibres and matrix. The fibre buckling failure criterion states that when, in any one of the plies in a laminate, the stress satisfies the criterion($e_b > 1$), that layer fails in fibre buckling.

D) Fibre-Matrix Shearing Failure[8]

The fibre-matrix shearing failure criterion states that when in any one of the plies in a laminate, the combined stresses σ_x ($\sigma_x < 0$) and σ_{xy} satisfy the criterion with $e_{fs} > 1$, that layer fails by fibre-matrix shearing.

$$\left(\frac{\sigma_x}{X_c}\right)^2 + \frac{\int_0^{\gamma_{xy}} \sigma_{xy}\, d\gamma_{xy}}{\int_0^{\gamma_{xy}^u} \sigma_{xy}\, d\gamma_{xy}} = e_{fs}^2$$

IV) A failure criterion for composite materials based upon the strain invariants of finite elasticity.

the failure criterion assumes that the materials transversely isotropic and that the failure occurs when the strain energy density reaches its maximum value. The criterion have the form

$$f = A_1 (I_1 -3) + A_{11} (I_1 -3)^2 + A_2 (I_2 -3) + A_4 (I_4 -1) + A_5 (I_5 -1) +$$

$$A_{55} (I_5 - 1)^2 + A_{15} (I_1 -3) (I_5 -1) + a$$

For the coefficient see [29].

V) Laminate Failure Criterion[30]

The fibre and matrix failure criteria are derived from a constitutive equation for transversely isotropic fibre reinforced media. The stress constitutive equation and the associated failure criteria are given by

$$\sigma_{ij} = \underbrace{\lambda \varepsilon_{kk} \delta_{ij} + 2 \mu \varepsilon_{ij}}_{\text{Matrix constituent}} + \underbrace{(E_{11} - E) \delta_{li} \delta_{lj} \varepsilon_{ll}}_{\text{Fibre Constituent}}$$

$$\underbrace{\alpha\varepsilon_{kk} + e_{ij}\, e_{ij} \le k^2}_{\text{Matrix Failure}} \qquad \underbrace{\varepsilon_f^{(-)} \le \varepsilon_{11} \le \varepsilon_f^{(+)}}_{\text{Fibre Failure}}$$

Axis 1 is in the fibre direction, with E_{11} being the fibre direction modulus while λ, μ and E are the fibre\matrix interaction based moduli expressed in terms of ν_{12}, E_{22}, μ_{12}, and μ_{23} by forms given in [30].